

Understanding Current and Future Mountain Hydroclimate: Consideration of Air Temperature, Snow, and Rock Glaciers

A Dissertation
Presented in Partial Fulfillment of the Requirements for the
Degree of Doctor of Philosophy
with a
Major in Water Resources
in the
College of Graduate Studies
University of Idaho
by
Abigail C. Lute

Major Professor: Timothy Link, Ph.D.
Committee Members: John Abatzoglou, Ph.D.; Andrew Fountain, Ph.D.;
Timothy Bartholomaeus, Ph.D.
Department Administrator: Timothy Link, Ph.D.


August 2021

Authorization to Submit Dissertation

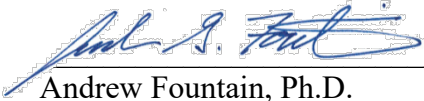
This dissertation of Abigail C. Lute, submitted for the degree of Doctor of Philosophy with a Major in Water Resources and titled "Understanding Current and Future Mountain Hydroclimate: Consideration of Air Temperature, Snow, and Rock Glaciers," has been reviewed in final form. Permission, as indicated by the signatures and dates below, is now granted to submit final copies to the College of Graduate Studies for approval.

Major Professor: 


Timothy Link, Ph.D. Date: July 15, 2021

Committee Members: 


John Abatzoglou, Ph.D. Date: July 16, 2021



Andrew Fountain, Ph.D. Date: July 27, 2021



Timothy Bartholomaeus, Ph.D. Date: July 27, 2021

Department
Administrator: 

Timothy Link, Ph.D. Date: July 15, 2021

Abstract

The hydroclimate of mountain environments shapes the spatiotemporal distribution of energy and water on scales from local to global. Climate change is inducing rapid changes in mountain hydroclimate in the form of warmer temperatures, reduced snowpack and glacier mass balance, and earlier snowmelt runoff. These changes have large implications for local and downstream ecosystems and societies. However, understanding of current and future mountain hydroclimate is hindered by a paucity of observations and the need for high resolution data and models to capture the effects of topographic complexity. New modeling approaches, tools, and datasets are needed. This dissertation addresses these needs with a focus on three important aspects of mountain hydroclimate: air temperature, snow, and rock glaciers. In the first study, I quantify the error and uncertainty in air temperature lapse rates and outline best practices for lapse rate estimation. In the second study, I develop a novel energy balance snow model and force it with new high-resolution multitemporal climate forcings to create snow and climate metrics for the western United States. In the final study, I employ a machine learning method to understand the response of rock glacier spatial distributions to climate change. This dissertation contributes to scientific understanding of mountain hydroclimate and provides tools and datasets to further develop this understanding.

Acknowledgements

First and foremost, I would like to thank my advisor, John Abatzoglou. When I came to the University of Idaho for my master's degree, John was willing to take a chance on me even though I only had a music degree. Throughout my master's and my PhD, John has been consistently kind, available, proactively supportive, and insistent on high standards. I would not have accomplished what I have without his amazing mentorship and advocacy.

I would also like to thank Tim Link. In addition to being a valuable scientific mentor, Tim has always looked out for me- from setting me up with an amazing internship at the Coldwater Lab in Canmore to going to bat for me to make sure U of I did not take away my email address. When John moved, Tim stepped up to be my major advisor and chief advocate at U of I.

I thank my committee member Tim Bartholomaus for pushing me to think about things from different perspectives. His questions are consistently challenging and have led me to grow as a scientist.

I thank my committee member Andrew Fountain for his enthusiasm for my work and willingness to engage from afar. Andrew was always available for a check-in and for interesting and informative conversations about climate, glaciers, and rock glaciers.

I would like to recognize my IGERT colleagues who provided companionship and new perspectives, especially Riveraine Walters, Konrad Hafen, Becky Witinok-Huber, and Matt Dunkle. A special thank you goes to Adrienne Marshall who inspired me to take on new challenges, pushed me to not underestimate myself, and was always available for a de-stressing run on the mountain when I needed it.

Thank you also to my friends and family for their unwavering support and cheerleading, even when I felt stuck. Juan, thank you for sacrificing so much to move to Moscow with me and for always talking to me and providing perspective when I was having a rough time. Link, thanks for the many phone conversations and for your pride in me, it's mutual. Moontanners, you inspire me to do my best and think for myself. Gus and Leo, your unwavering affection and happiness have made my life so much richer.

I thank the National Science Foundation (NSF) Integrative Graduate Education and Research Traineeship (IGERT) program (award 1249400) and a Hydroinformatics Innovation Fellowship from the Consortium of Universities Allied for Water Research (CUAHSI; NSF Cooperative Agreement No. EAR-1849458) for helping to fund this work.

I would like to acknowledge my privilege as a white, upper-middle class woman. I have seen repeatedly how this has made the road smoother for me and allowed me to be successful.

This research was conducted on the homelands of the Nimiipu (Nez Perce), at the University of Idaho in Moscow, Idaho. The University of Idaho is a land grant university whose endowment was partially funded by more than 87,000 acres of land acquired through the Morrill Act. The United States government used treaties and seizures to obtain land from the Shoshone-Bannocks, Nimiipu, and Schitsu'umsh (Couer d'Alene) tribes. The income generated from this land, benefitting the university, is 372 times the amount paid to the tribes¹. Additionally, data used in this research was collected on land significant to many Indigenous communities across the western United States. I recognize, pay respect, and extend gratitude to the Indigenous communities that live upon, hold sacred, and care for the lands reflected in this research.

¹Lee, R. (2020). *Morrill Act of 1862 Indigenous Land Parcels Database*, High Country News.

Dedication

To my parents, who always told me I could be whoever I wanted to be and supported me in all possible ways

Table of Contents

Authorization to Submit Dissertation	ii
Abstract	iii
Acknowledgements	iv
Dedication	v
Table of Contents	vi
List of Tables	viii
List of Figures	ix
List of Equations	xiv
Statement of Contribution	xv
Chapter 1: Introduction	1
References	5
Chapter 2: Best Practices for Estimating Near-Surface Air Temperature Lapse Rates.....	8
Abstract	8
Introduction	8
Data	11
Methods	14
Results	19
Discussion	29
Conclusions	33
References	33
Chapter 3: SnowClim: High-Resolution Snow Model and Data for the Western United States	38
Abstract	38
Introduction	38
Model Description.....	41
Model Application to the Western United States.....	51
Data Availability	61
Discussion and Conclusions.....	62
References	64
Chapter 4: Projected Loss of Active Rock Glaciers in the Western U.S. with Warming.....	76
Abstract	76
Introduction	76
Data and Methods.....	78

Results	83
Discussion and Conclusions.....	90
References	93
Chapter 5: Conclusion.....	102
Appendix A - Best Practices for Estimating Near-Surface Temperature Lapse Rates.....	106
Synthetic datasets covariates.....	106
Observational station data covariates.....	107
References	111
Appendix B - SnowClim: High-Resolution Snow Model and Data for the Western United States	114
Appendix C - Projected Loss of Active Rock Glaciers in the Western U.S. with Warming	118
Data	118
Model Complexity.....	123
References	135

List of Tables

Table 2.1 Covariates used to account for non-elevational effects on temperature. Additional information is available in Appendix A.....	14
Table 3.1 Required forcing data for the snow model.....	42
Table 3.2 Parameters, their abbreviated names, the parameter values used in calibration, and their units. Parameter values with an * indicate values chosen for the full model run by calibration at SNOTEL sites. Additional parameter options, including the VIC model albedo option, were evaluated in preliminary work but were excluded from the full calibration due to consistently poor performance. ¹ Essery et al., (2013); ² Tarboton & Luce, (1996).....	51
Table 3.3 WRF data used to derive forcing data for the snow model.	54
Table 3.4 Summary climate and snow variables included in the SnowClim dataset. Summary variables are available for pre-industrial, historical, and future time periods.	62
Table C.1 Environmental covariates used in the Maxent model. ¹ Lute et al., (2021); ² Gesch et al., (2018); ³ Anning & Ator, (2017).	119
Table C.2 Descriptions of numeric lithology classes which were used as a categorical variable in the Maxent model. Data is from Anning & Ator, (2017).	120
Table C.3 AUC values from cross-validation experiments. Calibration AUC is the AUC from the model calibrated on the indicated spatial fold. Validation AUC is the AUC of the model calibrated on the other fold and validated on the indicated spatial fold. Delta AUC is the difference between the calibration and validation AUC values.....	128
Table C.4 Summary of pre-industrial, historical, and future rock glacier habitat, grouped by level III ecoregion. Suitable and unsuitable areas are defined by the 0.212 threshold as discussed in the text. Values are in km ² , except for the percent changes which are in %. Total column shows the area of the whole ecoregion, whereas the Modeled column shows the area within the ecoregion that was included in the distribution model.....	134

List of Figures

- Figure 2.1 a) Black line shows mean elevation across longitude over the study domain of the Oregon Cascades, USA (42.8- 44°N, 120.5-123°W). Colored points show mean summer maximum temperature from 30 weather stations with symbols indicating the originating network. Vertical grey dashed line marks the maximum elevation of the transect and divides the stations into west and east groups. b) Examples of lapse rates calculated from these stations, including using only sites from the US Cooperative Observer Program (COOP), the US Interagency Remote Automatic Weather Stations network (RAWS), the US Natural Resources Conservation Service Snowpack Telemetry network (SNOTEL), only sites east or west of the divide, the mean environmental lapse rate (MELR, $-6.5\text{ }^{\circ}\text{C km}^{-1}$), or all stations ($n=30$). c) Distribution of lapse rates estimated from 15,000 samples of 10 stations from the full population shown in a). Colors and symbols in c) indicate lapse rates shown in b). Vertical jitter has been added to points in c). 10
- Figure 2.2 Oregon Cascades study area. Red box in inset map shows location of Oregon Cascades study area in Western North America. The 30 meteorological stations used in this study are indicated by markers according to the observation network. Light blue polygons are waterbodies..... 12
- Figure 2.3 Lapse rate mean error (x-axis) and interquartile range (y-axis) estimated via a) SLR and b) MLR for datasets with varying levels of dataset noise (size) and collinearity (color, shape). Lapse rates are estimated from samples of 5 stations drawn from each synthetic dataset..... 19
- Figure 2.4 MAE of lapse rates (log scale on y-axis) estimated from synthetic datasets using SLR (left column) and MLR (right column). MAE is calculated across all possible samples of the sample size indicated on the x-axis. In the upper plots each line represents a synthetic dataset with a different collinearity level and with dataset noise of 1°C , in the lower plots each line represents a dataset with a different level of dataset noise and with collinearity of 0.6..... 20
- Figure 2.5 Percent change in a) MAE and b) IQR between the most similar decile of samples selected using TDA and all samples. Results are shown for lapse rates estimated via SLR from samples of varying sample size (x-axis) drawn from datasets with collinearity of 0.3 and varying dataset noise (y-axis). Negative values indicate that the most similar decile had lower MAE or IQR than the average sample. Positive values (grey) indicate increased MAE or IQR..... 21
- Figure 2.6 Percent difference in MAE between lapse rates of varying sample size (x-axis) selected by TDA (i.e., the median lapse rate from the most similar decile of samples) and lapse rates calculated from the full subpopulations using SLR (subpopulation size shown on y-axis). Blue, outlined points indicate reduced MAE. Data is from the synthetic dataset with noise of 1°C and collinearity of 0.6..... 23
- Figure 2.7 Lapse rates calculated from samples of five stations from the 30 stations in the Oregon Cascades dataset for Tmax (top) and Tmin (bottom). Yellow boxes indicate lapse rates calculated via SLR. Red boxes correspond to lapse rates calculated via MLR using elevation, solar radiation, and distance from coast as predictors. Green

- boxes indicate free-air lapse rates calculated from ERA-Interim reanalysis collocated with stations (see Appendix A for details) and are the same for Tmax and Tmin. 24
- Figure 2.8 (a) Oregon Cascades domain with stations colored according to cluster, as indicated by boxplot legend. (b) Tmax lapse rates estimated via SLR from samples of 5 stations from the full dataset ('all', n=30), the 'west' cluster (n=17), and the 'east' cluster (n=13). Tsc indicates lapse rates estimated for the 'east' and 'west' clusters using spatially corrected station temperatures. Tsc* indicates lapse rates estimated from spatially corrected temperatures from the 'east' cluster with influential stations removed (n=12)..... 26
- Figure 2.9 Cumulative distributions of spatially corrected Tmax lapse rates estimated from samples of stations from the 'west' (left column) and 'east' (right column) clusters of the Oregon Cascades dataset for summer and winter (rows). Sample sizes of 13 and 10 were used for the 'west' and 'east' clusters, respectively. Results are grouped by decile of the dissimilarity metric. Only deciles 1, 3, 8, and 10 are shown. 28
- Figure 2.10 Decision tree outlining best practices for estimating near-surface temperature lapse rates. N is the total number of stations available (i.e., the population size). 31
- Figure 2.11 Seasonal Tmax lapse rates estimated for the Oregon Cascades stations following best practices. Colored points represent the single best lapse rate (i.e., the median lapse rate of the most similar decile of samples) and colored bars indicate uncertainty range (the minimum and maximum lapse rates of the most similar decile of samples). Grey violin plots illustrate the possible lapse rates that can be estimated from any combination of 10 stations from the original dataset, not using best practices. White dots indicate the lapse rate estimated from the full 30 station dataset not using best practices. The gray dashed line marks the MELR ($-6.5^{\circ}\text{C km}^{-1}$)..... 32
- Figure 3.1 Snow model conceptual diagram. Solid black arrows indicate mass fluxes, dashed grey arrows indicate energy fluxes. Fluxes are described in the text. 43
- Figure 3.2 Performance metrics for an hourly model run with the selected parameterization. 57
- Figure 3.3 Time series of observed and modeled SWE at the Hilts Creek, Idaho SNOTEL site. Out of all 170 SNOTEL sites, errors at this site were closest to the all-station median errors reported in the text. 58
- Figure 3.4 Snow model performance for different time steps using the parameter set selected in calibration of the hourly model. Points represent median values across 170 SNOTEL sites. 58
- Figure 3.5 a) Historical and b) future maxswe (mm), c) historical and d) future snow duration (days). Historical values are averages over the period 2000-2013. Future values represent averages during the period 2071-2100 under RCP 8.5. In a) and b), white land areas denote areas that had less than 10 mm maxswe. In c) and d), white land areas denote areas where snow duration was 0. Note the non-linear colorscale in panels a) and b). 59
- Figure 3.6 a) Absolute and b) percent change in maxswe between historical and future periods. c) Absolute and d) percent change in snow duration between historical and

future periods. Small box in northern Utah indicates the region highlighted in Figure 3.7.....	60
Figure 3.7 Example of simulations of changing maxswe for a portion of the Uinta Mountains, Utah (location is marked in Figure 3.6). The elevation (m) of the domain is shown in a). The percent change (%) in maxswe between historical and late 21st century periods as simulated by a 4 km WRF product (Liu et al., 2017) is shown in b) and the same metric but from the SnowClim dataset is shown in c).....	61
Figure 4.1 a) Modeling domain. Elevation of terrain is indicated by the color bar. Black points denote known rock glacier locations. In bivariate density plots (b and c), salmon color indicates the distribution of rock glacier locations while grey blue indicates the distribution of background domain locations in two-dimensional pre-industrial covariate space.....	79
Figure 4.2 a) Importance of each variable to capturing rock glacier habitat suitability according to Maxent jackknife approach. Model performance (y-axis) is the normalized regularized training gain. Black horizontal line indicates the performance of the model with all variables. Light grey bars indicate the performance of all models built with all variables except the variable of interest. Dark grey bars indicate the performance of models built on each variable alone and determine the order of the bars. b) Marginal response functions illustrating the relationship between the covariate values (x-axis) and the rock glacier habitat suitability (y-axis) when other variables are held constant at their average sample value.	85
Figure 4.3 Predicted suitability for rock glaciers under pre-industrial (a), present (b), and future (c) conditions across the western U.S. The Beartooth Mountains, Montana domain used in subsequent analyses is marked by a black rectangle on the western U.S. maps. d) shows the area on the y-axis that exceeds the suitability level on the x-axis (starting at 0.1) for the three time periods. The dashed line in d) marks the suitability threshold used in subsequent analyses (0.212).	86
Figure 4.4 Changes in rock glacier habitat suitability over time in the Beartooth Mountains, Montana. Elevation of the terrain (a). Changes in rock glacier suitability between a) pre-industrial and present periods and b) present and future periods. Black and white outlines denote the locations of present-day rock glaciers and glaciers, respectively.	89
Figure A.1 Correlation matrix for a subset of the covariates associated with the Oregon Cascades stations for Summer and Winter. Numbers and colors indicate the correlation coefficient.	107
Figure B.1 Map of modeling domain with locations modeled at 210m spatial resolution in blue.....	114
Figure B.2 Performance of best hourly model at SNOTEL sites in temperature-precipitation space. Each point represents a SNOTEL site.	115
Figure B.3 Parameter sensitivity of hourly model performance.....	116
Figure B.4 Performance of snow model without shallow snow correction for different time steps using the parameter set selected in calibration of the hourly model with	

shallow snow correction. Points represent median values across 170 SNOTEL sites.	117
Figure C.1 Correlation matrices for pre-industrial, present, and future time periods. White x's denote correlations with absolute values greater than 0.7.	122
Figure C.2 AICc values for different levels of regularization beta parameter and different feature class combinations.	124
Figure C.3 Map of spatial blocks used in the spatial cross validation analysis overlaid on western U.S. modeling domain. Blocks were grouped into folds as indicated by the number in each block.	125
Figure C.4. Predicted pre-industrial suitability at known rock glacier locations. Color scale is divided at the threshold that excludes 10% of known rock glaciers (0.212).	126
Figure C.5. Pre-industrial covariate distributions at known rock glacier locations. Quartiles on the x-axis are quartiles of predicted suitability with 1 being the least suitable and 4 being the most suitable.	127
Figure C.6. Response functions illustrating the relationship between the covariate values (x-axis) and the rock glacier habitat suitability (y-axis) based on models built on each variable in isolation.	128
Figure C.7. Distribution of covariates between preindustrial (blue) and present (purple) time periods, grouped by suitability change category. For covariates that are not time-varying (bottom row), a single violin is shown for each suitability category. In the first subplot, percent values indicate the percent of the full modeling domain that falls into each category.	129
Figure C.8. Distribution of covariates between present (purple) and future (red) time periods, grouped by suitability change category. For covariates that are not time-varying (bottom row), a single violin is shown for each suitability category. In the first subplot, percent values indicate the percent of the full modeling domain that falls into each category.	129
Figure C.9. Distribution of covariates between preindustrial (blue) and present (purple) time periods, for presently glaciated locations, grouped by suitability change category. For covariates that are not time-varying (bottom row), a single violin is shown for each suitability category. In the first subplot, percent values indicate the percent of modeled glaciated area that falls into each category.	130
Figure C.10. Distribution of covariates between present (purple) and future (red) time periods, for presently glaciated locations, grouped by suitability change category. For covariates that are not time-varying (bottom row), a single violin is shown for each suitability category. In the first subplot, percent values indicate the percent of modeled glaciated area that falls into each category.	130
Figure C.11. Predicted suitability for rock glaciers under pre-industrial (a), present (b), and future (c) conditions across the Beartooth Mountains, Montana domain. Red and turquoise outlines mark the locations of present day glaciers and rock glaciers, respectively.	131

- Figure C.12. Changes in environmental covariates over time at locations corresponding to present day glaciers and present-day rock glaciers in the Beartooth Mountains domain. Topographic variables, which do not change over time, are represented by one violin for glaciers and one for rock glaciers. The rocktype covariate is excluded from the plot because all glacier and rock glacier locations in the domain had the same rocktype (class 6). 132
- Figure C.13. For locations in the Beartooth Mountains, Montana, distributions of covariate values under pre-industrial and present conditions grouped by habitat suitability class. The rocktype covariate is not shown because the region has a single rocktype (class 6)..... 133
- Figure C.14. For locations in the Beartooth Mountains, Montana, distributions of covariate values under present and future conditions grouped by habitat suitability class. The rocktype covariate is not shown because the region has a single rocktype (class 6). 133

List of Equations

Equation 2.1	13
Equation 2.2	14
Equation 2.3	14
Equation 2.4	17
Equation 3.1	42
Equation 3.2	43
Equation 3.3	44
Equation 3.4	44
Equation 3.5	44
Equation 3.6	44
Equation 3.7	45
Equation 3.8	45
Equation 3.9	45
Equation 3.10	45
Equation 3.11	45
Equation 3.12	45
Equation 3.13	45
Equation 3.14	46
Equation 3.15	46
Equation 3.16	48
Equation 3.17	48
Equation 3.18	48
Equation 3.19	48
Equation 3.20	49
Equation 3.21	49
Equation 3.22	50
Equation 3.23	50
Equation 3.24	50
Equation 3.25	51
Equation 3.26	51
Equation 3.27	51
Equation 3.28	51
Equation A.1	106
Equation A.2	106
Equation A.3	106
Equation A.4	109
Equation A.5	110

Statement of Contribution

For chapter 2, Abigail Lute led the research, performed the analyses, and wrote the manuscript with mentorship and feedback from John Abatzoglou. For chapter 3, Abigail Lute developed the downscaling routines with feedback from John Abatzoglou. Abigail Lute developed the snow model with input from John Abatzoglou and Tim Link. Abigail Lute performed the model calibration, model runs, and additional analyses. Abigail Lute wrote the manuscript with input from John Abatzoglou and Tim Link. For chapter 4, Abigail Lute designed and led the research and wrote the manuscript with input from John Abatzoglou, Andrew Fountain, and Tim Bartholomaus.

Chapter 1: Introduction

The study of hydroclimatology is the study of fluxes and stores of energy and water, how they relate to one another, and how these quantities and relationships vary in space and time. In the context of mountains, there is an added focus on the effects of topographic complexity and on all things frozen- snow, ice, and permafrost. The hydroclimate of mountains is of particular interest because to a large extent, mountains shape the water resources of adjacent non-mountainous regions; mountains confronted with orthogonal winds induce orographic precipitation that defines stark wet-dry contrasts in adjacent basins, seasonal snow accumulation and storage in mountains is released downstream in warm months to support ecosystems, agriculture, and other human endeavors, and the presence of mountain snow and ice increases the planetary albedo. By regulating energy and water availability, mountain hydroclimate shapes ecosystems and economies on broad scales (Barnett et al., 2005; Huss et al., 2017).

One approach to understanding mountain hydroclimate is through the complementary lenses of time and space. Temporally, mountain hydroclimate is subject to natural variability on a range of scales from diurnal to seasonal, annual, and decadal. Examples of these scales of temporal variability include diurnal upslope and downslope winds, seasonal snow covered to snow free states, and annual to decadal patterns of temperature and precipitation stemming from large scale modes of climate variability such as the El Niño Southern Oscillation and the Pacific Decadal Oscillation. In addition to these layered modes of natural variability, there is increasing evidence of anthropogenic hydroclimatic change. Observations indicate that increasing greenhouse gas concentrations are warming mountain environments more than other environments (Mountain Research Initiative EDW Working Group, 2015) and melting snow and glaciers (Najafi et al., 2017; Roe et al., 2021), among many changes. These developments are expected to continue and may fundamentally alter mountain hydroclimate, for example by eliminating snow and glaciers in some mountain ranges, with large implications for ecosystems and societies (Huss et al., 2017). In the face of these changes, a more nuanced and comprehensive understanding of current and future mountain hydroclimate is needed.

Spatially, the topographic complexity of mountain environments requires an emphasis on fine scale variability. Coarser datasets and models of mountain hydroclimatic processes and their implications typically have larger errors than finer scale approaches. For example, coarser scale models tend to provide less accurate simulations of orographic precipitation (Chan et al., 2013), underestimate snowpack (Sohrabi et al., 2019), and overestimate species habitat loss under climate change (Randin et al., 2009). However, the development of high-resolution data and models for mountain environments is hindered by a paucity of observations (Strachan & Daly, 2017), either for use themselves or as validation, and by the increased computational cost of high-resolution modeling (Wood et al., 2011). These challenges highlight the need for novel approaches to make the most of available observational data and to maximize model physical realism within the current computational constraints.

Modeling approaches for addressing these challenges should be developed based on data availability, research questions, and computational resources. As an example, empirical models are typically less computationally expensive and quicker than other approaches and may also have fewer data requirements, both in terms of the number of data types and the quantity of each (Jajarmizad et al., 2012). More advanced data-driven approaches, such as artificial intelligence and machine learning, can detect relationships in massive datasets and are particularly useful when processes are poorly understood or parameters for a more mechanistic approach are unavailable (Shortridge et al., 2016). Physics-based modeling can be more computationally expensive than other approaches but is thought to provide better transferability to new conditions in space and time than empirical approaches since it emphasizes physical principles over calibrated parameters (Devi et al., 2015; Merz et al., 2011). In addition, there is potential for hybrid methods to capitalize on the assets of a variety of approaches while avoiding some of the limitations of each (Konapala et al., 2020; Kraft et al., 2021).

This dissertation addresses the needs for a) a more comprehensive understanding of the mountain hydroclimate and cryosphere and b) novel approaches to work within data and computation constraints, in the context of three hydroclimatic foci: air temperature, snow, and rock glaciers. These investigations, in the form of three chapters, are united by the common themes of temporal variability, long-term change, and topographic complexity. The

spatial modeling approach for each investigation is tailored to the research questions and data availability, resulting in a variety of spatial modeling approaches spanning empirical, machine learning, and physics-based methods.

The first study seeks to enhance our understanding of spatiotemporal temperature variability in mountain environments and improve downscaled climate data and environmental model simulations by making better use of available temperature observations (Lute & Abatzoglou, 2021). In statistical downscaling routines and environmental models, a single parameter called the air temperature lapse rate is often used to distribute temperature from either coarse grid cells to finer grid cells or from point locations across a domain. This parameter is typically assumed to be constant or is estimated from a handful of meteorological stations with no consideration of uncertainty. I used empirical analysis of a combination of synthetic and observational datasets to quantify error and uncertainty in lapse rates stemming from a variety of sources. I showed that the effects of lapse rate uncertainty can exceed the effects of climate change in some modeling contexts and provided a decision tree of best practices for lapse rate estimation. This study highlights the ability of empirical approaches to enhance the utility of limited observational data with the end result of improving climate datasets and environmental model simulations.

The second study addresses the need for a large extent, multitemporal, high-resolution, physics-based snow dataset to provide a more nuanced understanding of the changing mountain snowpack (Lute et al., 2021). Such datasets are not currently available due to the dual hurdles of insufficient climate forcing data and inadequate computational resources. I address the first hurdle by applying best practices for lapse rate estimation from the previous study to statistically downscale 4-hourly climate forcing data for pre-industrial, historical, and future time periods across the western United States (U.S.) at 210m spatial resolution. I then developed a hybrid computationally efficient energy balance snow model that contains the essential elements of physics-based snow models (i.e., energy and mass conservation), but incorporates empirical elements to enhance computational efficiency. I force the model with the downscaled climate forcings to create a multitemporal high-resolution dataset of climate and snow metrics across the western U.S. This dataset enables unprecedented analyses of changing mountain snowpack and its implications for wildlife, agriculture, hydrology, and other fields.

The final study also seeks to provide a more comprehensive understanding of the changing mountain cryosphere. While snow and glaciers in the western U.S. are expected to decline with continued warming (Lute et al., 2021; Moore et al., 2009), the insulating debris layer and slow response time to warming of rock glaciers suggest that they may persist longer than other components of the cryosphere (Anderson et al., 2018). However, broad scale projections of future rock glaciers are hindered by limited process understanding and limited data on debris thicknesses and internal debris concentrations. In light of these constraints, I employed a machine learning approach, Maxent (Phillips et al., 2006; Phillips & Dudík, 2008), to predict the future spatial distribution of rock glaciers in the western U.S. I supplied the model with topographic and geologic covariates in addition to the high-resolution snow and climate metrics developed in the second study. I showed that despite their insulating debris layers, rock glaciers are more sensitive to air temperature than they are to other covariates. Between pre-industrial and present-day periods the model predicted that suitable areas for rock glaciers would decline in many mountain ranges, but some areas formerly occupied by alpine glaciers would become more suitable for rock glaciers. However, by the late 21st century the model predicted drastic declines in suitable rock glacier habitat across the domain. This study suggests that even debris insulation cannot protect mountain ice under significant warming and highlights the value of machine learning approaches in the context of limited data.

In sum, this work employed a variety of approaches to advance scientific understanding of mountain hydroclimate and to provide new tools and datasets for further work. In terms of scientific knowledge, this work enhanced understanding of temperature lapse rate uncertainty and its sources, shed light on the climate sensitivity of mountain snowpack as it relates to topographic complexity, and highlighted the topoclimatic conditions under which rock glaciers can be expected to persist versus disappear. In addition, this work leaves a substantial legacy of tools and datasets for further research and for improvement of existing models and datasets including a decision tree of best practices for improving temperature lapse rate estimates, a computationally efficient energy balance snow model that can be run in the cloud, and a suite of multitemporal, high-resolution snow and climate metrics for the western U.S.

References

- Anderson, R. S., Anderson, L. S., Armstrong, W. H., Rossi, M. W., & Crump, S. E. (2018). Glaciation of alpine valleys: The glacier – debris-covered glacier – rock glacier continuum. *Geomorphology*, *311*, 127–142.
<https://doi.org/10.1016/j.geomorph.2018.03.015>
- Barnett, T. P., Adam, J. C., & Lettenmaier, D. P. (2005). Potential impacts of a warming climate on water availability in snow-dominated regions. *Nature*, *438*(7066), 303–309. <https://doi.org/10.1038/nature04141>
- Chan, S. C., Kendon, E. J., Fowler, H. J., Blenkinsop, S., Ferro, C. A. T., & Stephenson, D. B. (2013). Does increasing the spatial resolution of a regional climate model improve the simulated daily precipitation? *Climate Dynamics*, *41*(5–6), 1475–1495.
<https://doi.org/10.1007/s00382-012-1568-9>
- Devi, G. K., Ganasri, B. P., & Dwarakish, G. S. (2015). A Review on Hydrological Models. *Aquatic Procedia*, *4*, 1001–1007. <https://doi.org/10.1016/j.aqpro.2015.02.126>
- Huss, M., Bookhagen, B., Huggel, C., Jacobsen, D., Bradley, R. S., Clague, J. J., Vuille, M., Buytaert, W., Cayan, D. R., Greenwood, G., Mark, B. G., Milner, A. M., Weingartner, R., & Winder, M. (2017). Toward mountains without permanent snow and ice. *Earth's Future*, *5*(5), 2016EF000514. <https://doi.org/10.1002/2016EF000514>
- Jajarmizad, M., Harun, S., & Salarpour, M. (2012). A Review on Theoretical Consideration and Types of Models in Hydrology. *Journal of Environmental Science and Technology*, *5*(5), 249–261. <https://doi.org/10.3923/jest.2012.249.261>
- Konapala, G., Kao, S.-C., Painter, S. L., & Lu, D. (2020). Machine learning assisted hybrid models can improve streamflow simulation in diverse catchments across the conterminous US. *Environmental Research Letters*, *15*(10), 104022.
<https://doi.org/10.1088/1748-9326/aba927>
- Kraft, B., Jung, M., Körner, M., Koirala, S., & Reichstein, M. (2021). *Towards hybrid modeling of the global hydrological cycle* [Preprint]. Global hydrology/Modelling approaches. <https://doi.org/10.5194/hess-2021-211>
- Lute, A. C., & Abatzoglou, J. T. (2021). Best practices for estimating near-surface air temperature lapse rates. *International Journal of Climatology*, *41*(S1).
<https://doi.org/10.1002/joc.6668>

- Lute, A. C., Abatzoglou, J. T., & Link, T. (2021). SnowClim: High-resolution snow model and data for the western United States. *Manuscript in preparation*.
- Merz, R., Parajka, J., & Blöschl, G. (2011). Time stability of catchment model parameters: Implications for climate impact analyses. *Water Resources Research*, *47*(2).
<https://doi.org/10.1029/2010WR009505>
- Moore, R. D., Fleming, S. W., Menounos, B., Wheate, R., Fountain, A., Stahl, K., Holm, K., & Jakob, M. (2009). Glacier change in western North America: Influences on hydrology, geomorphic hazards and water quality. *Hydrological Processes*, *23*(1), 42–61. <https://doi.org/10.1002/hyp.7162>
- Mountain Research Initiative EDW Working Group. (2015). Elevation-dependent warming in mountain regions of the world. *Nature Climate Change*, *5*(5), 424–430.
<https://doi.org/10.1038/nclimate2563>
- Najafi, M. R., Zwiers, F., & Gillett, N. (2017). Attribution of the Observed Spring Snowpack Decline in British Columbia to Anthropogenic Climate Change. *Journal of Climate*, *30*(11), 4113–4130. <https://doi.org/10.1175/JCLI-D-16-0189.1>
- Phillips, S. J., Anderson, R. P., & Schapire, R. E. (2006). Maximum entropy modeling of species geographic distributions. *Ecological Modelling*, *190*(3), 231–259.
<https://doi.org/10.1016/j.ecolmodel.2005.03.026>
- Phillips, S. J., & Dudík, M. (2008). Modeling of species distributions with Maxent: New extensions and a comprehensive evaluation. *Ecography*, *31*(2), 161–175.
<https://doi.org/10.1111/j.0906-7590.2008.5203.x>
- Randin, C. F., Engler, R., Normand, S., Zappa, M., Zimmermann, N. E., Pearman, P. B., Vittoz, P., Thuiller, W., & Guisan, A. (2009). Climate change and plant distribution: Local models predict high-elevation persistence. *Global Change Biology*, *15*(6), 1557–1569. <https://doi.org/10.1111/j.1365-2486.2008.01766.x>
- Roe, G. H., Christian, J. E., & Marzeion, B. (2021). On the attribution of industrial-era glacier mass loss to anthropogenic climate change. *The Cryosphere*, *15*(4), 1889–1905. <https://doi.org/10.5194/tc-15-1889-2021>
- Shortridge, J. E., Guikema, S. D., & Zaitchik, B. F. (2016). Machine learning methods for empirical streamflow simulation: A comparison of model accuracy, interpretability,

- and uncertainty in seasonal watersheds. *Hydrology and Earth System Sciences*, 20(7), 2611–2628. <https://doi.org/10.5194/hess-20-2611-2016>
- Sohrabi, M. M., Tonina, D., Benjankar, R., Kumar, M., Kormos, P., Marks, D., & Luce, C. (2019). On the role of spatial resolution on snow estimates using a process-based snow model across a range of climatology and elevation. *Hydrological Processes*, 33(8), 1260–1275. <https://doi.org/10.1002/hyp.13397>
- Strachan, S., & Daly, C. (2017). Testing the daily PRISM air temperature model on semiarid mountain slopes. *Journal of Geophysical Research: Atmospheres*, 122(11), 5697–5715. <https://doi.org/10.1002/2016JD025920>
- Wood, E. F., Roundy, J. K., Troy, T. J., van Beek, L. P. H., Bierkens, M. F. P., Blyth, E., de Roo, A., Döll, P., Ek, M., Famiglietti, J., Gochis, D., van de Giesen, N., Houser, P., Jaffé, P. R., Kollet, S., Lehner, B., Lettenmaier, D. P., Peters-Lidard, C., Sivapalan, M., ... Whitehead, P. (2011). Hyperresolution global land surface modeling: Meeting a grand challenge for monitoring Earth's terrestrial water. *Water Resources Research*, 47(5). <https://doi.org/10.1029/2010WR010090>

Chapter 2: Best Practices for Estimating Near-Surface Air Temperature Lapse Rates

Lute, A.C. and J.T. Abatzoglou (2021). “Best Practices for Estimating Near-Surface Air Temperature Lapse Rates.” *International Journal of Climatology*, 41 (Suppl. 1): E110-E125.

Abstract

The near-surface air temperature lapse rate is the predominant source of spatial temperature variability in mountains and controls snowfall and snowmelt regimes, glacier mass balance, and species distributions. Lapse rates are often estimated from observational data, however there is little guidance on best practices for estimating lapse rates. We use observational and synthetic datasets to evaluate the error and uncertainty in lapse rate estimates stemming from sample size, dataset noise, covariate collinearity, domain selection, and estimation methods. We find that lapse rates estimated from small sample sizes (<5) or datasets with high noise or collinearity can have errors of several °C km⁻¹. Uncertainty in lapse rates due to non-elevation related largescale temperature variability was reduced by correcting for spatial temperature gradients and restricting domains based on spatial clusters of stations. We generally found simple linear regression to be more robust than multiple linear regression for lapse rate estimation. Finally, lapse rates had lower error and uncertainty when estimated from a sample of topoclimatically self-similar stations. Motivated by these results, we outline a set of best practices for lapse rate estimation that include using quality controlled temperature observations from as many locations as possible within the study domain, accounting for and minimizing non-elevational sources of climatic gradients, and calculating lapse rates using simple linear regression across topoclimatically self-similar samples of stations which are roughly 80% of the station population size.

Introduction

Accurate estimates of air temperature are essential for understanding and modelling environmental processes in mountain regions. The predominant source of mesoscale to microscale spatial temperature variability in mountains is associated with elevation through the near-surface air temperature lapse rate. In contrast to the free-air lapse rate that represents temperature changes along a vertical profile through the boundary layer and into the free

atmosphere, the near-surface air temperature lapse rate (hereafter, lapse rate) represents temperature variability within the surface layer (McCutchan, 1983). The lapse rate is therefore a key parameter for resolving local conditions in many environmental models that consider topoclimate variability in montane regions. However, guidance on estimating lapse rates is lacking, despite the fact that hydrological and ecological modelling efforts can be highly sensitive to the choice of lapse rate parameter used to infer fine-scale spatial temperature fields (Sekercioglu et al., 2008; Gardner and Sharp, 2009; Immerzeel et al., 2014). For example, Minder et al. (2010) showed that the application of contrasting lapse rates (-4 and $-6.5^{\circ}\text{C km}^{-1}$) to a snow model resulted in a 1-month difference in snowmelt commencement in the Washington Cascades, United States. Accurate lapse rate estimates are also needed to detect and project future elevation dependent warming (Pepin et al., 2015).

In practice, the lapse rate is often assumed to equal the mean environmental lapse rate (MELR) of $-6.5^{\circ}\text{C km}^{-1}$. Yet, observations show large variability of lapse rates geographically, seasonally, diurnally, and with elevation (Rolland, 2003; Lundquist and Cayan, 2007; Shen et al., 2016; Navarro-Serrano et al., 2018). The latter results in nonlinear lapse rates, although this is rarely acknowledged in modelling contexts. Mechanistic explanations for lapse rate variability include radiative processes, thermodynamics, and atmospheric dynamics (Harding, 1979; Blandford et al., 2008; Kattel et al., 2013; Navarro-Serrano et al., 2018).

Despite basic understanding of these processes, it remains difficult to constrain lapse rate estimates with observational data. Figure 2.1 illustrates this challenge showing summer temperatures across a longitudinal transect of the Oregon Cascades, United States. Station observations are a sample of the spatial temperature field. The default assumption that the full population of station observations is optimal for estimating the lapse rate has not been evaluated. Lapse rate estimates can be confounded by varied topoclimatic controls across a region of interest, which may help explain the diversity of lapse rates estimated using varied sample configurations (e.g., Figure 2.1b, c). Hence, while it is conceptually easy to calculate

a lapse rate, the statistical approach and station characteristics merit more careful consideration than typically given.

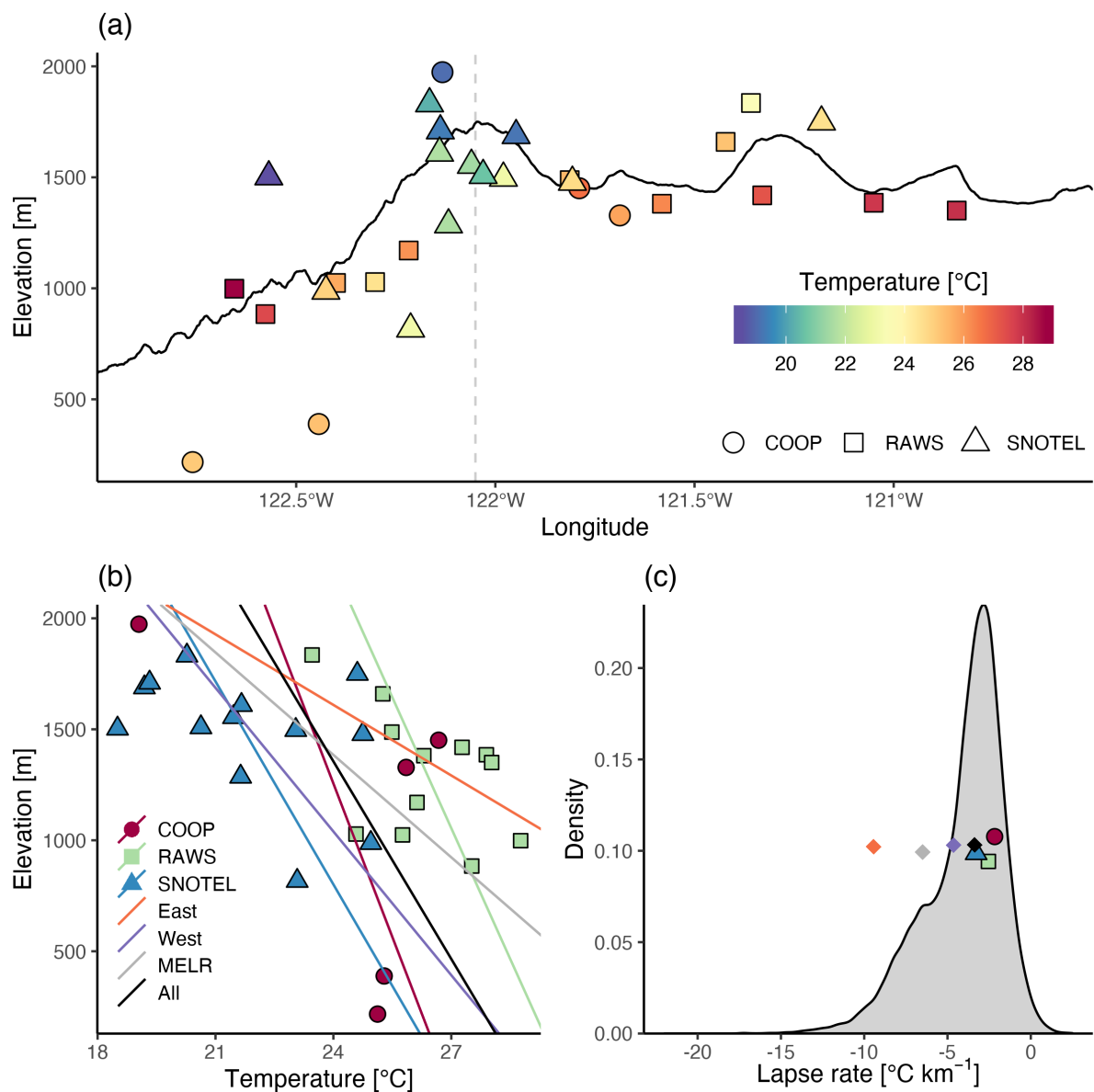


Figure 2.1 a) Black line shows mean elevation across longitude over the study domain of the Oregon Cascades, USA (42.8- 44°N, 120.5-123°W). Colored points show mean summer maximum temperature from 30 weather stations with symbols indicating the originating network. Vertical grey dashed line marks the maximum elevation of the transect and divides the stations into west and east groups. b) Examples of lapse rates calculated from these stations, including using only sites from the US Cooperative Observer Program (COOP), the US Interagency Remote Automatic Weather Stations network (RAWS), the US Natural Resources Conservation Service Snowpack Telemetry network (SNOTEL), only sites east or west of the divide, the mean environmental lapse rate (MELR, $-6.5\text{ }^{\circ}\text{C km}^{-1}$), or all stations ($n=30$). c) Distribution of lapse rates estimated from 15,000 samples of 10 stations from the full population shown in a). Colors and symbols in c) indicate lapse rates shown in b). Vertical jitter has been added to points in c).

Lapse rates are typically estimated via either simple linear regression (SLR) of temperature on elevation or multiple linear regression (MLR) of temperature on elevation and other covariates using a local population of observations (e.g., Pepin et al., 1999; Rolland, 2003; Kattel et al., 2013); it remains unclear whether SLR or MLR is more appropriate. Additionally, these approaches may be confounded by factors exogenous to elevation but collinear with elevation, including topographic position, land cover, soil moisture, and snow cover (Rolland, 2003; Dobrowski et al., 2009; Kattel et al., 2013; Navarro-Serrano et al., 2018). Collinearity is common among empirical approaches designed to isolate a single phenomenon and contributes to biased and unstable parameter estimates in SLR and MLR (e.g., Graham, 2003; Dormann et al., 2013). Another key consideration in calculating lapse rates is sample size. Studies have used as few as two up to tens of stations (Kirchner et al., 2013; Li et al., 2013). A further question is which stations should be used. Recognizing the role of topoclimatic factors in both determining and, in the context of collinearity, confounding lapse rates it may be appropriate to estimate lapse rates from stations with similar topoclimatic characteristics.

Given the importance of accurate lapse rates to environmental understanding and modelling, efforts to improve lapse rate estimation methods offer cascading benefits. This study quantifies the uncertainty and error in lapse rate estimates stemming from dataset characteristics and methodological choices by complementing observational data with synthetic data. In addition to standard SLR and MLR methods for lapse rate estimation we introduce a novel method that identifies samples of stations that are topoclimatically self-similar. Finally, we provide recommendations on best practices for lapse rate estimation that are applicable in any geographic or temporal context.

Data

A collection of stations traversing the Cascade Mountains of Oregon, United States (42.8–44°N, 120.5–123°W) was selected to exemplify complex terrain and land surfaces typical of mountain regions (Figure 2.2). The western, maritime portion of the domain is largely mesic and forested whereas the eastern portion in the rain shadow of the Cascade Mountains is largely semi-arid with mixed forest and shrubland. Observational data were

complemented by a suite of synthetic datasets with prescribed lapse rates. The following sections provide details of the synthetic, observational, and covariate datasets.

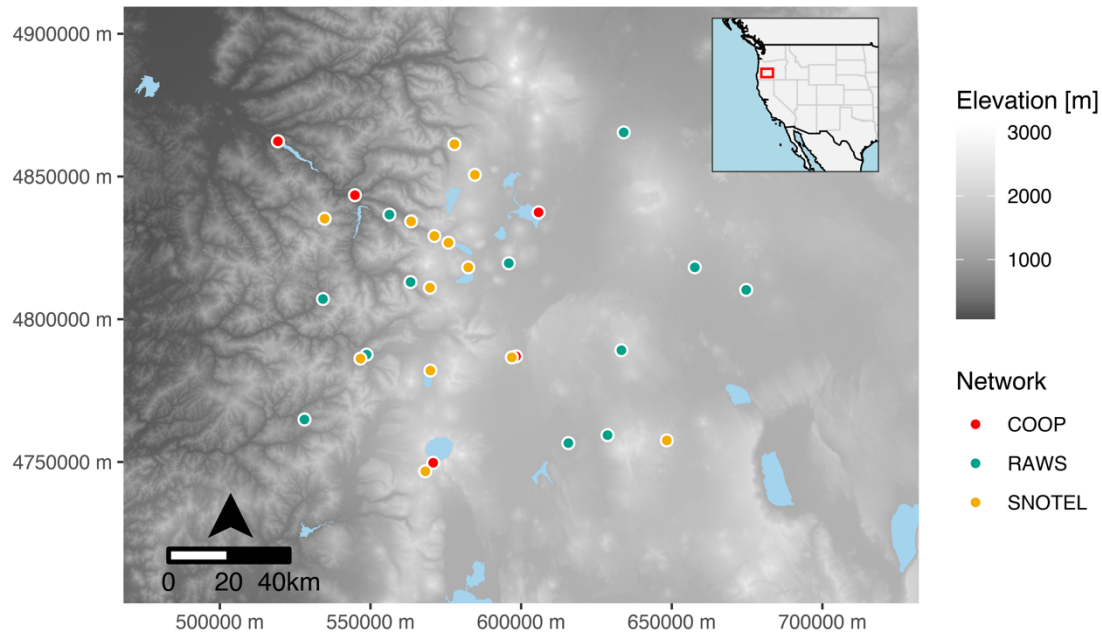


Figure 2.2 Oregon Cascades study area. Red box in inset map shows location of Oregon Cascades study area in Western North America. The 30 meteorological stations used in this study are indicated by markers according to the observation network. Light blue polygons are waterbodies.

Synthetic Datasets

The true lapse rate in a given observational setting is rarely known, impeding efforts to formally evaluate empirical lapse rate approaches. As an alternative, we developed synthetic temperature datasets with a prescribed lapse rate and fully quantified covariates. Nine synthetic datasets were developed that considered different levels of dataset noise and topoclimatic collinearity with elevation. Synthetic datasets had the same number of ‘stations’ ($n = 20$) at the same elevations with a prescribed lapse rate of $-6.5^{\circ}\text{C km}^{-1}$. Dataset noise (e.g., sensor error, data transcription errors, temperature variations not explained by other covariates) was quantified as the standard deviation of the random error term and was prescribed at three levels: 0.1, 1, and 2°C . Dataset collinearity was quantified as the correlation (r) between elevation and a prescribed covariate, solar radiation, at three levels: 0.00, 0.30, and 0.60.

Station temperatures were calculated as the sum of the temperature effects of three conceptual covariates and the random error term:

$$T_{s,ds} = T_{elev,s,ds} + T_{srads,s,ds} + T_{coast,s,ds} + T_{\varepsilon,s,ds}$$

Equation 2.1

where T is the temperature at station s in dataset ds , and T_{elev} , T_{srads} , T_{coast} , and T_{ε} are the temperature effects of elevation, solar radiation, distance from coast, and random error, respectively. Further details can be found in Appendix A.

Observational Datasets

Daily minimum (Tmin) and maximum temperature (Tmax) during September 1, 2005–August 31, 2015 for stations in Oregon were acquired from the Global Historical Climatology Network – Daily dataset (GHCND v3; Menne et al., 2012). We discarded values that were flagged for quality control. The remaining data were subject to completeness requirements such that stations were included if all years reported $\geq 85\%$ of daily values (Daly et al., 2008). Seasonal (DJF, MAM, JJA, SON) average temperatures were computed for seasons with $\geq 85\%$ of daily values reported, years with seasonal values reporting $< 85\%$ of daily values were set to missing, and annual and seasonal averages at each station were computed from at least 7 (out of a possible 10) data points. This resulted in 30 stations with Tmax and Tmin records covering the Oregon Cascades region of interest and spanning elevations from 217 to 1974 m (Figures 2.1 and 2.2). The dataset includes stations from the U.S. Cooperative Observer Program (COOP) network ($n = 5$), the U.S. Natural Resources Conservation Service Snowpack Telemetry (SNOTEL) network ($n = 13$), and the U.S. Interagency Remote Automatic Weather Station (RAWS) network ($n = 12$).

We selected covariates representative of known sources of non-elevational temperature variability in mountains (Table 2.1). Details of covariate data sources and calculations are provided in Appendix A. Covariates were estimated for each station, and in the case of time varying metrics, for seasonal and annual averages.

Table 2.1 Covariates used to account for non-elevational effects on temperature. Additional information is available in Appendix A.

COVARIATE	RELEVANT PROCESS	DATA SOURCE
SOLAR RADIATION	Surface energy budget	WRF
TOPOGRAPHIC CONVERGENCE INDEX (TCI)	Cold air pooling, coupling to free atmosphere	SRTM
CLOUD COVER	Shading during daytime, enhanced longwave radiation	MODIS
OROGRAPHIC UPSLOPE WIND INDEX (WINDEX)	Cloud cover, latent heating due to upslope condensation	ERA-Interim Reanalysis, SRTM
DISTANCE FROM COAST	Moisture availability, cloud cover, Bowen ratio	
WATERBODY INDEX	Surface energy budget	NHDPlus V2
FREE-AIR TEMPERATURE	Broad scale atmospheric conditions	ERA-Interim Reanalysis
FREE-AIR LAPSE RATE	Atmospheric stability	ERA-Interim Reanalysis

Methods

Regression Approaches

We employ two common approaches to estimate temperature lapse rates: simple linear regression (SLR) and multiple linear regression (MLR). In SLR, temperature is regressed on elevation, such that

$$T = \beta_0 + \beta_1 \times elev + \varepsilon$$

Equation 2.2

where T is the temperature at a given place and time, β_0 is the temperature at reference sea level, β_1 is the lapse rate, $elev$ is the elevation, and ε is the error. This approach assumes that temperature varies only as a function of elevation, disregarding additional topoclimatic factors known to affect temperature. Non-elevational factors that influence temperature but are not correlated with elevation will be subsumed within the error term. However, if these other factors are correlated with elevation, then SLR will alias these factors, making the lapse rate a derivative of temperature with respect to elevation, instead of a partial derivative.

In MLR, temperature is regressed on elevation and other variables, such that

$$T = \beta_0 + \beta_1 \times elev + \beta_2 \times X_2 + \dots + \beta_n \times X_n + \varepsilon$$

Equation 2.3

where the additional $n - 1$ terms β_2 through β_n are coefficients for the additional $n - 1$ predictor variables X_2 through X_n . The present study uses covariates of elevation, solar radiation, and distance from coast, which explain a large portion of temperature variability across the domain (Figure A.1). The number of covariates was limited to three and MLR lapse rates were not calculated for samples of <4 stations for this example in order to avoid overfitting. A potential hazard in the MLR approach is the assumption of noncollinearity of covariates; collinearity between elevation and other predictor variables can produce large uncertainties in estimated lapse rates (Dormann et al., 2013).

We further evaluated the effect of sample size on the robustness of lapse rates by running calculations for every combination of stations from two to the population size. Due to computational limitations, we restricted the number of station combinations (i.e., samples) for a given sample size to 15,000.

Domain Selection

Spatial variability of lapse rates has been documented for many regions (Wolfe, 1992; Rolland, 2003; Li et al., 2013), motivating a domain selection process for grouping stations based on climatic and physiographic factors. We used an empirical clustering approach based on known regional climate gradients and previous work documenting windward-leeward contrasts in lapse rates (Minder et al., 2010). Regionalizing climate stations is commonly done to isolate stations in terms of certain climate phenomenon (Abatzoglou et al., 2009). Clustering was based on covariates that capture large scale climatic and moisture gradients: the upslope flow index (hereafter, windex) and the free-air lapse rate. The windex provides an indication of linear orographic flow (product of the lower tropospheric flow and local terrain gradient, see Appendix A) and the free-air lapse rate provides an indication of broad scale atmospheric stability calculated directly from pressure level reanalysis or radiosonde data (Minder et al., 2010). Clusters based on seasonal values of the 40 km windex and free-air lapse rates were assessed using a k -means approach with $k=2$ and 10 random starting clusters. Lapse rates estimated from the resulting clusters were compared with one another and with lapse rates estimated from the full population.

Accounting for Regional Climate

Ideally lapse rates are estimated over small domains with little contrast in regional climate, however the paucity of observational stations in mountains often necessitates the use of larger domains (>100 km). Large domains may have significant spatial climatic gradients not directly tied to elevation (e.g., solar radiation, circulation patterns, continentality), making it difficult to isolate elevation-temperature relationships. In these contexts, it is useful to consider near-surface temperatures as a function of regional climate and topoclimatic siting (Lundquist et al., 2008; Dobrowski et al., 2009; Sadoti et al., 2018). This framing contrasts with traditional SLR and MLR methods which do not recognize the effect of regional climate on near-surface temperature.

We use free-air temperatures collocated with stations and at a fixed elevation (2,500 m was used in this analysis, the approximate height of the Cascade crest) derived from ERA-Interim (Appendix A) as a proxy for spatially varying temperatures that do not entrain elevational controls. Spatially corrected station temperatures (T_{sc}) are calculated as the difference between station temperatures and free-air temperatures. While previous studies have used free-air temperatures to account for temporal temperature variability (e.g., Dobrowski et al., 2009), here we use free-air temperatures to account for spatial temperature variability. We evaluate lapse rates estimated from SLR in which T_{sc} is substituted for station temperature as the dependent variable.

Identifying Influential Stations

Data points with high leverage and an anomalous predictor-response value combination can strongly influence linear regression coefficients (Altman and Krzywinski, 2016). In the context of lapse rates, the highest and lowest elevation stations can exert outsized influence on the lapse rate estimate if their temperatures are poorly predicted by a model based on the other stations. We quantify the influence of each station using Cook's Distance (Cook, 1977). Stations with Cook's Distances exceeding four divided by the population size in all seasons are considered influential and are considered for exclusion from lapse rate calculations (Altman and Krzywinski, 2016). For brevity, we only evaluate station influence for a subset of the Oregon Cascades stations.

Topoclimatic Dissimilarity Approach (TDA)

To improve lapse rate estimates in the context of collinear covariates, one can minimize the temperature variance explained by non-elevational factors. One way to accomplish this is to a priori develop lapse rates based on stations that occupy similar topoclimatic siting for covariates except elevation. For example, solar radiation will be a less important predictor of inter-station variability in Tmax for a sample where all sites have similar radiational loading than in a sample with large differences in solar radiation. These arguments form the basis for a new lapse rate estimation method, termed the Topoclimatic Dissimilarity Approach (TDA). The TDA is conceptually similar to the Parameter-elevation Relationships on Independent Slopes Model (PRISM; Daly et al., 2002), in that stations are selected or weighted based on topoclimatic characteristics, however the specific methods and goals differ.

The TDA is a sample selection algorithm which preferentially minimizes the range of values of non-elevational factors according to the amount of temperature variability the factor explains. The correlations (r_v) between each covariate (v) and temperature across the full population of stations are used to weight each covariate. Weightings are applied as the square root of the absolute values of r_v . Using the full population, each covariate is then converted to standardized anomalies so that covariates can be compared. We calculate the range of standardized anomalies (R_v) for each covariate across each sample. Elevation ranges are subtracted from the maximum elevation range of all the samples to allow the algorithm to maximize the range of elevation while minimizing the ranges of all other covariates. A topoclimatic dissimilarity metric (TD) is then computed as the weighted maximum distance for each sample:

$$TD = \sum_{v=1}^p \sqrt{|r_v|} \times R_v$$

Equation 2.4

where p is the number of covariates evaluated. TD quantifies the topoclimatic dissimilarity of each sample, with lower values representing more topoclimatically self-similar samples. In subsequent analyses, TDA results are presented grouped in deciles of TD to elucidate the potential value of self-similar samples. Covariates included in the TDA algorithm as used in this study are elevation, TCI, cloud cover, windex, distance from coast, and the waterbody

index for the observational data and elevation, solar radiation, and distance from coast for the synthetic datasets. This algorithm is available as an R script at https://github.com/abbylute/lapse_rate_TDA.

In addition to comparing lapse rates from TDA to lapse rates from randomly sampled stations, we evaluated potential advantages of using TDA compared to using SLR with an entire population to determine whether the benefits of TDA outweighed the benefits of a larger sample. For each synthetic dataset, we drew all possible subpopulations of each size (N_{sub}) from 4 to 19. For N_{sub} with >100 subpopulations, we randomly selected 100 from the list of all possible subpopulations. From each subpopulation, we similarly drew up to 100 random samples of each size from 2 to $N_{sub} - 1$. We applied the TDA to each of these subpopulation-sample size combinations. Finally, we compared the error of the median lapse rates from the samples with TD in the lowest decile to the lapse rate error from SLR applied to the subpopulations.

Assessment Metrics

Lapse rate error was quantified as the difference between the specified lapse rate ($-6.5^{\circ}\text{C km}^{-1}$ for the synthetic datasets) and the estimated lapse rate. We use mean absolute error (MAE) to quantify the average lapse rate error and mean error to quantify lapse rate bias. Error was not quantified for the observational dataset because the true lapse rate is unknown.

Lapse rate uncertainty for both the observational and synthetic datasets was quantified as the interquartile range (IQR) of the lapse rate estimates. Differences in uncertainty are used to assess improvements in observational lapse rate accuracy.

Initial results for both datasets are presented for a sample size of 5 since this is representative of sample sizes used in the literature (e.g., Blandford et al., 2008; Gardner et al., 2009; Kirchner et al., 2013; Li et al., 2013). Later results are presented for multiple sample sizes or for sample sizes determined to be more appropriate based on intermediate results.

Results

Synthetic Datasets

Lapse Rate Sensitivity to Collinearity, Dataset Noise, Sample Size, and Method

Lapse rate uncertainty and error were typically greater for datasets with high dataset noise, high collinearity, small sample sizes, or when MLR was used (Figures 2.3 and 2.4). For samples of 5 stations, we found that increased dataset noise increased the uncertainty and MAE of SLR and MLR lapse rate estimates (Figure 2.3). Secondly, increased collinearity increased the bias of SLR lapse rate estimates (Figure 2.3a). The bias was positive in this case due to the way the collinearity was prescribed in the synthetic datasets (i.e., a positive correlation between elevation and solar radiation aliases the lapse rate to other processes). Thirdly, the response of MLR estimates to collinearity was less consistent than for SLR, likely due to interactions with noise which affected the collinearity structure; dataset noise can be aliased by other covariates and contribute to additional collinearity and therefore additional error. Except for cases with low noise (0.1°C), SLR generally outperformed MLR.

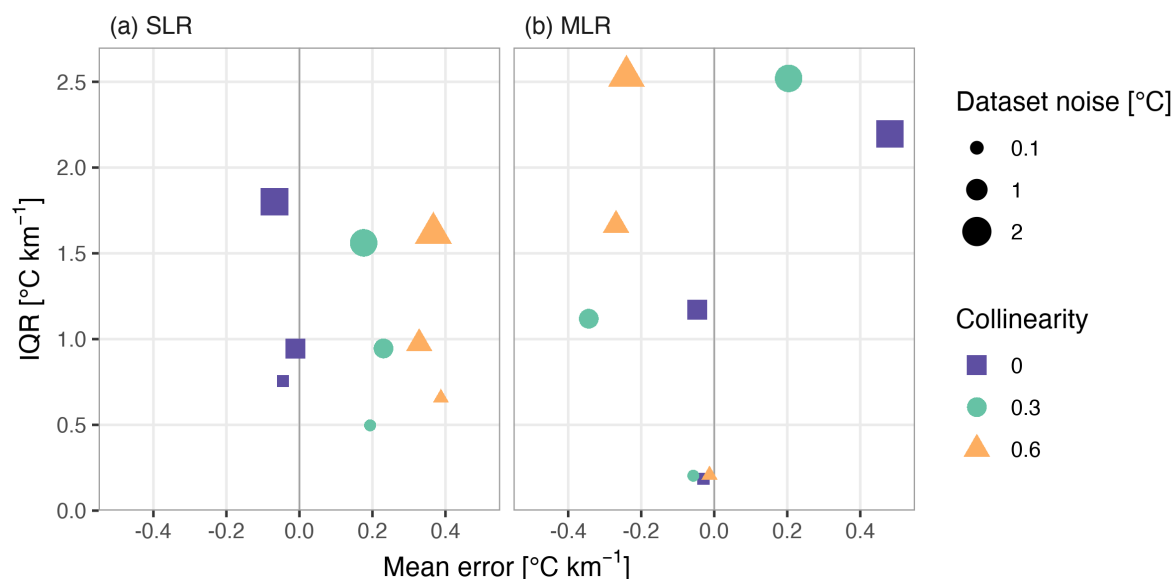


Figure 2.3 Lapse rate mean error (x-axis) and interquartile range (y-axis) estimated via a) SLR and b) MLR for datasets with varying levels of dataset noise (size) and collinearity (color, shape). Lapse rates are estimated from samples of 5 stations drawn from each synthetic dataset.

We next compared the sensitivity of lapse rate MAE to sample size across the matrix of estimation method, collinearity, and dataset noise. MAE increased with increased collinearity, increased dataset noise, or decreased sample size in almost every case (Figure 2.4). Firstly, MAE increased exponentially with decreasing sample size and was

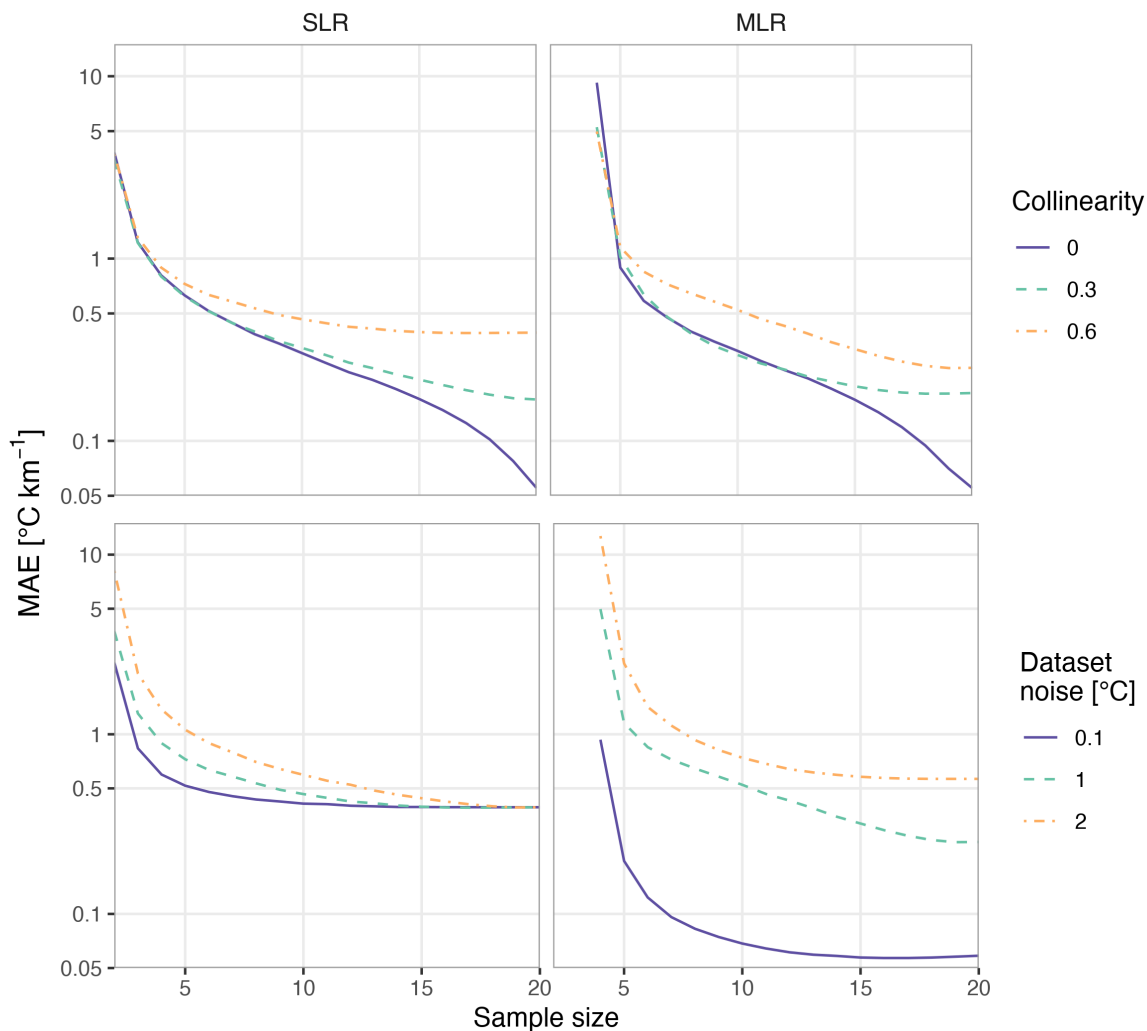


Figure 2.4 MAE of lapse rates (log scale on y-axis) estimated from synthetic datasets using SLR (left column) and MLR (right column). MAE is calculated across all possible samples of the sample size indicated on the x-axis. In the upper plots each line represents a synthetic dataset with a different collinearity level and with dataset noise of 1°C, in the lower plots each line represents a dataset with a different level of dataset noise and with collinearity of 0.6.

typically $<1^{\circ}\text{C km}^{-1}$ for sample sizes of at least 5 stations. Small samples were more likely to span a small elevation range (<500 m) than larger samples, which amplified the effect of non-elevational factors on the lapse rate (not shown) and increased uncertainty. Secondly, SLR lapse rate estimates had lower error than MLR estimates for small sample sizes (5 or less), greater collinearity, and greater dataset noise. Small samples can have greater collinearity (both from latent covariates and aliased from dataset noise) than the population as a whole, resulting in larger MAE, particularly for MLR. MLR slightly outperformed SLR for cases with low to moderate dataset noise and collinearity and sample sizes >5 . These

results mirror conclusions of other statistical efforts that consider the interacting effects of noise, collinearity, sample size, and regression method on the bias and uncertainty of regression coefficients in other disciplines (Mason and Perreault Jr., 1991).

Application of Topoclimatic Dissimilarity Approach to Synthetic Datasets

Compared to all samples, the most self-similar samples generally had lower lapse rate MAE and uncertainty (Figure 2.5). The TDA was effective at reducing error and uncertainty for small samples, since small samples from a finite population provide more diversity to choose from than larger samples which have many stations in common and offer limited flexibility. The TDA also reduced error and uncertainty for large samples, which had low

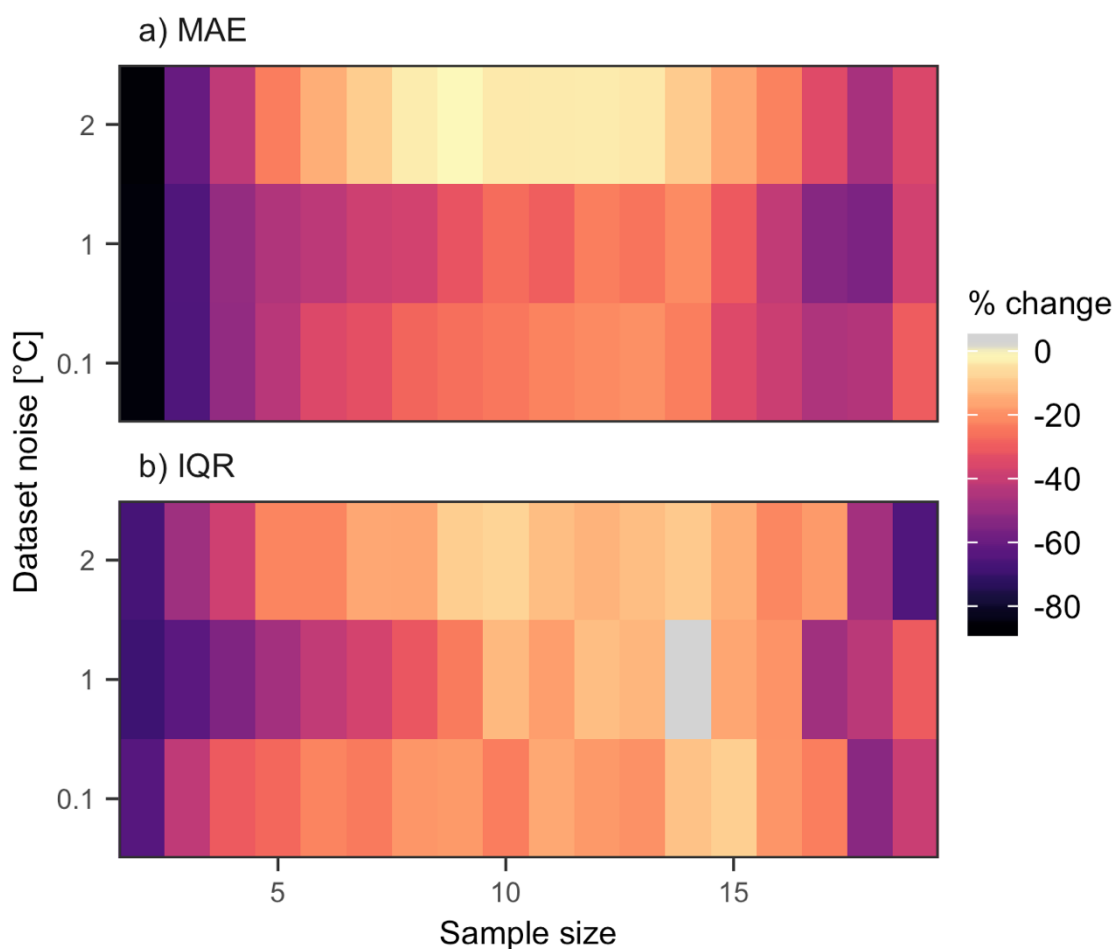


Figure 2.5 Percent change in a) MAE and b) IQR between the most similar decile of samples selected using TDA and all samples. Results are shown for lapse rates estimated via SLR from samples of varying sample size (x-axis) drawn from datasets with collinearity of 0.3 and varying dataset noise (y-axis). Negative values indicate that the most similar decile had lower MAE or IQR than the average sample. Positive values (grey) indicate increased MAE or IQR.

error initially (Figure 2.4), suggesting that omission of just one to a few outlier stations can greatly reduce lapse rate error. Low uncertainty does not necessarily equate to better lapse rates with lower error; it is possible to have low lapse rate uncertainty but large lapse rate error. However, across the synthetic datasets lower IQR typically corresponded to lower MAE (e.g., Figure 2.5), suggesting that this definition of uncertainty may be a proxy for error in the observational datasets.

The median lapse rate from the most similar decile of samples, evaluated for all sample sizes, dataset noise, and collinearity levels, had absolute error $< 0.5^{\circ}\text{C}$ in 84% of cases, compared to 67% of cases for all possible samples. The median lapse rate from the most similar decile provides a good best guess at the actual lapse rate and the minimum and maximum lapse rates from the most similar decile may be useful as a measure of lapse rate uncertainty.

Median lapse rates from the most similar decile of samples had lower MAE than lapse rates estimated from subpopulation-based SLR in some cases (Figure 2.6), with MAE being an average of 12% lower ($-0.04^{\circ}\text{C km}^{-1}$) for subpopulation size >5 and sample size $\geq 80\%$ of the subpopulation size. Given the larger uncertainty of the observational data ($3.5^{\circ}\text{C km}^{-1}$ on average for the SLR results shown in Figure 2.7) compared to the synthetic data ($1^{\circ}\text{C km}^{-1}$ for sample size of 5 for datasets with 1°C noise), we expect larger absolute error reduction for the TDA applied to the observational data. In many cases, lapse rates estimated from the TDA using a sample size of 2 had lower error than the full subpopulation, illustrating that it is possible to calculate an accurate lapse rate from only two stations. However, error reduction was more consistent for samples sizes that were roughly $\geq 80\%$ of the subpopulation size. For the middle range of sample sizes, the TDA was not beneficial; middle range sample sizes had neither the flexibility of small samples to choose the best stations nor the robustness of the larger samples. Finally, for subpopulation sizes roughly ≤ 5 , the TDA was not consistently beneficial. In these cases, the median of lapse rates estimated from all possible station combinations of size 2 to the subpopulation size $- 1$ typically was as accurate or more accurate than the full subpopulation lapse rate (not shown).

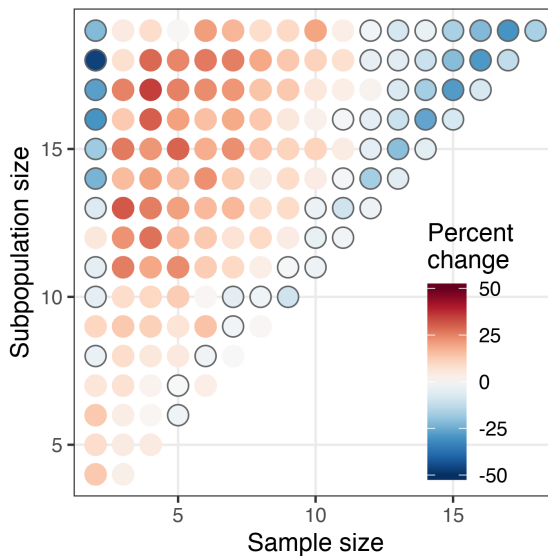


Figure 2.6 Percent difference in MAE between lapse rates of varying sample size (x-axis) selected by TDA (i.e., the median lapse rate from the most similar decile of samples) and lapse rates calculated from the full subpopulations using SLR (subpopulation size shown on y-axis). Blue, outlined points indicate reduced MAE. Data is from the synthetic dataset with noise of 1°C and collinearity of 0.6.

Oregon Cascades Station Dataset

Lapse Rate Estimation Method and Sample Size

Seasonal lapse rates estimated via MLR from samples of 5 stations from the Oregon Cascades had uncertainty $>5^{\circ}\text{C km}^{-1}$ (Figure 2.7). Tmax lapse rates estimated via SLR were generally weaker than those estimated via MLR, while the opposite was found for Tmin. The uncertainty of SLR estimates was generally smaller than for MLR, which is expected since SLR regression coefficient variance is a function of sample size and noise, whereas MLR coefficient variance is additionally a function of collinearity (Mason and Perreault Jr., 1991; Montgomery et al., 2012). Uncertainty increased dramatically for samples smaller than 10 stations (not shown). Combined with the results for the synthetic datasets, these results confirm the hypothesis of Rolland (2003) that small sample sizes can be a source of error in lapse rate estimates.

Free-air lapse rates showed limited seasonality and typically fell between the SLR and MLR estimates for T_{max} but were steeper than most SLR and MLR estimates for T_{min} . The steeper free-air lapse rates relative to near-surface T_{min} lapse rates is likely related to night-time atmospheric decoupling and cold air drainage (Lundquist et al., 2008; Daly et al., 2010).

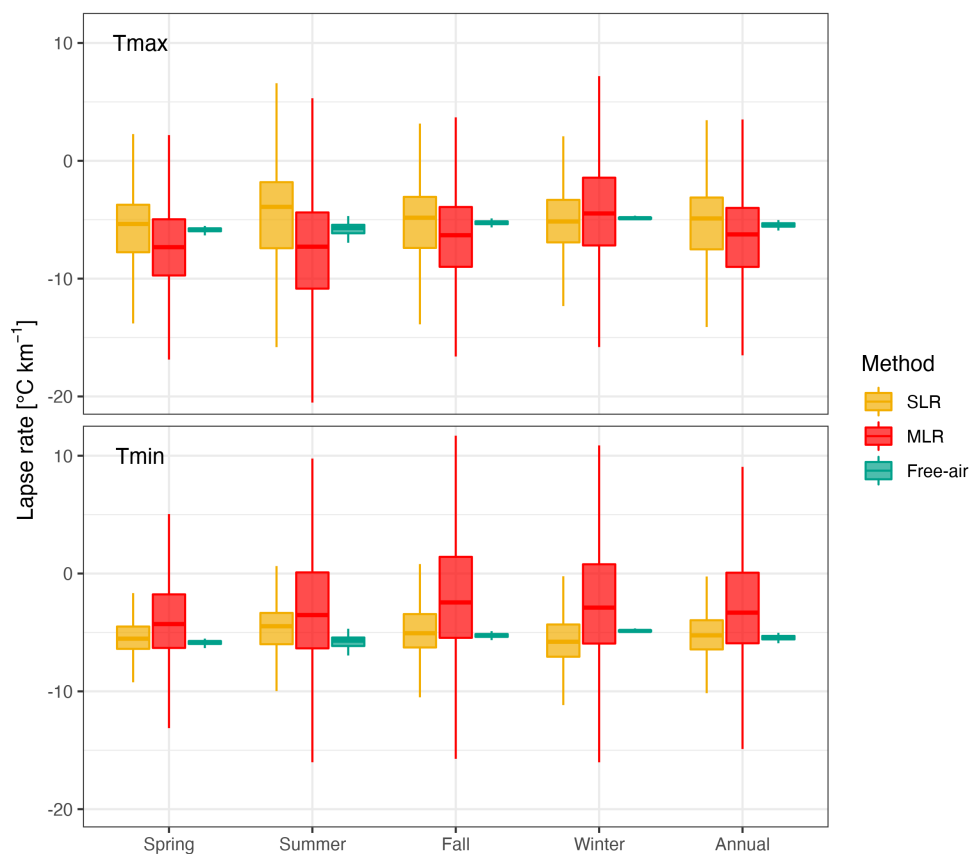


Figure 2.7 Lapse rates calculated from samples of five stations from the 30 stations in the Oregon Cascades dataset for T_{max} (top) and T_{min} (bottom). Yellow boxes indicate lapse rates calculated via SLR. Red boxes correspond to lapse rates calculated via MLR using elevation, solar radiation, and distance from coast as predictors. Green boxes indicate free-air lapse rates calculated from ERA-Interim reanalysis collocated with stations (see Appendix A for details) and are the same for T_{max} and T_{min} .

Collinearity

One might expect that the predictor variables in the MLR (elevation, solar radiation, and distance from coast) would capture the key processes controlling spatial variability in temperature and provide more refined lapse rate estimates than SLR. However, MLR increased lapse rate uncertainty due to collinearity between elevation and additional predictor variables (e.g., the correlation between elevation and distance from coast was 0.57;

Figure A.1). Recognizing this collinearity and the large uncertainty in MLR lapse rates (Figure 2.7), we focus on SLR lapse rates for the remainder of the paper. For brevity, we only present results for Tmax to illustrate our methods.

Accounting for Spatial Variability of Lapse Rates Through Domain Selection and Spatial Temperature Correction

We evaluated two methods of accounting for spatial variability of lapse rates: a spatial clustering approach and a spatial temperature correction. Spatial clustering aims to identify contrasting regional climates which may merit separate lapse rates whereas the spatial temperature correction is designed to address gradual climatic gradients not related to elevational differences. Therefore, we recommend assessing the potential for clustering first, and then spatial correction. Spatial correction can be applied with or without clustering.

The clustering analysis identified two clusters roughly corresponding to stations west and east of the Cascade crest, hereafter referred to as a windward ‘west’ cluster ($n = 17$) and a leeward ‘east’ cluster ($n = 13$) (Figure 2.8a). Tmax lapse rates from these clusters contrasted with lapse rates from the full population of stations (Figure 2.8b). ‘East’ cluster lapse rates were steeper than full population or ‘west’ cluster lapse rates, except in winter. The ‘east’ cluster had the greatest seasonality, with steeper lapse rates during summer and weaker lapse rates in winter when inversions are more common (Whiteman et al., 2001). The large uncertainty in the ‘east’ cluster may be partly due to the small elevation range of these stations (645 m) relative to those in the ‘west’ cluster (1,615 m), since small elevation ranges amplify the effects of non-elevational factors on the lapse rate. In contrast, ‘west’ cluster lapse rates were around $-5^{\circ}\text{C km}^{-1}$ with minimal seasonality. The east–west contrasts in lapse rates and in lapse rate seasonality are similar to the results of Minder et al., (2010) for the Washington Cascades. Coherent spatial patterns of lapse rates and lapse rate seasonality have also been identified in other regions including Spain and Northern Italy (Rolland, 2003; Navarro-Serrano et al., 2018).

In all seasons except winter, the median Tmax lapse rate from the full population was weaker than the median lapse rate from either of the clusters. This was most evident in summer, when ‘east’ stations were significantly warmer than ‘west’ stations at the same

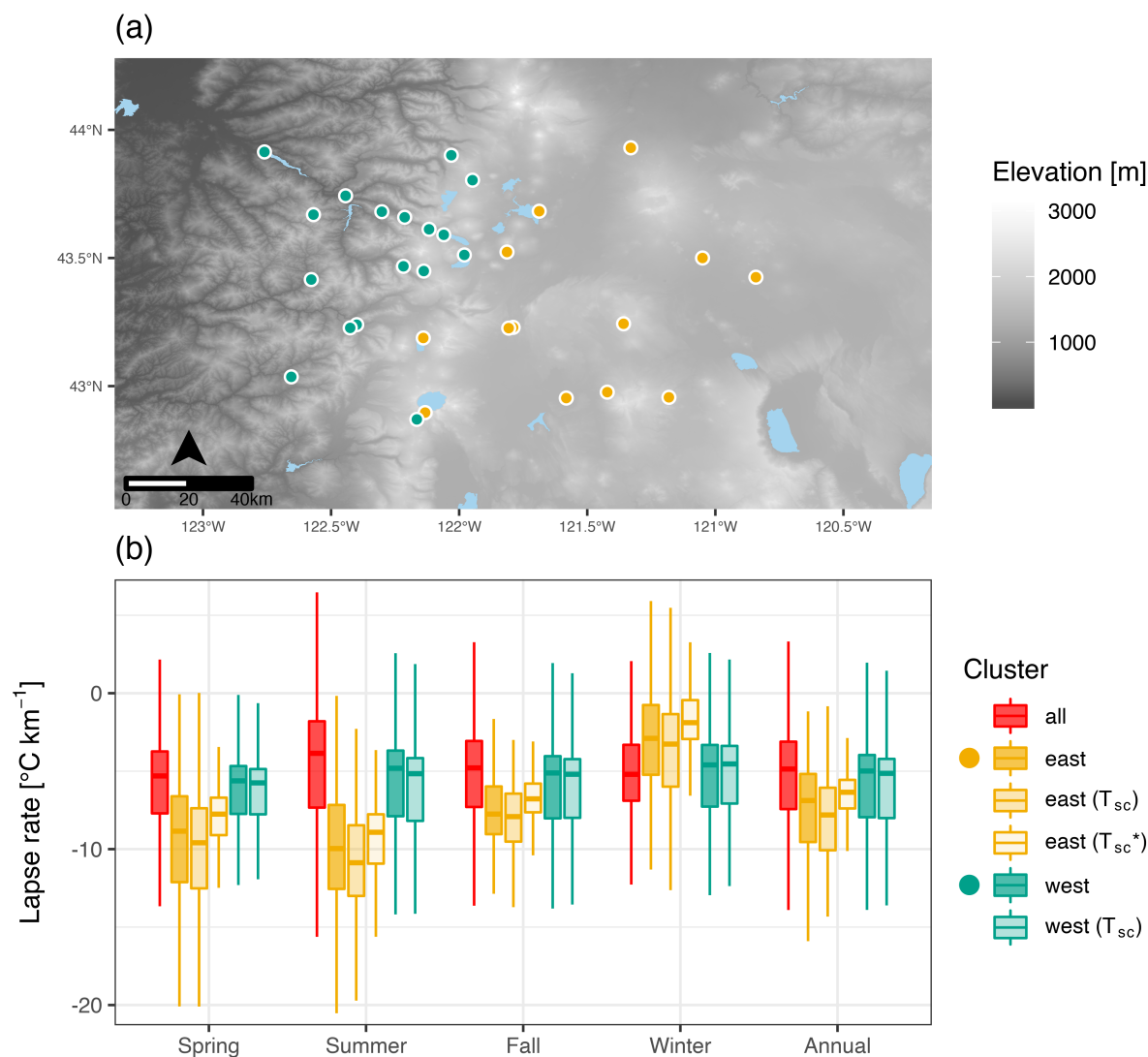


Figure 2.8 (a) Oregon Cascades domain with stations colored according to cluster, as indicated by boxplot legend. (b) Tmax lapse rates estimated via SLR from samples of 5 stations from the full dataset ('all', $n=30$), the 'west' cluster ($n=17$), and the 'east' cluster ($n=13$). T_{sc} indicates lapse rates estimated for the 'east' and 'west' clusters using spatially corrected station temperatures. T_{sc}^* indicates lapse rates estimated from spatially corrected temperatures from the 'east' cluster with influential stations removed ($n=12$).

elevation due to greater Bowen ratio and downward surface shortwave flux. The fact that the full population lapse rates do not represent the lapse rates in these subregions (similar to Rolland, 2003), and the strong and physically reasonable contrasts between 'east' and 'west' lapse rates motivate regionalization efforts when calculating lapse rates over large geographic areas.

Spatial correction of Tmax (T_{sc}) steepened lapse rates in the 'east' cluster, particularly in summer and generally reduced the uncertainty compared to lapse rates based on raw

station temperatures and increased the correlation between elevation and temperature (Figure 2.8b). An exception was the ‘east’ cluster in winter, likely because of the prevalence of persistent winter cold pool events in this region (Whiteman et al., 2001) which decouple near-surface temperatures from free-air temperatures. Considering all combinations of region, season, and sample size, T_{sc} reduced the lapse rate uncertainty in >75% of cases. The uncertainty reduction was typically on the order of tenths of $^{\circ}\text{C km}^{-1}$, but in some cases exceeded $1^{\circ}\text{C km}^{-1}$. The uncertainty reduction was greater for small samples and in summer as free-air temperatures in summer exhibit a longitudinal gradient across the study region. Similarly, we expect that the uncertainty reduction would be greater if applied to regions with larger differences in free-air temperature (e.g., larger geographic regions).

While clustering was most appropriate for this example, we also assessed the benefit of applying the spatial correction without clustering. Lapse rates estimated from spatially corrected temperatures from samples of 5 stations from the full dataset were generally steeper and had lower uncertainty than those estimated from uncorrected station temperatures (not shown). The largest improvements were seen in summer; the median lapse rate was $0.9^{\circ}\text{C km}^{-1}$ steeper and the IQR was $0.3^{\circ}\text{C km}^{-1}$ smaller. These results were similar to the clustering results, but the improvements were smaller.

Influential Stations in the Oregon Cascades Dataset

Application of Cook’s Distance to the ‘east’ cluster identified the highest elevation station, Crater Lake COOP station (GHCND ID: USC00351946), as influential. This station was colder in every season than would be expected based on lapse rates estimated from the other stations and would be excluded by the TDA if the TDA did not try to maximize sample elevation range. It is possible that this station could be indicative of a steeper lapse rate across high elevation portions of the domain, however this would require additional data to evaluate. We excluded this station from further analysis, which resulted in lapse rates that were $1.5\text{--}3^{\circ}\text{C km}^{-1}$ weaker than lapse rates based on the full cluster (Figure 2.8b). We reapplied Cook’s Distance after removing this station and no additional influential stations were identified. Hereafter, the ‘east’ cluster refers to the ‘east’ cluster with this influential station removed.

Application of Topoclimatic Dissimilarity Approach to the Oregon Cascades Dataset

Application of the TDA to the Oregon Cascades dataset, using spatially corrected station temperatures and sample sizes roughly 80% of the population size (13 and 10 for ‘west’ and ‘east’, respectively), resulted in contrasting lapse rate distributions across dissimilarity quantiles (Figure 2.9). The distributions of lapse rates in the most similar quantile were tightly clustered relative to distributions for less similar quantiles, suggesting that accounting for topoclimatic variability in station siting can improve temperature estimates (Lookingbill and Urban, 2003). In general, we expect the TDA to exclude dissimilar stations and reduce lapse rate error and uncertainty, however the specifics of which stations are excluded based on which covariates will depend on the dataset.

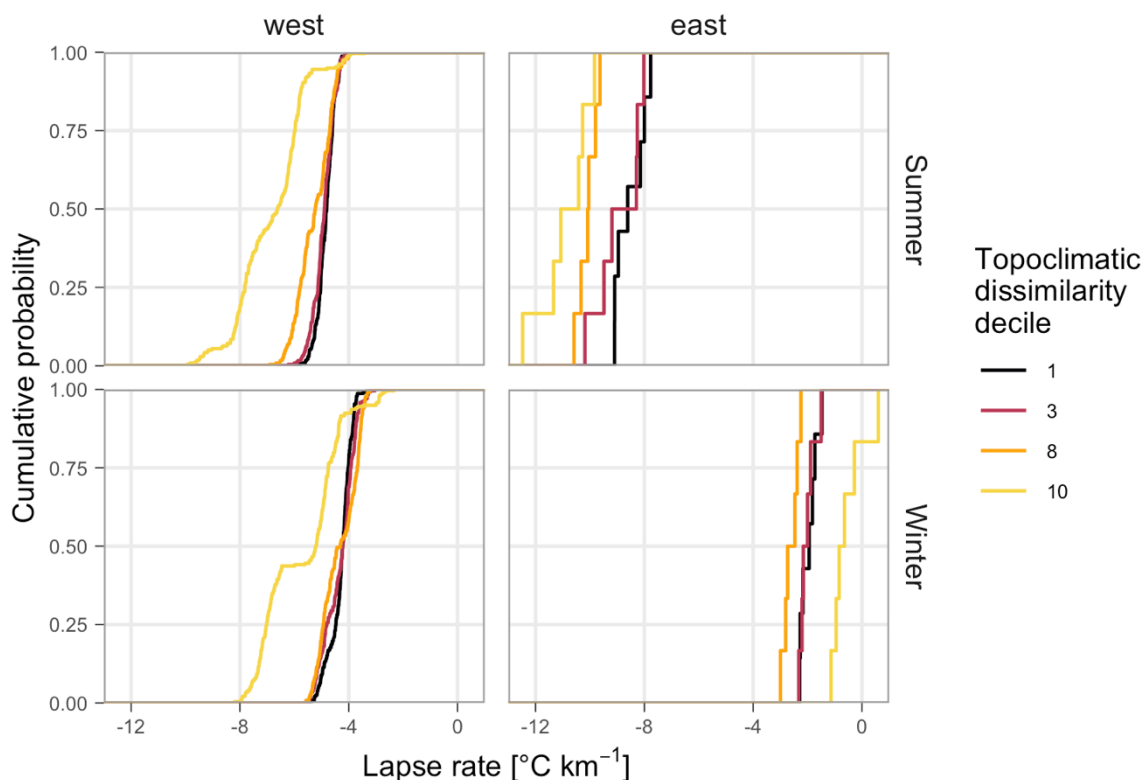


Figure 2.9 Cumulative distributions of spatially corrected Tmax lapse rates estimated from samples of stations from the ‘west’ (left column) and ‘east’ (right column) clusters of the Oregon Cascades dataset for summer and winter (rows). Sample sizes of 13 and 10 were used for the ‘west’ and ‘east’ clusters, respectively. Results are grouped by decile of the dissimilarity metric. Only deciles 1, 3, 8, and 10 are shown.

For the ‘west’ cluster in summer, cloud cover was the strongest predictor of temperature after elevation. In the most similar decile of samples, the TDA preferentially excluded the stations with the lowest and highest cloud cover values which were much

warmer and cooler, respectively, than expected, resulting in a weaker lapse rate. The most important non-elevation predictor of winter temperature in the ‘west’ cluster was distance from coast, however this variable was strongly correlated with elevation ($r = 0.78$) limiting the TDA from excluding this covariate in station selection for the most similar decile. Instead, stations with extreme values in the next most important predictors of temperature (the waterbody index and the 40 km windex) were excluded from the most similar decile.

The ‘east’ cluster lapse rates based on the TDA had greater seasonality than the ‘west’ cluster. Summer lapse rates for the ‘east’ cluster were steep, with a median of $-9.0^{\circ}\text{C km}^{-1}$ for the most similar decile. This was slightly weaker than the summer lapse rate calculated across all ‘east’ cluster stations ($-9.2^{\circ}\text{C km}^{-1}$) but is slightly steeper than the summer lapse rates found by Minder et al., (2010) for the lee side of the Washington Cascades. In the most self-similar decile of samples, the TDA excluded a site that was an outlier in terms of the 40 km windex, which was the covariate most strongly correlated with summer temperature ($r = -0.56$) after elevation ($r = -0.80$). Winter temperatures were as strongly correlated with the TCI as they were with elevation ($r \sim 0.41$), corroborating the importance of inversions and cold-air drainage effects in the ‘east’ cluster in winter. The TDA preferentially excluded the station with the highest TCI value from the most similar decile of samples.

Discussion

Our results document latent uncertainties in near-surface temperature lapse rate estimates. Standard approaches for calculating lapse rates using our example of stations in the Oregon Cascades showed uncertainty of $>5^{\circ}\text{C km}^{-1}$ in some cases (Figure 2.7). Given this uncertainty, it is unsurprising that the mean environmental lapse rate of $-6.5^{\circ}\text{C km}^{-1}$ is often used. However, the sensitivity of environmental models to lapse rate estimates (e.g., Gardner and Sharp, 2009) indicates that a one size fits all lapse rate parameter is not sufficient and that better lapse rate estimation methods are needed (e.g., Minder et al., 2010). The analyses presented above of observational and synthetic datasets point to a handful of best practices for lapse rate estimation (Figure 2.10) applicable to any timescale or geographic context, and to station data or gridded data (Cannon et al., 2012).

1. *Estimation method*: SLR provides more accurate and robust lapse rate estimates than MLR in situations with high collinearity and data noise or small sample sizes (Figure 2.4). MLR can provide extreme lapse rate estimates when collinearity exists, which is common in observational data (Figures 2.7 and A.1). Therefore, we recommend the use of SLR.
2. *Sample size*: Small samples are more sensitive than large samples to deviations in station temperature stemming from non-elevational factors. Evaluation of the TDA found that sample sizes that were roughly 80% of the population size struck a balance between the benefits of more data points and the benefits of being able to exclude dissimilar stations (Figure 2.6). We recommend using more than 5 stations and using sample sizes of about 80% of the population size when applying the TDA.
3. *Elevation Range*: Theory and exploratory data analysis indicate that lapse rate error increases dramatically as the sample elevation range decreases (Figure 2.8). Efforts should be made to collect data from a wide range of elevations, or barring this, a large number of stations, and the greater lapse rate uncertainty stemming from small elevation ranges should be taken into account in broader modelling efforts.
4. *Dataset Noise*: Analysis of the synthetic datasets illustrated that dataset noise increases lapse rate uncertainty and can increase bias (Figure 2.3). Efforts to quality control and correct for known sources of temperature bias, including removing influential stations, can reduce the uncertainty in lapse rate estimates.
5. *Collinearity*: Collinearity of elevation with non-elevational factors influencing temperature is common in observational data and affects lapse rate estimates (Figures 2.3 and 2.4). Selection of self-similar samples (e.g., using the TDA) can reduce the effects of collinearity and improve lapse rate estimates (Figures 2.5 and 2.6). Topoclimatic variables used to assess collinearity and sample self-similarity should be tailored to reflect processes relevant to the region and time period of interest.
6. *Domain selection*: Lapse rates estimated from windward and leeward clusters of stations showed distinct values and seasonality compared to those using stations from the full domain (Figure 2.8). This suggests that lapse rates should be estimated over

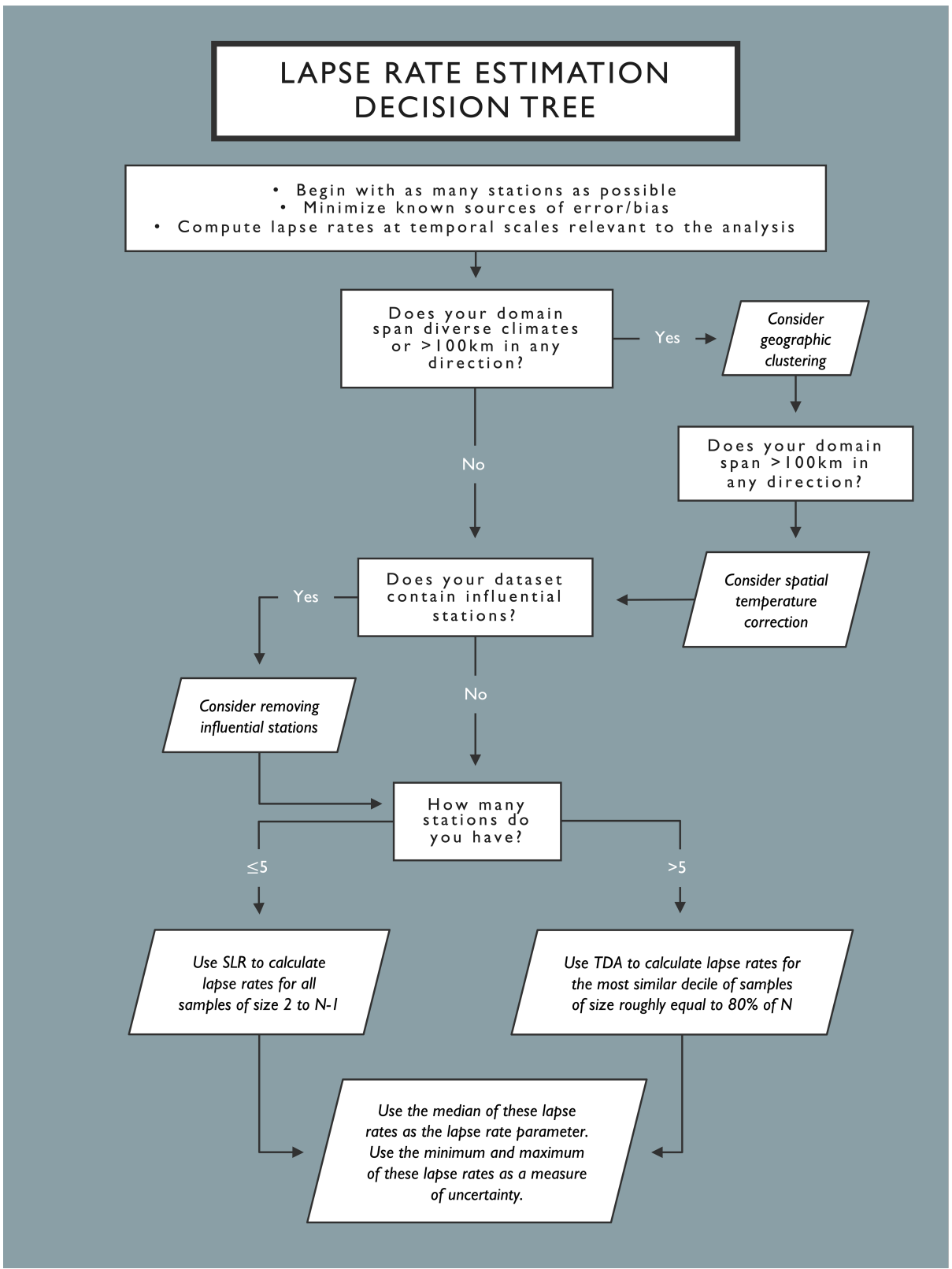


Figure 2.10 Decision tree outlining best practices for estimating near-surface temperature lapse rates. N is the total number of stations available (i.e., the population size).

regions without strong climatic discontinuities or should be estimated from spatially corrected temperatures.

7. *Uncertainty*: Given the large uncertainty in lapse rates documented here, we argue that lapse rate uncertainty should be incorporated in model uncertainty and sensitivity analyses when possible.

Using the best practices outlined above we estimated seasonal lapse rates and lapse rate uncertainty for the ‘west’ and ‘east’ clusters of the Oregon Cascades station data (Figure 2.11). Our results indicate lapse rates close to $2^{\circ}\text{C km}^{-1}$ different, on average, from those estimated from the full dataset without using best practices or from the commonly used MELR (similar to Navarro-Serrano et al., 2018; Shen et al., 2016).

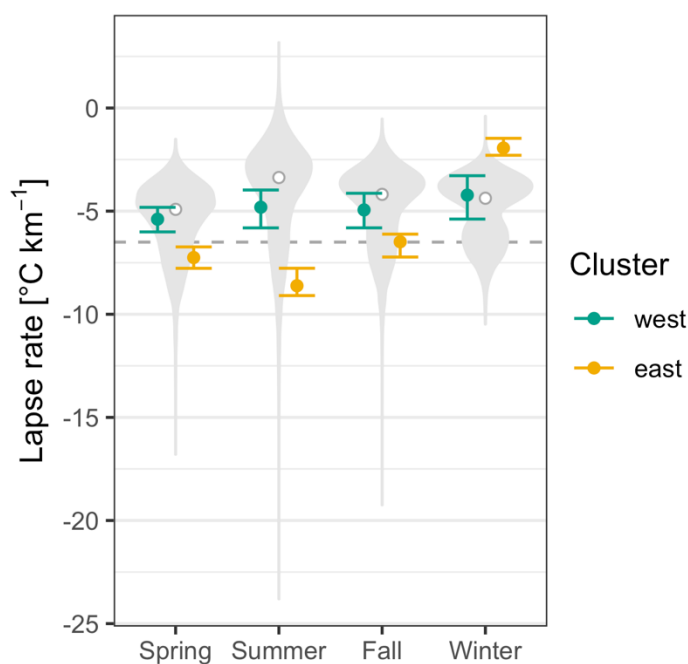


Figure 2.11 Seasonal Tmax lapse rates estimated for the Oregon Cascades stations following best practices. Colored points represent the single best lapse rate (i.e., the median lapse rate of the most similar decile of samples) and colored bars indicate uncertainty range (the minimum and maximum lapse rates of the most similar decile of samples). Grey violin plots illustrate the possible lapse rates that can be estimated from any combination of 10 stations from the original dataset, not using best practices. White dots indicate the lapse rate estimated from the full 30 station dataset not using best practices. The grey dashed line marks the MELR ($-6.5^{\circ}\text{C km}^{-1}$).

Conclusions

Temperature fields in environmental models dictate a wide range of processes including phenology, growing degree days, precipitation phase, snowmelt, and glacier mass balance, thereby exerting outsized influence on modelling outcomes. Yet these temperature fields are often governed by a single lapse rate parameter selected from the literature or calculated from a handful of stations within the modelling domain with little consideration of error or uncertainty. Contrasting but physically reasonable lapse rates (-4 and $-6.5^{\circ}\text{C km}^{-1}$) applied to an elevational range of 1 km can result in differences in model outcomes that are of similar magnitude to the difference between modelling outcomes based on historical and $+2^{\circ}\text{C}$ climate scenarios (Minder et al., 2010), emphasizing the importance of carefully choosing a lapse rate. We show that lapse rate uncertainty can easily exceed the range evaluated by Minder et al., (2010), suggesting that the effects of lapse rate uncertainty may exceed the effects of climate change in some modelling contexts.

The best practices presented here reduce lapse rate uncertainty and error, but further research is needed to refine lapse rate estimation methods. In particular, night-time temperature lapse rates in complex terrain remain difficult to determine due to localized atmospheric decoupling, and thermal belts at topographic elevations near the inversion top may lead to multiple lapse rates (Lundquist and Cayan, 2007). Building on the clustering analysis presented here, additional work is needed to understand the relevant spatial scales over which lapse rates should be defined. Development of carefully designed observational temperature networks may help to further evaluate methodological choices. Improvement in lapse rate estimates will enhance the accuracy of environmental models and downscaling routines, enabling better understanding of biophysical processes and how they will change in a warming climate.

References

- Abatzoglou, J. T., Redmond, K. T., & Edwards, L. M. (2009). Classification of Regional Climate Variability in the State of California. *Journal of Applied Meteorology and Climatology*, 48(8), 1527–1541. <https://doi.org/10.1175/2009JAMC2062.1>
- Altman, N., & Krzywinski, M. (2016). Analyzing outliers: Influential or nuisance? *Nature Methods*, 13(4), 281–282. <https://doi.org/10.1038/nmeth.3812>

- Blandford, T. R., Humes, K. S., Harshburger, B. J., Moore, B. C., Walden, V. P., & Hengchun Ye. (2008). Seasonal and Synoptic Variations in Near-Surface Air Temperature Lapse Rates in a Mountainous Basin. *Journal of Applied Meteorology & Climatology*, 47(1), 249–261. <https://doi.org/10.1175/2007JAMC1565.1>
- Cannon, A. J., Neilsen, D., & Taylor, B. (2012). Lapse Rate Adjustments of Gridded Surface Temperature Normals in an Area of Complex Terrain: Atmospheric Reanalysis versus Statistical Up-Sampling. *Atmosphere-Ocean*, 50(1), 9–16. <https://doi.org/10.1080/07055900.2011.649035>
- Cook, R. D. (1977). *Detection of Influential Observation in Linear Regression*. 19(1), 5.
- Daly, C., Gibson, W., Taylor, G., Johnson, G., & Pasteris, P. (2002). A knowledge-based approach to the statistical mapping of climate. *Climate Research*, 22, 99–113. <https://doi.org/10.3354/cr022099>
- Daly, Christopher, Conklin, D. R., & Unsworth, M. H. (2009). Local atmospheric decoupling in complex topography alters climate change impacts. *International Journal of Climatology*, 1857–1864. <https://doi.org/10.1002/joc.2007>
- Daly, Christopher, Halbleib, M., Smith, J. I., Gibson, W. P., Doggett, M. K., Taylor, G. H., Curtis, J., & Pasteris, P. P. (2008). Physiographically sensitive mapping of climatological temperature and precipitation across the conterminous United States. *International Journal of Climatology*, 28(15), 2031–2064. <https://doi.org/10.1002/joc.1688>
- Dobrowski, S. Z., Abatzoglou, J. T., Greenberg, J., & Schladow, S. G. (2009). How much influence does landscape-scale physiography have on air temperature in a mountain environment? *Agricultural and Forest Meteorology*, 149, 1751–1758. <https://doi.org/10.1016/j.agrformet.2009.06.006>
- Dormann, C. F., Elith, J., Bacher, S., Buchmann, C., Carl, G., Carré, G., Marquéz, J. R. G., Gruber, B., Lafourcade, B., Leitão, P. J., Münkemüller, T., McClean, C., Osborne, P. E., Reineking, B., Schröder, B., Skidmore, A. K., Zurell, D., & Lautenbach, S. (2013). Collinearity: A review of methods to deal with it and a simulation study evaluating their performance. *Ecography*, 36(1), 27–46. <https://doi.org/10.1111/j.1600-0587.2012.07348.x>

- Gardner, A. S., & Sharp, M. (2009). Sensitivity of net mass-balance estimates to near-surface temperature lapse rates when employing the degree-day method to estimate glacier melt. *Annals of Glaciology*, *50*(50), 80–86.
<https://doi.org/10.3189/172756409787769663>
- Gardner, A. S., Sharp, M. J., Koerner, R. M., Labine, C., Boon, S., Marshall, S. J., Burgess, D. O., & Lewis, D. (2009). Near-Surface Temperature Lapse Rates over Arctic Glaciers and Their Implications for Temperature Downscaling. *Journal of Climate*, *22*(16), 4281–4298. <https://doi.org/10.1175/2009JCLI2845.1>
- Graham, M. H. (2003). Confronting multicollinearity in ecological multiple regression. *Ecology*, *84*(11), 2809–2815. <https://doi.org/10.1890/02-3114>
- Harding, R. J. (1979). Altitudinal gradients of temperature in the Northern Pennines. *Weather*, *34*(5), 190–202. <https://doi.org/10.1002/j.1477-8696.1979.tb03442.x>
- Immerzeel, W. W., Petersen, L., Raetelli, S., & Pellicciotti, F. (2014). The importance of observed gradients of air temperature and precipitation for modeling runoff from a glacierized watershed in the Nepalese Himalayas. *Water Resources Research*, *50*(3), 2212–2226. <https://doi.org/10.1002/2013WR014506>
- Kattel, D., Yao, T., Yang, K., Tian, L., Yang, G., & Joswiak, D. (2013). Temperature lapse rate in complex mountain terrain on the southern slope of the central Himalayas. *Theoretical & Applied Climatology*, *113*(3/4), 671–682.
<https://doi.org/10.1007/s00704-012-0816-6>
- Kirchner, M., Faus-Kessler Theresa, Jakobi Gert, Leuchner Michael, Ries Ludwig, Scheel Hans-Eckhart, & Suppan Peter. (2013). Altitudinal temperature lapse rates in an Alpine valley: Trends and the influence of season and weather patterns. *International Journal of Climatology*, *33*(3), 539–555. <https://doi.org/10.1002/joc.3444>
- Li, X., Wang, L., Chen, D., Yang, K., Xue, B., & Sun, L. (2013). Near-surface air temperature lapse rates in the mainland China during 1962–2011. *Journal of Geophysical Research: Atmospheres*, *118*(14), 7505–7515.
<https://doi.org/10.1002/jgrd.50553>
- Lookingbill, T. R., & Urban, D. L. (2003). Spatial estimation of air temperature differences for landscape-scale studies in montane environments. *Agricultural and Forest Meteorology*, *114*(3–4), 141–151. [https://doi.org/10.1016/S0168-1923\(02\)00196-X](https://doi.org/10.1016/S0168-1923(02)00196-X)

- Lundquist, J. D., & Cayan, D. R. (2007). Surface temperature patterns in complex terrain: Daily variations and long-term change in the central Sierra Nevada, California. *Journal of Geophysical Research: Atmospheres*, *112*(D11).
<https://doi.org/10.1029/2006JD007561>
- Lundquist, Jessica D., Pepin, N., & Rochford, C. (2008). Automated algorithm for mapping regions of cold-air pooling in complex terrain. *Journal of Geophysical Research: Atmospheres*, *113*(D22). <https://doi.org/10.1029/2008JD009879>
- Mason, C. H., & Perreault, W. D., Jr. (1991). Collinearity, Power, and Interpretation of Multiple Regression Analysis. *Journal of Marketing Research*, *28*(3), 13.
- McCutchan, Morris H. (1983). Comparing temperature and humidity on a mountain slope and in the free air nearby. *Monthly Weather Review*, *111*, 836–845.
[https://doi.org/10.1175/1520-0493\(1983\)111<0836:CTAHOA>2.0.CO;2](https://doi.org/10.1175/1520-0493(1983)111<0836:CTAHOA>2.0.CO;2)
- Menne, M. J., Durre, I., Vose, R. S., Gleason, B. E., & Houston, T. G. (2012). An Overview of the Global Historical Climatology Network-Daily Database. *Journal of Atmospheric and Oceanic Technology*, *29*(7), 897–910.
<https://doi.org/10.1175/JTECH-D-11-00103.1>
- Minder, J. R., Mote, P. W., & Lundquist, J. D. (2010). Surface temperature lapse rates over complex terrain: Lessons from the Cascade Mountains. *Journal of Geophysical Research: Atmospheres*, *115*(D14), D14122. <https://doi.org/10.1029/2009JD013493>
- Montgomery, D. C., Peck, E. A., & Vining, G. G. (2012). *Introduction to Linear Regression Analysis*. John Wiley & Sons, Inc.
- Navarro-Serrano, F., López-Moreno J. I., Azorin-Molina C., Alonso-González E., Tomás-Burguera M., Sanmiguel-Vallelado A., Revuelto J., & Vicente-Serrano S. M. (2018). Estimation of near-surface air temperature lapse rates over continental Spain and its mountain areas. *International Journal of Climatology*, *38*(8), 3233–3249.
<https://doi.org/10.1002/joc.5497>
- Pepin, N., Benham, D., & Taylor, K. (1999). Modeling Lapse Rates in the Maritime Uplands of Northern England: Implications for Climate Change. *Arctic, Antarctic, and Alpine Research*, *31*(2), 151–164. <https://doi.org/10.2307/1552603>
- Pepin, N., Bradley, R. S., Diaz, H. F., Baraer, M., Caceres, E. B., Forsythe, N., Fowler, H., Greenwood, G., Hashmi, M. Z., Liu, X. D., Miller, J. R., Ning, L., Ohmura, A.,

- Palazzi, E., Rangwala, I., Schöner, W., Severskiy, I., Shahgedanova, M., Wang, M. B., ... Yang, D. Q. (2015). Elevation-dependent warming in mountain regions of the world. *Nature Climate Change*, 5(5), 424–430. <https://doi.org/10.1038/nclimate2563>
- Rolland, C. (2003). Spatial and Seasonal Variations of Air Temperature Lapse Rates in Alpine Regions. *Journal of Climate*, 16(7), 1032–1046. [https://doi.org/10.1175/1520-0442\(2003\)016<1032:SASVOA>2.0.CO;2](https://doi.org/10.1175/1520-0442(2003)016<1032:SASVOA>2.0.CO;2)
- Sadoti, G., McAfee, S. A., Roland, C. A., Fleur Nicklen, E., & Sousanes, P. J. (2018). Modelling high-latitude summer temperature patterns using physiographic variables. *International Journal of Climatology*, 38(10), 4033–4042. <https://doi.org/10.1002/joc.5538>
- Sekercioglu, C. H., Schneider, S. H., Fay, J. P., & Loarie, S. R. (2008). Climate Change, Elevational Range Shifts, and Bird Extinctions. *Conservation Biology*, 22(1), 140–150. <https://doi.org/10.1111/j.1523-1739.2007.00852.x>
- Shen, Y.-J., Shen, Y., Goetz, J., & Brenning, A. (2016). Spatial-temporal variation of near-surface temperature lapse rates over the Tianshan Mountains, central Asia. *Journal of Geophysical Research: Atmospheres*, 121(23), 14,006–14,017. <https://doi.org/10.1002/2016JD025711>
- Whiteman, C. D., Zhong, S., Shaw, W. J., Hubbe, J. M., Bian, X., & Mittelstadt, J. (2001). Cold Pools in the Columbia Basin. *Weather and Forecasting*, 16, 16.
- Wolfe, J. A. (1992). *An analysis of present-day terrestrial lapse rates in the western conterminous United States and their significance to paleoaltitudinal estimates* (Report No. 1964; Bulletin). USGS Publications Warehouse. <https://doi.org/10.3133/b1964>

Chapter 3: SnowClim: High-Resolution Snow Model and Data for the Western United States

Abstract

Seasonal snowpack dynamics shape the biophysical and societal characteristics of many global regions. However, snowpack accumulation and duration have generally declined in recent decades largely due to anthropogenic climate change. Mechanistic understanding of snowpack spatiotemporal heterogeneity and climate change impacts will benefit from snow data products that are based on physical principles, that are simulated at high spatial resolution, and that cover large geographic domains. Existing datasets do not meet these requirements, hindering our ability to understand both contemporary and changing snow regimes and to develop adaptation strategies in regions where snowpack patterns and processes are important components of Earth systems.

We developed a computationally efficient physics-based snow model, SnowClim, that can be run in the cloud. The model was evaluated and calibrated at NRCS Snowpack Telemetry sites across the western United States (U.S.), achieving a site-median root mean square error for daily snow water equivalent of 62 mm, bias in peak snow water equivalent of -9.6 mm, and bias in snow duration of 1.2 days when run hourly. Positive biases were found at sites with mean winter temperature above freezing where the estimation of precipitation phase is prone to errors. The model was applied to the western US using newly developed forcing data created by statistically downscaling 4-hourly pre-industrial, historical, and pseudo-global warming climate data from the Weather Research and Forecasting (WRF) model. The resulting product is the SnowClim dataset, a suite of summary climate and snow metrics for the western US at 210 m spatial resolution. The physical basis, large extent, and high spatial resolution of this dataset will enable unprecedented analyses of changing hydroclimate and its implications for natural and human systems.

Introduction

Seasonal snowpack shapes the climatic, hydrologic, ecological, economic, and cultural characteristics of many global regions. Snow is an important determinant of the surface energy balance through its effect on land surface albedo, partitioning of sensible and

latent heat fluxes, near-surface atmospheric stability, and horizontal energy transport (Cohen, 1994; Rudisill et al., 2021; Stiegler et al., 2016). Hydrologic benefits of snow include natural water storage, delayed runoff, and cooler stream temperatures (Bales et al., 2006; Luce et al., 2014). Ecologically, seasonal snow insulates flora and snow-dependent fauna, controls mobility and foraging opportunities, mediates nutrient cycling, and supplements plant-water availability (Formozov, 1964; Grippa et al., 2005; Jones, 1999). Economically, seasonal snow synchronizes water supply and demand enabling crop irrigation, fuels a multibillion-dollar winter recreation industry in the United States (U.S.) alone, and can cause transportation delays and accidents (Burakowski & Magnusson, 2012; Qin et al., 2020; Seeherman & Liu, 2015; Sturm et al., 2017). Finally, seasonal snow is a defining aspect of many cultures globally, shaping language, traditions, and sense of self (Eira et al., 2013; Mergen, 1997).

In many mountain regions, recent decades have seen less precipitation falling as snow, lower peak snow water equivalent (SWE), shorter snow duration, and earlier snowmelt runoff (Choi et al., 2010; Fritze et al., 2011; Knowles et al., 2006; Mote et al., 2018). These developments are expected to continue in the coming decades, resulting in substantial declines (>50%) in seasonal snowpack for areas such as the western U.S. and significant impacts to human and natural systems (Fountain et al., 2012; Fyfe et al., 2017; Huss et al., 2017; Marshall et al., 2019). In addition to these macroscale developments, there are important nuances to changing snow. Increased atmospheric water vapor due to warming is expected to enable larger snowfall events (Lute et al., 2015), which may buffer declines in snowpack (Marshall et al., 2020). Changes in atmospheric circulation may affect snow accumulation, for example by diminishing orographic precipitation enhancement (Luce et al., 2013) or altering characteristics of atmospheric rivers (Dettinger, 2011). Decreasing snow cover will result in increased hydrologic importance of microclimates that serve as snow refugia, such as high elevations, deposition zones, and shaded areas (Marshall et al., 2019; McLaughlin et al., 2017). A warmer and moister atmosphere will shift the relative importance of snowpack energy and mass budget terms, resulting, for example, in slower snowmelt (Musselman et al., 2017), changes to the partitioning of snow ablation between runoff and sublimation (Sexstone et al., 2018), and increasing rain-on-snow risk in regions that retain snow cover (Musselman et al., 2018).

Understanding these changes and their implications often requires snow models and modeled snow data products (hereafter snow data) that satisfy at least one of several criteria. These criteria include that the data is: a) simulated with physics-based representations of energy and mass transfer processes, b) spatially continuous, c) high spatial resolution, d) large extent, e) multivariate, and f) multitemporal. To address some questions about contemporary or future snow, the snow models themselves are needed and must be able to synthesize data that satisfies these criteria. Snow data developed from physical principles is argued to be necessary for both capturing the spatial variability of energy fluxes across the landscape and providing physically realistic simulations of the effects of climate change (Kumar et al., 2013; Raleigh & Clark, 2014). To assess changes in snowpack across a landscape, spatially continuous data are needed. In areas of complex terrain, high spatial resolution data are necessary to resolve the effects of elevation and shading (Barsugli et al., 2020; Sohrabi et al., 2019; Winstral et al., 2014). For some applications, such as water management and species distribution modeling, snow data may need to cover large geographic domains. Multiple snow metrics are needed for diverse applications (e.g., SWE for water management, snow depth for wildlife). Finally, historical and future data are necessary to evaluate changes over time and to inform long term planning and development of adaptation strategies for specific locales.

There are two major hurdles to the development of a snow dataset that meets all of these criteria: appropriate forcing data and computational cost. Presently, large-extent climate datasets only achieve horizontal resolutions of up to 1 km (e.g., Abatzoglou & Brown, 2012; Fick & Hijmans, 2017; Thornton et al., 2014) and the finer resolution datasets cover limited domains or are restricted to historical periods (Dietrich et al., 2019; Holden et al., 2011, 2016). Second, even with appropriate forcing data, the computational expense of running snow models has generally forced the selection of some of these criteria at the expense of others (Winstral et al., 2014). For example, a temperature-index model might be used for applications requiring rapid results over large domains (e.g., SNOW-17; Anderson, 2006), a physics-based model might be run at high resolution over watershed sized domains (Garen & Marks, 2005; Liston & Elder, 2006), or a physics-based model might be run at coarser resolution over a larger extent (e.g., SNODAS, National Operational Hydrologic Remote Sensing Center, 2004; WRF, Liu et al., 2017; Gergel et al., 2017; Wrzesien et al., 2018).

There is potential for clever computational solutions and model formulations, such as variable resolution grids, to alleviate these trade-offs to some extent (Marsh et al., 2020).

In this study we developed a computationally efficient physics-based snow model called SnowClim that has a flexible model structure and can be run in the cloud. The model retains the most important components of physically based models, including the complete energy balance and internal snowpack energetics, while omitting more computationally expensive components such as horizontal transport, multiple layers, and iterative solutions for snow surface temperature. Unlike existing models, this simplified physics-based model is efficient enough to be run over sub-continental domains at high spatial resolution. We force the SnowClim model with pre-industrial (1850-1879), historical (2000-2013), and projected future (2071-2100) meteorological data from the Weather Research and Forecasting (WRF) model downscaled to correct for terrain effects. We then applied the model to the western U.S. to create the SnowClim dataset, a multivariate, gridded, snow and climate dataset for three time periods at 210m spatial resolution. Here we provide a description of the model and its application to the western U.S., including parameterization, calibration, climate forcing data preparation, and resultant datasets.

Model Description

Model Overview

The SnowClim model is a fully distributed energy and mass balance snow model. It simulates the snowpack as a single layer, but accounts for different surface and pack temperatures (Figure 3.1). The effects of vegetation, fractional snow cover, and snow redistribution via gravitational and wind-driven processes are not represented.

The model has a flexible structure to facilitate uncertainty analysis and application to new conditions. This flexible structure includes tunable parameters, customizability of the spatiotemporal application, and process modularity. Key parameters (Table 3.2) are user-defined as opposed to hard-coded in the model, allowing for calibration of the model to new conditions and regions as seen fit. The temporal and spatial resolution and extent are also user-defined, which allows users to adjust to computational constraints and the requirements of the project. Finally, key processes such as albedo and turbulent fluxes are modularized to allow evaluation of alternative process representations.

The required forcings are described in Table 3.1. The model is written in MATLAB. The model can be run in the cloud using MATLAB online through CUAHSI's HydroShare Platform.

Table 3.1 Required forcing data for the snow model.

Forcing data	Abbreviation
Downward shortwave radiation flux at the surface	SW_{\downarrow}
Downward longwave radiation flux at the surface	LW_{\downarrow}
Air Temperature	T_a
Dewpoint Temperature	T_d
Precipitation	P
Relative Humidity	RH
Specific Humidity	Q_a
Wind speed	U_a
Air pressure	P_{air}

Energy Balance

The SnowClim model evaluates the surface energy balance at each time step such that

$$Q_{net} = SW_{\downarrow} - SW_{\uparrow} + LW_{\downarrow} - LW_{\uparrow} + H + E_i + E_w + P + G$$

Equation 3.1

where Q_{net} is the net surface energy flux, SW_{\downarrow} is the downward shortwave radiation at the surface, SW_{\uparrow} is the upward shortwave radiation at the surface, LW_{\downarrow} is the downward longwave radiation at the surface, LW_{\uparrow} is the upward longwave radiation at the surface, H is the sensible heat flux, E_i and E_w are the latent heat fluxes of ice and water, P is the advected heat flux from precipitation, and G is the ground heat flux (Figure 3.1).

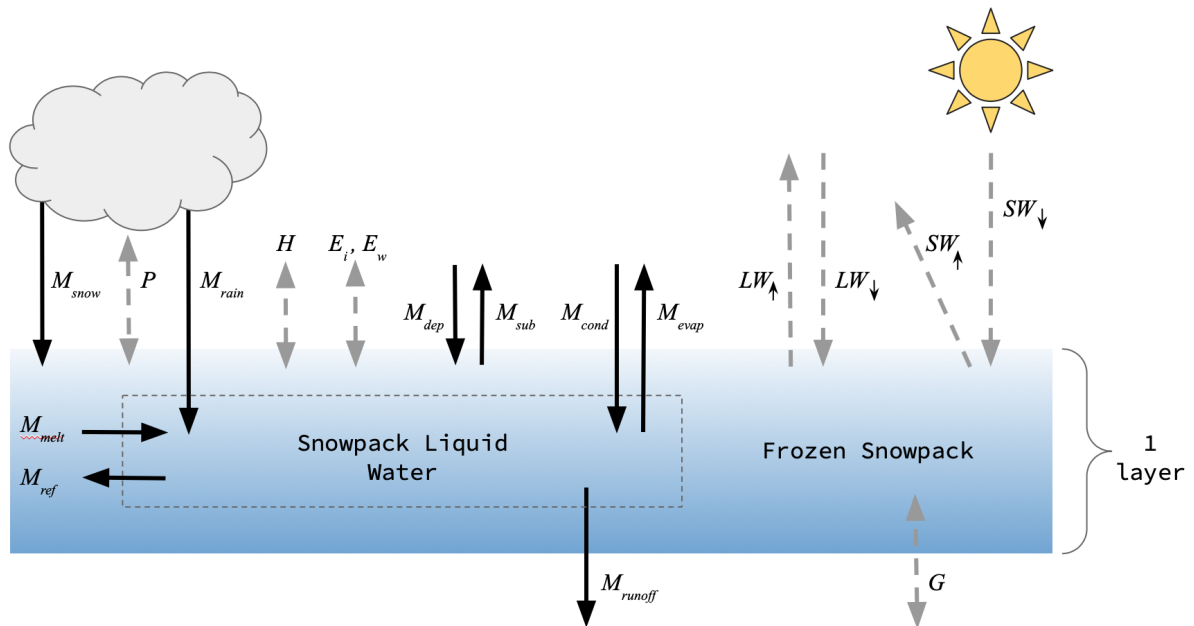


Figure 3.1 Snow model conceptual diagram. Solid black arrows indicate mass fluxes, dashed grey arrows indicate energy fluxes. Fluxes are described in the text.

Shortwave Radiation

Upward shortwave radiation is equivalent to

$$SW_{\uparrow} = SW_{\downarrow} \alpha$$

Equation 3.2

where α is the spectrally integrated snow surface albedo.

Springtime snow model simulations are sensitive to the specific albedo algorithm (Etchevers et al., 2004; Günther et al., 2019). The SnowClim model provides three options for computing snow albedo (albedo_opt). In all options, albedo decays with time and the albedo of shallow snowpacks (<100 mm depth) is diminished to account for the albedo of the ground surface, assumed to be 0.25 (Walter et al., 2005). A user-specified maximum albedo parameter (albedo_max) is used in each method.

The simplest albedo model (Essery et al., 2013; hereafter Essery), is empirical and sets albedo decay as a function of snowpack temperature. Snow albedo is augmented based on the occurrence and amount of new snow. Parameters other than the maximum albedo are taken from Douville et al., (1995).

In the second albedo model (Hamman et al., 2018; Liang et al., 1994; hereafter VIC), snowpacks with new snow depth $> 10\text{mm}$ and non-zero cold content receive the maximum snow albedo. Other albedo parameters are taken directly from VIC. Snow albedo decays more rapidly for melting snowpacks than cold snowpacks (cold content, $cc < 0$).

The final albedo model (Tarboton & Luce, 1996; hereafter Tarboton) accounts for the wavelength dependence of albedo by computing separate visible and near-infrared band albedos as a function of snow surface age and solar illumination angle. The maximum albedo parameter is set equal to the average of the maximum visible band and infrared band albedos. This is the only albedo model of the three that includes a correction for illumination angle.

Longwave Radiation

Upward longwave radiation is a function of snow surface temperature (T_s) in degrees Celsius, snow emissivity (ε), and the Stefan-Boltzmann constant (σ) such that

$$LW_{\uparrow} = \varepsilon\sigma(T_s + 273.15)^4$$

Equation 3.3

We assume $\varepsilon = 0.98$ (Armstrong & Brun, 2008). We consider T_s to be a function of the dewpoint temperature (T_d ; Raleigh et al., 2013), such that

$$T_s = \min(0^\circ\text{C}, T_d + T_{add})$$

Equation 3.4

where T_{add} is an augmentation parameter that increases T_s and improves simulations of sublimation. For further discussion of T_s see the section title Enhanced Single Layer Approach.

Turbulent Fluxes

The turbulent fluxes, H , E_i , and E_w , are estimated using a Richardson number parameterization of the exchange coefficient following Essery et al., (2013). The bulk formula are

$$H = -\rho_a c_a C_H U_a (T_s - T_a)$$

Equation 3.5

$$E_i = -\rho_a C_H U_a (Q_s - Q_a) \lambda_s \quad \text{for } T_s < 0$$

Equation 3.6

$$E_w = -\rho_a C_H U_a (Q_s - Q_a) \lambda_v \quad \text{for } T_s = 0$$

Equation 3.7

where ρ_a is the air density, c_a is the specific heat capacity of air, C_H is the bulk exchange coefficient that accounts for near-surface atmospheric stability, U_a is the wind speed, Q_s is the specific humidity of the snow surface, and Q_a is the specific humidity of the air which is a required forcing. The specific humidity of the snow surface is calculated from T_s . The exchange coefficient C_H is parameterized as a function of the near-surface atmospheric stability as captured by the bulk Richardson number (Ri_B) such that

$$C_H = F_H(Ri_B) C_{HN}$$

Equation 3.8

$$Ri_B = (gz_u(T_a - T_s))/(T_a U_a^2)$$

Equation 3.9

$$C_{HN} = k^2 [\ln(z_u/z_0)]^{-1} [\ln(z_T/z_h)]^{-1}$$

Equation 3.10

$$F_H(Ri_B) = 1 \quad \text{for } Ri_B = 0$$

Equation 3.11

$$F_H(Ri_B) = 1 - (3c Ri_B)/(1 + 3c^2 C_{HN} (-Ri_B z_u/z_0)^{1/2}) \quad \text{for } Ri_B < 0$$

Equation 3.12

$$F_H(Ri_B) = [1 + (2c Ri_B)/(1 + Ri_B)^{1/2}]^{-1} \quad \text{for } Ri_B > 0$$

Equation 3.13

where g is gravitational acceleration, z_u is the height of simulated wind speeds, z_T is the height of simulated air temperatures, z_0 is the surface roughness length for momentum, z_h is the surface roughness length for heat and water vapor, and c is a constant assumed to equal 5 (Louis, 1979). z_0 and z_h are adjustable user-specified parameters (Table 3.2).

An optional windless exchange coefficient is available to counter large radiative losses particularly during stable conditions (Helgason & Pomeroy, 2012; Jordan, 1991). Application of the windless exchange coefficient can be modified through three parameters: $E0_value$, $E0_app$, and $E0_stability$ (Table 3.2). $E0_value$ is the value in $W m^{-2}$ of the windless exchange coefficient. $E0_app$ controls the application of the windless heat exchange

coefficient to the sensible and latent heat fluxes; an $E0_app$ value of 1 applies the coefficient only to the sensible heat flux, whereas an $E0_app$ value of 2 applies the coefficient to both the sensible and latent heat fluxes. $E0_stability$ controls the type of conditions where the windless coefficient is applied; an $E0_stability$ value of 1 applies the coefficient to all conditions, whereas an $E0_stability$ value of 2 applies the condition only under stable atmospheric conditions.

Precipitation Heat Flux

The heat flux of liquid precipitation is

$$P = c_w \rho_w T_d P_{rain}$$

Equation 3.14

where c_w is the specific heat of water, ρ_w is the density of water, and P_{rain} is the rate of liquid precipitation. The heat flux of solid precipitation (S) is handled separately for diagnostic purposes and is added directly to the snowpack cold content.

$$S = c_i \rho_w T_d P_{snow}$$

Equation 3.15

where c_i is the heat capacity of ice and P_{snow} is the rate of snowfall.

Ground Heat Flux

The ground heat flux can be important in controlling the onset of seasonal snow accumulation, particularly in warmer environments (e.g., Mazurkiewicz et al., 2008). However, under most circumstances G is thought to provide a minor contribution to the energy budget (DeWalle & Rango, 2008). In the interest of model efficiency and to avoid uncertainties associated with estimating soil temperatures and thermal conductivities, we use a constant G of 2 W m^{-2} (Walter et al., 2005), similar to other models (Etchevers et al., 2002).

Enhanced Single Layer Approach

Single layer snow models typically provide less physically realistic snowpack simulations than multilayer models due to their simplified treatment of energy transfer within the snowpack (Blöschl & Kirnbauer, 1991; Waliser et al., 2011). Bulk single layer conceptualizations treat the surface temperature and energy balance as synonymous with the

pack temperature and energy balance, ignoring the contrast between the thin surface layer which is highly sensitive to the near-surface atmosphere, and the pack, which is characterized by thermal inertia, i.e., cold content. These distinctions are key to accurate modeling of snowpack heat fluxes (Blöschl & Kirnbauer, 1991) and snowpack ablation (Waliser et al., 2011).

To address these shortcomings, advanced single layer snow models have differentiated between surface and pack temperatures, while attempting to maintain the parsimony of a single layer model (Tarboton & Luce, 1996; You et al., 2014). However, these approaches typically require iterative methods to solve for snow surface temperature that can be computationally expensive (Wigmosta et al., 1994) and subject to large uncertainty (Raleigh et al., 2013).

The present model uses a two-step modification of the net surface energy flux to approximate the conduction of energy between the surface and the snowpack. This approach enables separate temperatures and energy balances for surface and pack components while retaining the computational efficiency necessary to accomplish the modeling objectives of both large spatial extent and relatively fine resolution. In this approach, the surface is conceptualized as a skin with zero depth.

First, we apply a temporal running mean to the net surface energy flux to approximate the attenuation with depth of the characteristic diurnal variations in energy at the surface, akin to the approach taken by You et al., (2014). The smoothed energy flux from the surface to the pack at each time step ($\overline{Q_{net}}$) is calculated as the average net surface energy flux over a period *smooth_hrs*, that is a tunable parameter (Table 3.2). This approach reduces unrealistic high frequency modifications of the cold content and large amplitude freeze-thaw cycles during the ablation season.

Second, we apply a progressive tax on the negative net energy flux to the snowpack to limit the excessive accumulation of cold content that results from all surface energy being directly translated to the pack. The net effect of the energy tax is to reduce snowpack cold content, resulting in more accurate cold content simulations similar to those from other, more complex physics-based models (Jennings et al., 2018; not shown). Other single layer models have sought to limit cold content, however they used approaches that required site specific

calibration (Blöschl & Kirnbauer, 1991; Braun, 1984). We apply a progressive tax such that negative energy fluxes to snowpacks with larger cold content receive larger taxes:

$$Q_{pack} = \overline{Q_{net}} \quad \text{for } \overline{Q_{net}} \geq 0$$

Equation 3.16

$$Q_{pack} = \overline{Q_{net}} \times (1 - tax) \quad \text{for } \overline{Q_{net}} < 0$$

Equation 3.17

$$tax = \frac{cc - cc_0}{cc_1} \times maxtax \quad \text{such that } 0 \leq tax \leq maxtax$$

Equation 3.18

$\overline{Q_{net}}$ is the smoothed net surface energy flux, Q_{pack} is the energy flux from the surface to the pack, and cc is the snowpack cold content. cc_0 , cc_1 , and $maxtax$ are tunable parameters that define the maximum (least negative) cold content to which the tax should be applied, the range of cold content over which the tax should be applied (cc_0 to $cc_0 + cc_1$), and the maximum possible tax, respectively (Table 3.2). Negative energy fluxes to snowpacks with cold contents less negative than cc_0 receive 0 tax, and negative energy fluxes to snowpacks with cold contents more negative than $cc_0 + cc_1$ receive a tax equal to $maxtax$.

Q_{pack} is added to the snowpack cold content (cc) at each time step. Pack temperature (T_{pack}) can be obtained from cold content:

$$T_{pack} = cc / (\rho_w \times ci \times SWE)$$

Equation 3.19

where ci is the heat capacity of ice and SWE is the snow water equivalent.

Modification for Shallow Snowpacks

We developed a computationally efficient approach for controlling energy balance instabilities for shallow snowpacks. Marks et al., (1999) addressed the problem by shifting to progressively smaller time steps. In the interest of computational efficiency, we take an alternative approach. When modeled SWE is less than a threshold value, T_{pack} is constrained to be $\geq T_a$ but $\leq 0^\circ C$. Cold content is then updated according to this new temperature. The threshold for applying this correction is 15 mm of SWE for every hour in the time step (e.g.,

for a model run at a 4 hour time step the temperature correction would be applied to snowpacks with 60 mm SWE or less). Constraining T_{pack} and cold content in this way is reasonable given that surface and pack temperatures are likely to be similar for shallow snowpacks and the strong correspondence between T_s and T_a (Helgason & Pomeroy, 2012).

Mass Balance

The mass balance of the solid and liquid portions of the snowpack are evaluated at each time step as

$$M_s = M_{snow} + M_{ref} - M_{melt} + M_{dep} - M_{sub}$$

Equation 3.20

$$M_l = M_{rain} - M_{ref} + M_{melt} - M_{runoff} + M_{cond} - M_{evap}$$

Equation 3.21

where M_s is the mass of the solid portion of the snowpack, M_{snow} is the mass of new snowfall, M_{ref} is the mass of liquid water in the snowpack that has been refrozen, M_{melt} is the mass of snow that has melted, M_{dep} is the mass of deposition, M_{sub} is the mass of sublimation, M_l is the mass of the liquid in the snowpack, M_{rain} is the mass of rain added to the snowpack, M_{runoff} is the mass of liquid water that has left the snowpack as runoff, M_{cond} is the mass of condensation, and M_{evap} is the mass of evaporation (Figure 3.1).

Accumulation

Snowfall is calculated as an air temperature and relative humidity dependent fraction of precipitation using the bivariate logistic regression model of Jennings et al., (2018). We use a non-binary formulation to allow for mixed phase precipitation. New snowfall amounts less than 0.1 mm water equivalent per hour are set to 0. Rainfall is the difference between precipitation and snowfall. The temperature of new snowfall is set equal to the minimum of the dewpoint temperature and freezing point (0°C) whereas the temperature of rainfall is set equal to the maximum of the dewpoint temperature and the freezing point (Marks et al., 2013; Raleigh et al., 2013).

The density of new snowfall is calculated as a function of air temperature (Anderson, 1976) using constants identified by Oleson et al., (2004). Compaction of the snowpack is

modeled as a function of SWE and snowpack temperature following (Anderson, (1976) and using constants from Boone, (2002) for the ISBA-ES snow model. Snow depth is a function of SWE and density and is updated following changes in either variable.

Melt

Positive net energy flux must satisfy the snowpack cold content before melt can occur. Melt is equivalent to the minimum of the current SWE and the potential melt,

$$melt_{pot} = Q_{pack}/(\lambda_f \times \rho_w) \text{ for } Q_{pack} > 0$$

Equation 3.22

where λ_f is the latent heat of freezing.

Liquid Water Content

Rainfall, melt, and condensation are added to and evaporation is subtracted from the snowpack liquid water content. Snowpack liquid water content in excess of the liquid water holding capacity of the snowpack contributes to runoff. The liquid water holding capacity of the snowpack is the product of snow depth and the maximum liquid water fraction (lw_max , Table 3.2). Liquid water content below this threshold but greater than the minimum liquid water content (equivalent to 1% of snow depth; Marsh, (1991)) is allowed to drain at a rate of 100 mm hr^{-1} (based on values in Armstrong & Brun, (2008) and DeWalle & Rango, (2008)).

Refreezing

Excess cold content can be used to refreeze liquid water in the snowpack. The amount of water refrozen is the minimum of the total liquid water content of the snowpack and the potential refreezing,

$$refreeze_{pot} = -\frac{cc}{\lambda_f \times \rho_w} \text{ for } cc < 0$$

Equation 3.23

$$M_{ref} = \min(refreeze_{pot}, M_l) \text{ for } cc < 0$$

Equation 3.24

Energy released by refreezing is added to the snowpack cold content and the refrozen mass is added to the SWE, increasing the snowpack density (we assume no change in snow depth).

Refreezing is turned off when snowpack density exceeds 550 kg m^{-3} , which is considered to be the maximum snow density above which snow becomes firm (Marshall, 2012).

Sublimation and Condensation

Latent heat transfer results in sublimation or evaporation from or deposition or condensation onto the snowpack, such that

$$M_{sub} = -E_i / (\lambda_s \times \rho_w) \quad \text{for } E_i < 0 \text{ and } T_s < 0$$

Equation 3.25

$$M_{evap} = -E_w / (\lambda_v \times \rho_w) \quad \text{for } E_w < 0 \text{ and } T_s = 0$$

Equation 3.26

$$M_{dep} = -E_i / (\lambda_s \times \rho_w) \quad \text{for } E_i > 0 \text{ and } T_s < 0$$

Equation 3.27

$$M_{cond} = -E_w / (\lambda_v \times \rho_w) \quad \text{for } E_w > 0 \text{ and } T_s = 0$$

Equation 3.28

where λ_s is the latent heat of sublimation and λ_v is the latent heat of vaporization.

Model Application to the Western United States

The SnowClim model was evaluated and calibrated at a collection of automated snow stations across montane portions of the western US and further applied to the broader western US to create the SnowClim dataset. We describe the preparation and downscaling of the meteorological forcing data, the model calibration, and the model simulations for the western US. The model was calibrated at Snowpack Telemetry (SNOTEL) sites and model performance at these sites was used to select the parameters and temporal resolution at which to run the model over the full domain.

Table 3.2 Parameters, their abbreviated names, the parameter values used in calibration, and their units. Parameter values with an * indicate values chosen for the full model run by calibration at SNOTEL sites. Additional parameter options, including the VIC model albedo option, were evaluated in preliminary work but were excluded from the full calibration due to consistently poor performance. ¹Essery et al., (2013); ²Tarboton & Luce, (1996)

Parameter	Abbreviated name	Values used for calibration	Units
Albedo Algorithm	<i>albedo_opt</i>	Essery ⁽¹⁾ , Tarboton ⁽²⁾ *	-
Momentum roughness length	z_0	10^{-3} , 10^{-4} , 10^{-5} *	m
Heat and vapor roughness length	z_h	$z_0/10$ *	m
Maximum Albedo	<i>albedo_max</i>	0.85*, 0.90	-
Maximum liquid water fraction	<i>lw_max</i>	0.1*	-
Windless heat exchange coefficient	<i>E0</i>	0, 1*, 2	W m ⁻² K ⁻¹
Windless heat exchange coefficient flux application	<i>E0_app</i>	1*	-
Windless heat exchange coefficient stability condition	<i>E0_stability</i>	2*	-
Cold content threshold at which to start energy tax	cc_0	0*, -5000, -10000	kJ m ⁻²
Cold content range to tax	cc_1	-5000, -10000*, -15000, -20000	kJ m ⁻²
Maximum tax to apply to surface energy	<i>maxtax</i>	0.3, 0.6, 0.9*	-
Surface energy flux smoothing window	<i>smooth_hrs</i>	8, 12*, 24	hours
Snow surface temperature augmentation	T_{add}	0, 1, 2*	°C

Spatial Resolution

To balance the competing ambitions of high spatial resolution and computational feasibility over the western US domain, we used variable spatial resolutions. Regions of complex terrain were modeled at 210m (hereafter ‘fine’). This high resolution enhances the model’s ability to capture the effects of elevation, aspect, and slope on snowpack in complex terrain. Regions of less complex terrain were modeled at 1050m (hereafter ‘coarse’). Terrain complexity was assessed for each coarse grid cell by examining the elevations and downscaled solar radiation values for the 25 collocated fine grid cells. If the elevation difference across the fine cells was less than 50m and the maximum percent difference in solar radiation was less than 10%, then snow simulations were completed at coarse resolution. Otherwise, simulations were completed at fine resolution. This resulted in approximately 30% of the domain being modeled at coarse resolution (Figure B.1). Grid cells were defined using the 1 arc-second National Elevation Dataset Digital Elevation Model (DEM; Gesch et al., 2018), aggregated to 210m or 1050m.

Forcing Data Preparation

Modeled hourly meteorological data from the Weather Research and Forecasting model (WRF; Liu et al., 2017) were downscaled to force the snow model (Table 3.3). Forcing data was developed for a historical period, future period, and pre-industrial period. The raw WRF data consisted of 4 km spatial resolution hourly simulations for 1 October 2000 to 30 September 2013, that used initial and boundary conditions from ERA-Interim (Dee et al., 2011), herein referred to as historical period. A pseudo-global warming run was also performed by perturbing ERA-Interim by average differences from a suite of climate models participating in the Fifth Coupled Model Intercomparison Project (CMIP5; Taylor et al., 2012) between 1976-2005 and 2071-2100 under the RCP 8.5 scenario (Liu et al., 2017). Pre-industrial forcing data was developed by perturbing the downscaled historical WRF data by monthly climatological differences in climate between pre-industrial (1850-1879) and the historical period using a pattern scaling approach (Mitchell, 2003) based on spatially varying differences in variables from the CMIP5 models.

Table 3.3 WRF data used to derive forcing data for the snow model.

WRF data	Abbreviation
Downward shortwave radiation flux at the surface	SW_{\downarrow}
Downward longwave radiation flux at the surface	LW_{\downarrow}
Mean Air Temperature	T_a
Precipitation	P
Wind speed	U_a
Air pressure	P_{air}
Water vapor mixing ratio (kg/kg)	Q

Spatial downscaling for all variables except solar radiation was accomplished using moving window lapse rates (i.e., the change in the variable with elevation). Lapse rate downscaling has been shown to perform well relative to other statistical downscaling approaches in mountainous terrain (Praskievicz, 2018; Wang et al., 2012). We estimated monthly lapse rates for each grid cell and each variable, except for temperature for which we estimated hourly lapse rates for each grid cell. Windows of 7x7 WRF grid cells, or 28 km x 28 km, were used to balance the competing objectives of sufficient data points and the ability to capture local phenomena (Lute & Abatzoglou, 2021). Lapse rate corrections were applied hourly using the elevation difference between the WRF grid cell and the target DEM grid cell. For air pressure, lapse rates were calculated from and applied to temporally averaged WRF data. Grid cells not classified as land by WRF were excluded from lapse rate calculations.

For precipitation, a modified version of the methods above was used. Prior to calculating lapse rates, WRF precipitation was bias-corrected to monthly 4 km precipitation from PRISM (PRISM Climate Group, 2015) by calculating monthly correction ratios- the ratio of total monthly PRISM precipitation to total monthly WRF precipitation. Correction ratios were set to 1 (no correction) when monthly WRF precipitation was 0 or when the ratio was infinite. Monthly precipitation lapse rates were divided by the number of hours with

precipitation each month and days with 0 precipitation were maintained in the downscaled data to avoid precipitation everyday due to non-zero monthly lapse rates.

Solar radiation was downscaled to the target DEM using the insol package in R (Corripio, 2015) following the approach of Lute & Abatzoglou, (2021) which preserves the atmospheric effects (e.g., cloud cover) captured by WRF and also accounts for slope, aspect, self-shading, and shading by adjacent terrain. Parameters required by the algorithm, including visibility, RH, and temperature, were assumed to be constant. Terrain corrections were calculated for the midpoint of each hour of the middle day of each month, aggregated to the desired temporal resolution using a weighting scheme based on the amount of solar radiation each hour, and then interpolated to the full time period.

For model calibration at SNOTEL sites (see next section), the above downscaling procedures were applied, but values were adjusted based on the elevation difference between the SNOTEL site and the collocated WRF grid cell based on calculated lapse rates. Downscaled WRF precipitation was bias corrected to SNOTEL sites by applying a monthly correction factor consisting of the ratio of the total SNOTEL precipitation to the total WRF precipitation similar to Havens et al., (2019). We note that such bias correction approaches may not address issues of precipitation undercatch at SNOTEL sites.

Additional variables needed to force the snow model including specific humidity, relative humidity, and dewpoint temperature were derived from the downscaled water vapor mixing ratio, air temperature, and air pressure data using standard methods. Dewpoint temperatures exceeding the air temperature were set equal to the air temperature.

Model Calibration

Calibration Methods

The model was calibrated at SNOTEL sites across the mountains of the western US to select a single best parameter set across all sites. A total of 170 SNOTEL sites were selected meeting the following requirements:

1. elevation difference of less than 75m relative to the collocated WRF grid cell;
2. missing no more than 1% of daily precipitation and SWE observations between October and May in every water year between 1 October 2000 and 30 September 2013;

3. located more than 25km from any other SNOTEL site.

Missing SWE values were infilled using linear interpolation. Missing precipitation values were infilled using an inverse distance weighted average of the values at the three closest sites.

Calibration consisted of running the model across all SNOTEL sites for each possible combination of parameters listed in Table 3.2. Model performance was assessed using the mean absolute percent error (MAPE) of annual maximum SWE (maxswe), the MAPE of annual snow duration, and the root mean squared error (RMSE) of daily SWE at each site. Snow duration was defined as the duration (in days) of the longest period of consecutive days with $SWE > 0$. RMSE was computed for days when observed SWE exceeded 10 mm. Additionally, we used the mean error (ME) and mean percent error (MPE) of maxswe and duration to visualize calibration errors. The optimal parameter set was selected using Pareto preference ordering (Khu & Madsen, 2005) based on the median of each statistic across stations.

The model was subsequently evaluated for different run time steps (1, 2, 3, 4, 6, 8, 12, and 24 hours). Separate model calibration for each time step selected similar parameter sets to the hourly run, so the hourly parameter set was used for all time steps. Model performance was again assessed as described above.

Calibration Results

Snow model calibration via Pareto optimization selected a single best parameter set (Table 3.2). The station median MAPE of maxswe, MAPE of snow duration, and daily RMSE for this parameter set were 15.6%, 8.86%, and 62.2 mm, respectively. The spatial distribution of ME and MPE in maxswe and duration lacked strong coherent spatial patterns, suggesting that the model captured major climate related effects (Figure 3.2). The largest negative biases were found at dry sites with small or intermittent snowpacks (Figure B.2). The largest positive biases were found at sites with mean winter temperatures at or above freezing, where snow accumulation is very sensitive to the partitioning of precipitation into rain vs. snow (Figure B.2). A time series of observed and modeled SWE at one site with error values close to the station median values illustrates the model performance on a daily scale (Figure 3.3). The model also captured key components of interannual snowpack variability

over the short historical period; the station median correlations for maxswe and for snow duration were 0.92 and 0.69, respectively. The station correlations did not demonstrate any clear geographic or climatic patterns. This lends confidence to the model's ability to transfer to new climates. The parameter sensitivity of the model is documented in Appendix B (Figure B.3).

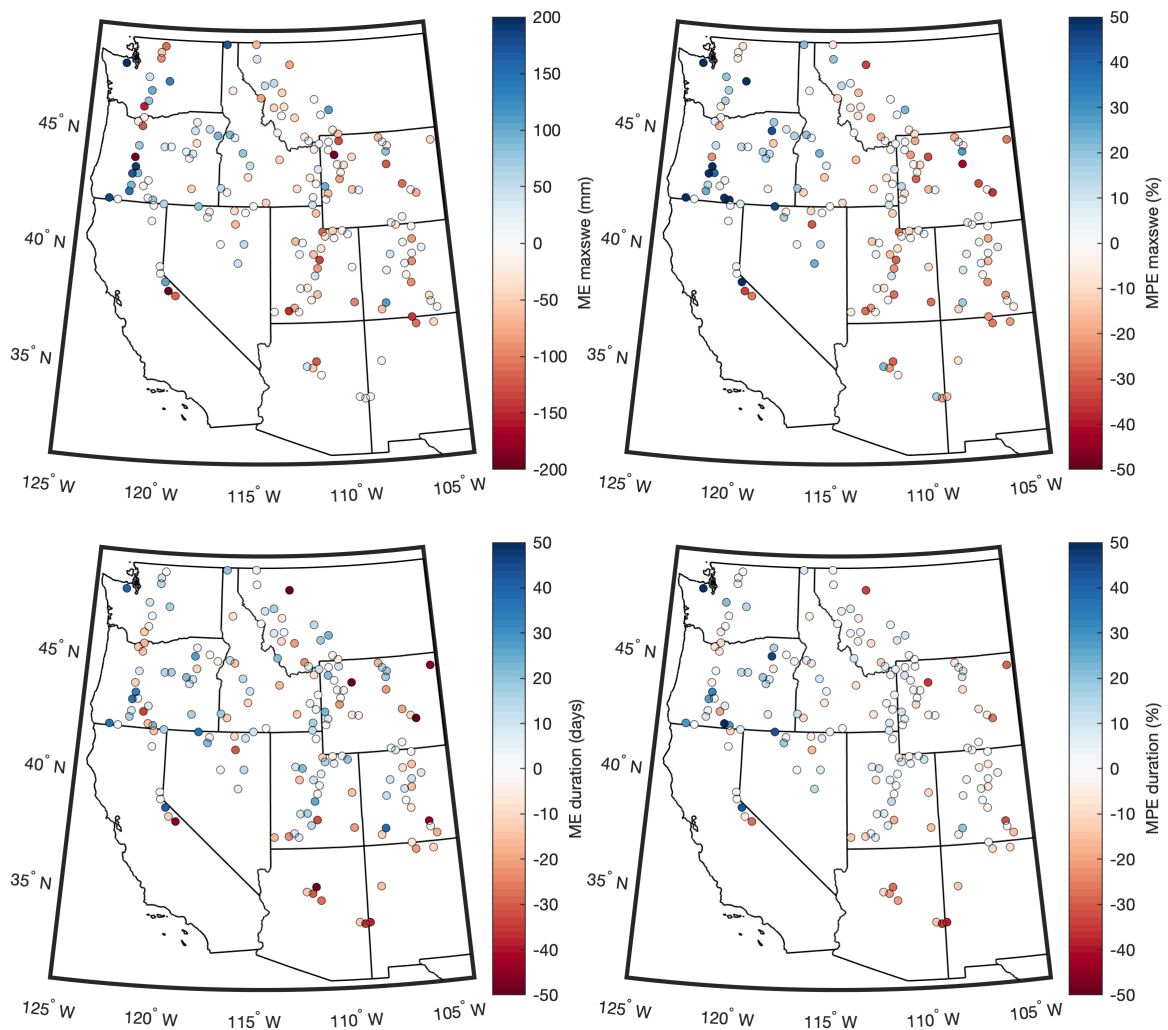


Figure 3.2 Performance metrics for an hourly model run with the selected parameterization.

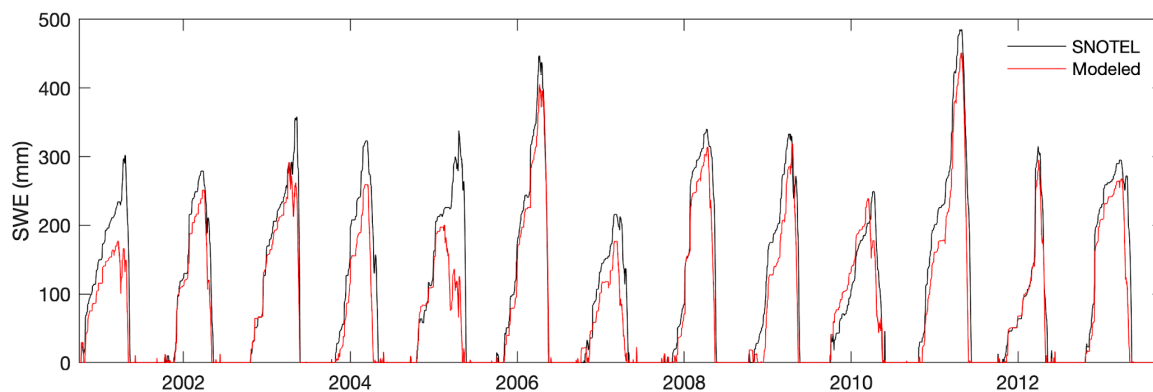


Figure 3.3 Time series of observed and modeled SWE at the Hilt Creek, Idaho SNOTEL site. Out of all 170 SNOTEL sites, errors at this site were closest to the all-station median errors reported in the text.

Model performance generally deteriorated as temporal resolution coarsened from 1 hour to 24 hours, although there was some improvement going from 12 hours to 24 hours (Figure 3.4). A timestep of 4 hours was selected for the full western US model run to balance the objectives of computational efficiency and model performance. The station median MAPE of maxswe, MAPE of snow duration, and RMSE for the 4 hour time step were 17.8%, 11.9%, and 75.4 mm, respectively. We note that simulations without the modification for shallow snowpacks degraded more consistently and significantly with coarsening temporal resolution (Figure B.4).

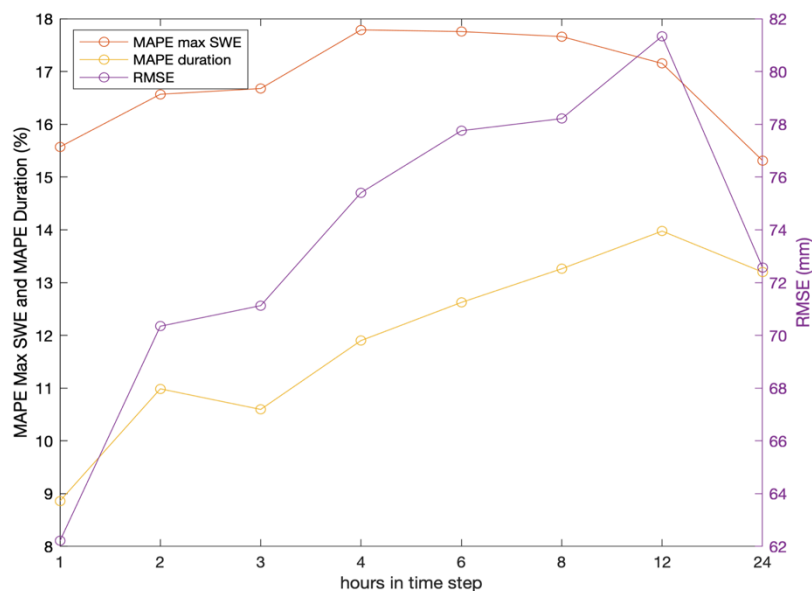


Figure 3.4 Snow model performance for different time steps using the parameter set selected in calibration of the hourly model. Points represent median values across 170 SNOTEL sites.

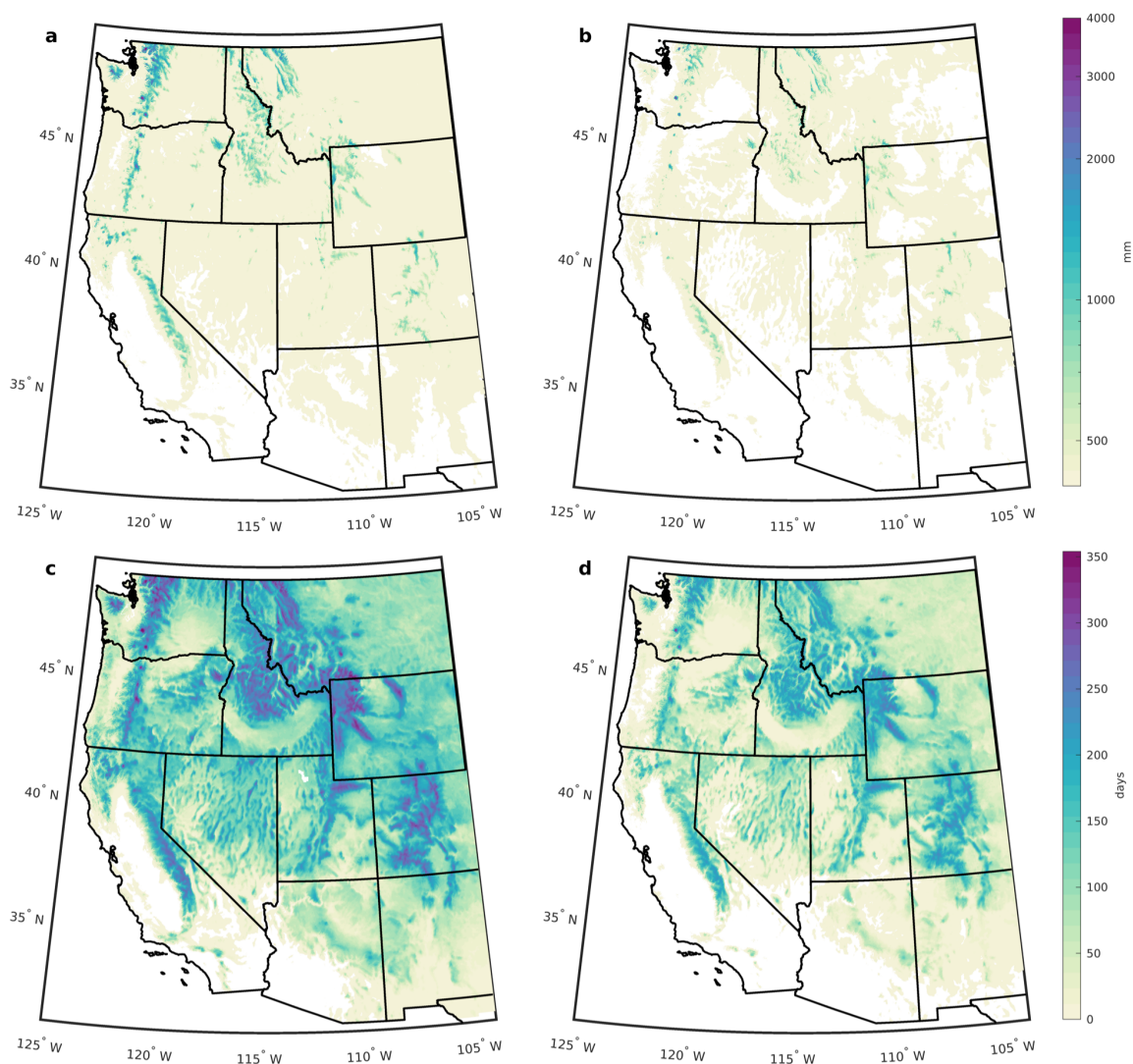


Figure 3.5 a) Historical and b) future maxswe (mm), c) historical and d) future snow duration (days). Historical values are averages over the period 2000-2013. Future values represent averages during the period 2071-2100 under RCP 8.5. In a) and b), white land areas denote areas that had less than 10 mm maxswe. In c) and d), white land areas denote areas where snow duration was 0. Note the non-linear colorscale in panels a) and b).

Model Results for the Western United States

The SnowClim model was applied to the western US (contiguous US west of 104°W) using the parameters identified above, a temporal resolution of 4 hours, and a variable spatial resolution as described previously (210m-1050m horizontal resolution). The model was run in parallel on a high-performance computer with 34 cores and 128GB RAM. The compute time for downscaling climate forcing and executing the snow model was 10 days and 3.5 days, respectively for the historical period.

Historical maxswe was 115 mm, spatially averaged across the full western US domain, and locations with historical maxswe < 10mm were largely restricted to the southern and southwestern portions of the domain (Figure 3.5a). Under the future scenario, the areas with maxswe < 10 mm greatly expanded to encompass many lower elevation areas and spatially averaged maxswe declined to 55 mm (Figure 3.5b). Historical snow duration averaged 115 days (Figure 3.5c), but declined to 56 days in the future scenario (Figure 3.5d). There were only a handful of locations with increases in maxswe or duration in the future period compared with the historical period, and these increases were small (Figure 3.6). The largest relative declines in maxswe and duration were found at low elevations. On average, maxswe and snow duration decreased by 55% and 57%, respectively.

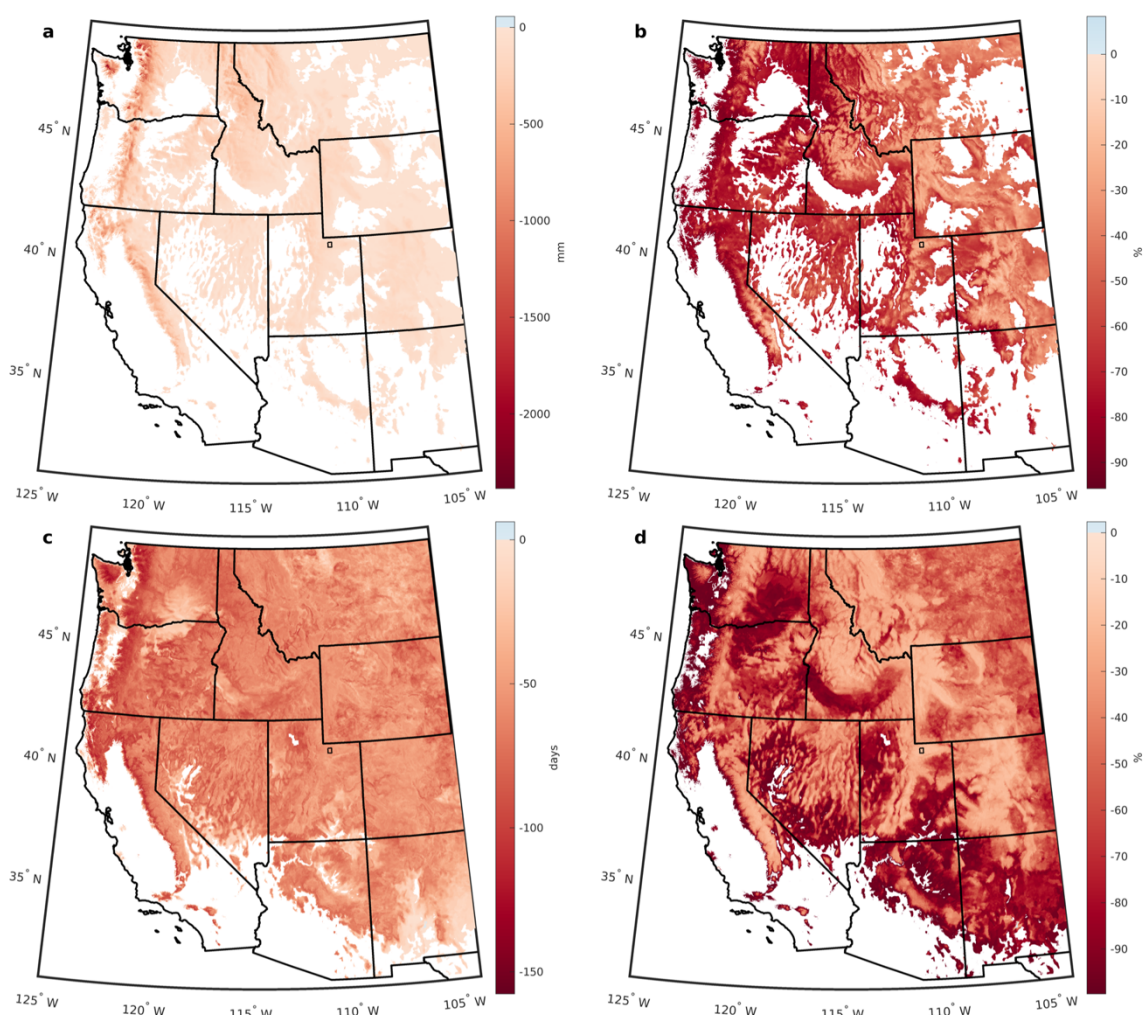


Figure 3.6 a) Absolute and b) percent change in maxswe between historical and future periods. c) Absolute and d) percent change in snow duration between historical and future periods. Small box in northern Utah indicates the region highlighted in Figure 3.7.

Compared to existing large extent, multitemporal, physics-based snow datasets such as that from the 4 km WRF runs (Liu et al., 2017), SnowClim provided a much more nuanced picture of changing snow, particularly in areas of complex terrain. For example, Figure 3.7 shows relative changes in maxswe for the Uinta Mountains in northeastern Utah as simulated directly by the 4 km WRF product and by SnowClim. SnowClim captured effects of elevation and aspect, including greater percent reductions in maxswe at lower elevations and on south facing aspects, similar to Barsugli et al., (2020). Nuanced results such as these are only possible with high-resolution, physics-based snow modeling.

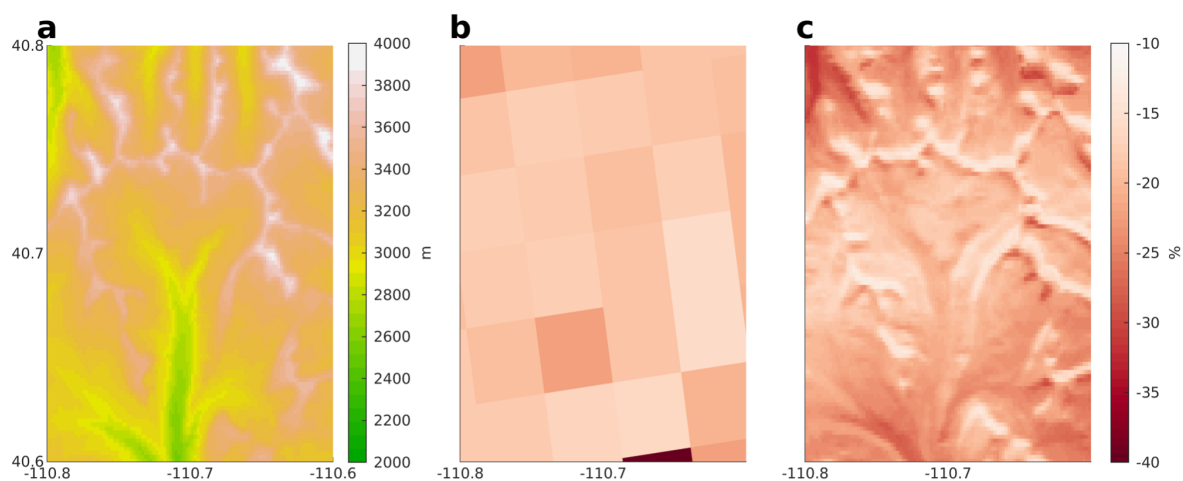


Figure 3.7 Example of simulations of changing maxswe for a portion of the Uinta Mountains, Utah (location is marked in Figure 3.6). The elevation (m) of the domain is shown in a). The percent change (%) in maxswe between historical and late 21st century periods as simulated by a 4 km WRF product (Liu et al., 2017) is shown in b) and the same metric but from the SnowClim dataset is shown in c).

Data Availability

Climate forcing data and modeled snow variables were aggregated to monthly and annual climatologies for each time period to create the SnowClim dataset (Table 3.4).

Table 3.4 Summary climate and snow variables included in the SnowClim dataset. Summary variables are available for pre-industrial, historical, and future time periods.

Climate Variables
Monthly temperature (min, max, and mean)
Monthly precipitation
Monthly solar radiation
Monthly dewpoint temperature
Annual number of freeze/thaw cycles
Snow Variables
Monthly SWE
Monthly snow depth
Monthly snow cover days
Monthly snowfall
Annual size and date of maximum SWE
Annual size and date of largest snowfall event
Annual snow duration
Date of first and last snow
Number of days without snow between first and last snow

Discussion and Conclusions

Through the development of a new computationally efficient snow model, SnowClim, and novel forcing data, we have overcome the two major hurdles to achieving snow data that meets the criteria outlined in the introduction. SnowClim's unique balance of mostly physical and some empirical components allows it to capture contrasts in radiative loading in complex terrain, timing and rate of ablation, and responses to future climate, while maintaining computational efficiency. The SnowClim dataset is spatially continuous across the western US at sub-kilometer resolution in complex terrain, enabling both high-resolution and large-extent analyses. The inclusion of multiple snow variables and compatible climate variables

across multiple time periods will empower analyses of hydroclimatic responses to changing climate.

The SnowClim model excludes some processes that might be included in more complex, computationally expensive models, such as vegetation related processes and snow redistribution processes. In some contexts, these may be necessary for accurate modeling of the snowpack (Freudiger et al., 2017; Musselman et al., 2008). Given the complexity of vegetation-snow processes, incorporation of vegetation effects may add significant computational expense and is hindered by the need for vegetation related data and parameters that are expected to change between the time periods considered here. However, incorporation of an optional vegetation routine to be used when data and computational resources are available is a logical next step. As it is, the SnowClim data can be considered a potential snow layer in vegetated areas and is expected to be most realistic in minimally vegetated areas with low amounts of snow redistribution. The model also includes simplified representations of the ground heat flux and snow surface temperature, which may be better captured by more physics-based approaches. In particular, a more nuanced treatment of the ground heat flux may be desired in warm snow climates (Mazurkiewicz et al., 2008).

Contrasts between modeled and observed snow metrics stem from several factors, including but not limited to: uncertainties in climate forcings, SNOTEL site specific factors that the model neglects such as fine scale topographic and vegetation patterns, and errors in model specification including process representation and calibration. Despite these factors, errors at SNOTEL sites from the hourly SnowClim model run were relatively small and compared well with errors reported for other gridded snow products. Ikeda et al., (2021) evaluated the snow simulations from the same 4 km WRF model runs that we sourced our raw climate forcings from Liu et al., (2017). Relative to SNOTEL sites, they found a -26.2% bias in maxswe. In contrast, the SnowClim model achieves a maxswe bias of only 0.15%. Wrzesien et al., (2018) compared maxswe at SNOTEL sites to maxswe from 9 km WRF simulations. Across sites, they found a correlation coefficient of 0.55 and a bias of -89 mm. SnowClim achieves a correlation coefficient of 0.94 and bias of -11 mm. In the Sierra Nevadas, Guan et al., (2013) blended modeled, remotely sensed, and observed data to capture SWE at 6 sites. Their method achieved a SWE RMSE of 205 mm compared to snow surveys. The SnowClim mean RMSE of daily SWE was 77 mm across all sites and 166 mm at Sierra

Nevada sites. While errors at SNOTEL sites were generally low, the model did tend to overestimate maxswe and duration at some warm/wet sites and underestimate these metrics at dry sites (Figure B.2). Further evaluation of the parameters used here in more marginal snow environments would lend additional confidence to the application of SnowClim data in these areas.

The flexible, modularized, structure of the SnowClim model lends itself to calibration, parameter sensitivity assessment, and experimentation. In the western US, model performance was particularly sensitive to the choice of albedo algorithm and snow surface temperature parameterization, in line with previous findings (Etchevers et al., 2004; Günther et al., 2019; Slater et al., 2001; Figure B.3). Given the importance of impurities (e.g., tree litter, dust, and black carbon) on snow albedo and consequently snow melt (Waliser et al., 2011), a future step will be to add albedo algorithms that account for these effects. The modular structure of SnowClim would make this relatively straightforward.

Given the multifaceted importance of snow and the ongoing changes to snow due to climate change, there is a need for models that can accurately and efficiently simulate snow to generate spatially extensive, high-resolution datasets to meet the diverse requirements of different applications. We anticipate that the SnowClim model and data will be powerful tools for researchers and managers across a range of disciplines including ecology and wildlife biology, recreation, transportation, hazard planning, and glacier and hydrologic modeling.

References

- Abatzoglou, J. T., & Brown, T. J. (2012). A comparison of statistical downscaling methods suited for wildfire applications. *International Journal of Climatology*, 32(5), 772–780. <https://doi.org/10.1002/joc.2312>
- Anderson, E. (2006). *Snow Accumulation and Ablation Model – SNOW-17*. 61. <https://www.wcc.nrcs.usda.gov/ftpref/wntsc/H&H/snow/AndersonSnow17.pdf>
- Anderson, E. A. (1976). *A point energy and mass balance model of a snow cover* (p. 150) [NOAA Technical Report NWS 19]. National Weather Service.
- Armstrong, R. L., & Brun, E. (2008). *Snow and Climate: Physical Processes, Surface Energy Exchange and Modeling*. Cambridge University Press.

- Bales, R. C., Molotch, N. P., Painter, T. H., Dettinger, M. D., Rice, R., & Dozier, J. (2006). Mountain hydrology of the western United States. *Water Resources Research*, 42(8). <https://doi.org/10.1029/2005WR004387>
- Barsugli, J. J., Ray, A. J., Livneh, B., Dewes, C. F., Heldmyer, A., Rangwala, I., Guinotte, J. M., & Torbit, S. (2020). Projections of Mountain Snowpack Loss for Wolverine Denning Elevations in the Rocky Mountains. *Earth's Future*, 8(10). <https://doi.org/10.1029/2020EF001537>
- Blöschl, G., & Kirnbauer, R. (1991). Point snowmelt models with different degrees of complexity—Internal processes. *Journal of Hydrology*, 129(1–4), 127–147. [https://doi.org/10.1016/0022-1694\(91\)90048-M](https://doi.org/10.1016/0022-1694(91)90048-M)
- Boone, A. (2002). *Description du Schema de Neige ISBA_ES (Explicit Snow)*. Centre National de Recherches Météorologiques, Météo-France. <https://www.umr-cnrm.fr/IMG/pdf/snowdoc.pdf>
- Braun, L. N. (1984). *Simulation of snowmelt-runoff in lowland and lower alpine regions of Switzerland* [Dissertation, ETH Zurich]. <https://doi.org/10.3929/ETHZ-A-000334295>
- Burakowski, E., & Magnusson, M. (2012). *Climate Impacts on the Winter Tourism Economy in the United States*. Prepared for Protect Our Winters (POW) and Natural Resources Defense Council (NRDC). <https://scholars.unh.edu/cgi/viewcontent.cgi?article=1020&context=sustainability>
- Choi, G., Robinson, D. A., & Kang, S. (2010). Changing Northern Hemisphere Snow Seasons. *Journal of Climate*, 23(19), 5305–5310. <https://doi.org/10.1175/2010JCLI3644.1>
- Cohen, J. (1994). Snow cover and climate. *Weather*, 49(5), 150–156. <https://doi.org/10.1002/j.1477-8696.1994.tb05997.x>
- Corripio, M. J. G. (2015). *Insol: Solar Radiation. R package version 1.2.1*. <https://CRAN.R-project.org/package=insol>
- Dee, D. P., Uppala, S. M., Simmons, A. J., Berrisford, P., Poli, P., Kobayashi, S., Andrae, U., Balmaseda, M. A., Balsamo, G., Bauer, P., Bechtold, P., Beljaars, A. C. M., van de Berg, L., Bidlot, J., Bormann, N., Delsol, C., Dragani, R., Fuentes, M., Geer, A. J., ... Vitart, F. (2011). The ERA-Interim reanalysis: Configuration and performance of the

- data assimilation system. *Quarterly Journal of the Royal Meteorological Society*, 137(656), 553–597. <https://doi.org/10.1002/qj.828>
- Dettinger, M. (2011). Climate Change, Atmospheric Rivers, and Floods in California - A Multimodel Analysis of Storm Frequency and Magnitude Changes 1: Climate Change, Atmospheric Rivers, and Floods in California - A Multimodel Analysis of Storm Frequency and Magnitude Changes. *JAWRA Journal of the American Water Resources Association*, 47(3), 514–523. <https://doi.org/10.1111/j.1752-1688.2011.00546.x>
- DeWalle, D., & Rango, A. (2008). *Principles of Snow Hydrology*. Cambridge University Press. doi:10.1017/CBO9780511535673
- Dietrich, H., Wolf, T., Kawohl, T., Wehberg, J., Kändler, G., Mette, T., Röder, A., & Böhner, J. (2019). Temporal and spatial high-resolution climate data from 1961 to 2100 for the German National Forest Inventory (NFI). *Annals of Forest Science*, 76(1), 6. <https://doi.org/10.1007/s13595-018-0788-5>
- Douville, H., Royer, J.-F., & Mahfouf, J.-F. (1995). A new snow parameterization for the Meteo-France climate model. Part I: validation in stand-alone experiments. *Climate Dynamics*, 12(1), 21–35. <https://doi.org/10.1007/s003820050092>
- Eira, I. M. G., Jaedicke, C., Magga, O. H., Maynard, N. G., Vikhamar-Schuler, D., & Mathiesen, S. D. (2013). Traditional Sámi snow terminology and physical snow classification—Two ways of knowing. *Cold Regions Science and Technology*, 85, 117–130. <https://doi.org/10.1016/j.coldregions.2012.09.004>
- Essery, R., Morin, S., Lejeune, Y., & B Ménard, C. (2013). A comparison of 1701 snow models using observations from an alpine site. *Advances in Water Resources*, 55, 131–148. <https://doi.org/10.1016/j.advwatres.2012.07.013>
- Etchevers, P., Martin, E., Brown, R., Fierz, C., Lejeune, Y., Bazile, E., Boone, A., Dai, Y. J., Essery, R., Fernandez, A., Gusev, Y., Jordan, R., Koren, V., Kowalczyk, E., Pyles, R. D., Schlosser, A., Shmakin, A. B., Smirnova, T. G., Strasser, U., ... Yang, Z. L. (2002). *SnowMIP- An Intercomparison of Snow Models: First Results*. International Snow Science Workshop, Penticton, British Columbia.
- Etchevers, P., Martin, E., Brown, R., Fierz, C., Lejeune, Y., Bazile, E., Boone, A., Dai, Y.-J., Essery, R., Fernandez, A., Gusev, Y., Jordan, R., Koren, V., Kowalczyk, E.,

- Nasonova, N. O., Pyles, R. D., Schlosser, A., Shmakin, A. B., Smirnova, T. G., ... Yang, Z.-L. (2004). Validation of the energy budget of an alpine snowpack simulated by several snow models (Snow MIP project). *Annals of Glaciology*, 38, 150–158. <https://doi.org/10.3189/172756404781814825>
- Fick, S. E., & Hijmans, R. J. (2017). WorldClim 2: New 1-km spatial resolution climate surfaces for global land areas. *International Journal of Climatology*, 37(12), 4302–4315. <https://doi.org/10.1002/joc.5086>
- Formozov, A. N. (1964). *Snow cover as an integral factor of the environment and its importance in the ecology of mammals and birds*. Boreal Institute for Northern Studies, The University of Alberta.
- Fountain, A. G., Campbell, J. L., Schuur, E. A. G., Stammerjohn, S. E., Williams, M. W., & Ducklow, H. W. (2012). The Disappearing Cryosphere: Impacts and Ecosystem Responses to Rapid Cryosphere Loss. *BioScience*, 62(4), 405–415. <https://doi.org/10.1525/bio.2012.62.4.11>
- Freudiger, D., Kohn, I., Seibert, J., Stahl, K., & Weiler, M. (2017). Snow redistribution for the hydrological modeling of alpine catchments. *Wiley Interdisciplinary Reviews: Water*, 4(5), e1232. <https://doi.org/10.1002/wat2.1232>
- Fritze, H., Stewart, I. T., & Pebesma, E. (2011). Shifts in Western North American Snowmelt Runoff Regimes for the Recent Warm Decades. *Journal of Hydrometeorology*, 12(5), 989–1006. <https://doi.org/10.1175/2011JHM1360.1>
- Fyfe, J. C., Derksen, C., Mudryk, L., Flato, G. M., Santer, B. D., Swart, N. C., Molotch, N. P., Zhang, X., Wan, H., Arora, V. K., Scinocca, J., & Jiao, Y. (2017). Large near-term projected snowpack loss over the western United States. *Nature Communications*, 8. <https://doi.org/10.1038/ncomms14996>
- Garen, D. C., & Marks, D. (2005). Spatially distributed energy balance snowmelt modelling in a mountainous river basin: Estimation of meteorological inputs and verification of model results. *Journal of Hydrology*, 315(1–4), 126–153. <https://doi.org/10.1016/j.jhydrol.2005.03.026>
- Gergel, D. R., Nijssen, B., Abatzoglou, J. T., Lettenmaier, D. P., & Stumbaugh, M. R. (2017). Effects of climate change on snowpack and fire potential in the western USA. *Climatic Change*, 141(2), 287–299. <https://doi.org/10.1007/s10584-017-1899-y>

- Gesch, D. B., Evans, G. A., Oimoen, M. J., & Arundel, S. (2018). *The National Elevation Dataset* (pp. 83–110). American Society for Photogrammetry and Remote Sensing; USGS Publications Warehouse. <http://pubs.er.usgs.gov/publication/70201572>
- Grippa, M., Kergoat, L., Le Toan, T., Mognard, N. M., Delbart, N., L'Hermitte, J., & Vicente-Serrano, S. M. (2005). The impact of snow depth and snowmelt on the vegetation variability over central Siberia. *Geophysical Research Letters*, *32*(21), L21412. <https://doi.org/10.1029/2005GL024286>
- Guan, B., Molotch, N. P., Waliser, D. E., Jepsen, S. M., Painter, T. H., & Dozier, J. (2013). Snow water equivalent in the Sierra Nevada: Blending snow sensor observations with snowmelt model simulations. *Water Resources Research*, *49*(8), 5029–5046. <https://doi.org/10.1002/wrcr.20387>
- Günther, D., Marke, T., Essery, R., & Strasser, U. (2019). Uncertainties in Snowpack Simulations—Assessing the Impact of Model Structure, Parameter Choice, and Forcing Data Error on Point-Scale Energy Balance Snow Model Performance. *Water Resources Research*, *55*(4), 2779–2800. <https://doi.org/10.1029/2018WR023403>
- Hamman, J. J., Nijssen, B., Bohn, T. J., Gergel, D. R., & Mao, Y. (2018). The Variable Infiltration Capacity model version 5 (VIC-5): Infrastructure improvements for new applications and reproducibility. *Geoscientific Model Development*, *11*(8), 3481–3496. <https://doi.org/10.5194/gmd-11-3481-2018>
- Havens, S., Marks, D., FitzGerald, K., Masarik, M., Flores, A. N., Kormos, P., & Hedrick, A. (2019). Approximating Input Data to a Snowmelt Model Using Weather Research and Forecasting Model Outputs in Lieu of Meteorological Measurements. *Journal of Hydrometeorology*, *20*(5), 847–862. <https://doi.org/10.1175/JHM-D-18-0146.1>
- Helgason, W., & Pomeroy, J. (2012). Problems Closing the Energy Balance over a Homogeneous Snow Cover during Midwinter. *Journal of Hydrometeorology*, *13*(2), 557–572. <https://doi.org/10.1175/JHM-D-11-0135.1>
- Holden, Z. A., Abatzoglou, J. T., Luce, C. H., & Baggett, L. S. (2011). Empirical downscaling of daily minimum air temperature at very fine resolutions in complex terrain. *Agricultural and Forest Meteorology*, *151*(8), 1066–1073. <https://doi.org/10.1016/j.agrformet.2011.03.011>

- Holden, Z. A., Swanson, A., Klene, A. E., Abatzoglou, J. T., Dobrowski, S. Z., Cushman, S. A., Squires, J., Moisen, G. G., & Oyler, J. W. (2016). Development of high-resolution (250 m) historical daily gridded air temperature data using reanalysis and distributed sensor networks for the US Northern Rocky Mountains. *International Journal of Climatology*, *36*(10), 3620–3632. <https://doi.org/10.1002/joc.4580>
- Huss, M., Bookhagen, B., Huggel, C., Jacobsen, D., Bradley, R. S., Clague, J. J., Vuille, M., Buytaert, W., Cayan, D. R., Greenwood, G., Mark, B. G., Milner, A. M., Weingartner, R., & Winder, M. (2017). Toward mountains without permanent snow and ice. *Earth's Future*, *5*(5), 2016EF000514. <https://doi.org/10.1002/2016EF000514>
- Ikeda, K., Rasmussen, R., Liu, C., Newman, A., Chen, F., Barlage, M., Gutmann, E., Dudhia, J., Dai, A., Luce, C., & Musselman, K. (2021). Snowfall and snowpack in the Western U.S. as captured by convection permitting climate simulations: Current climate and pseudo global warming future climate. *Climate Dynamics*. <https://doi.org/10.1007/s00382-021-05805-w>
- Jennings, K. S., Kittel, T. G. F., & Molotch, N. P. (2018). Observations and simulations of the seasonal evolution of snowpack cold content and its relation to snowmelt and the snowpack energy budget. *The Cryosphere*, *12*(5), 1595–1614. <https://doi.org/10.5194/tc-12-1595-2018>
- Jennings, K. S., Winchell, T. S., Livneh, B., & Molotch, N. P. (2018). Spatial variation of the rain–snow temperature threshold across the Northern Hemisphere. *Nature Communications*, *9*(1), 1148. <https://doi.org/10.1038/s41467-018-03629-7>
- Jones, H. G. (1999). The ecology of snow-covered systems: A brief overview of nutrient cycling and life in the cold. *Hydrological Processes*, *13*, 13.
- Jordan, R. (1991). *A one-dimensional temperature model for a snow cover: Technical documentation for SNTHERM.89* [Special Report 91-16]. Cold Regions Research and Engineering Laboratory.
- Khu, S. T., & Madsen, H. (2005). Multiobjective calibration with Pareto preference ordering: An application to rainfall-runoff model calibration. *Water Resources Research*, *41*(3). <https://doi.org/10.1029/2004WR003041>

- Knowles, N., Dettinger, M. D., & Cayan, D. R. (2006). Trends in Snowfall versus Rainfall in the Western United States. *Journal of Climate*, *19*(18), 4545–4559.
<https://doi.org/10.1175/JCLI3850.1>
- Kumar, M., Marks, D., Dozier, J., Reba, M., & Winstral, A. (2013). Evaluation of distributed hydrologic impacts of temperature-index and energy-based snow models. *Advances in Water Resources*, *56*, 77–89. <https://doi.org/10.1016/j.advwatres.2013.03.006>
- Liang, X., Lettenmaier, D. P., Wood, E. F., & Burges, S. J. (1994). A simple hydrologically based model of land surface water and energy fluxes for general circulation models. *Journal of Geophysical Research*, *99*(D7), 14415. <https://doi.org/10.1029/94JD00483>
- Liston, G. E., & Elder, K. (2006). A Distributed Snow-Evolution Modeling System (SnowModel). *Journal of Hydrometeorology*, *7*(6), 1259–1276.
<https://doi.org/10.1175/JHM548.1>
- Liu, C., Ikeda, K., Rasmussen, R., Barlage, M., Newman, A. J., Prein, A. F., Chen, F., Chen, L., Clark, M., Dai, A., Dudhia, J., Eidhammer, T., Gochis, D., Gutmann, E., Kurkute, S., Li, Y., Thompson, G., & Yates, D. (2017). Continental-scale convection-permitting modeling of the current and future climate of North America. *Climate Dynamics*, *49*(1–2), 71–95. <https://doi.org/10.1007/s00382-016-3327-9>
- Louis, J.-F. (1979). A parametric model of vertical eddy fluxes in the atmosphere. *Boundary-Layer Meteorology*, *17*(2), 187–202. <https://doi.org/10.1007/BF00117978>
- Luce, C. H., Abatzoglou, J. T., & Holden, Z. A. (2013). The Missing Mountain Water: Slower Westerlies Decrease Orographic Enhancement in the Pacific Northwest USA. *Science*, *342*(6164), 1360–1364. <https://doi.org/10.1126/science.1242335>
- Luce, C., Staab, B., Kramer, M., Wenger, S., Isaak, D., & McConnell, C. (2014). Sensitivity of summer stream temperatures to climate variability in the Pacific Northwest. *Water Resources Research*, *50*(4), 3428–3443. <https://doi.org/10.1002/2013WR014329>
- Lute, A. C., & Abatzoglou, J. T. (2021). Best practices for estimating near-surface air temperature lapse rates. *International Journal of Climatology*, *41*(S1).
<https://doi.org/10.1002/joc.6668>
- Lute, A. C., Abatzoglou, J. T., & Hegewisch, K. C. (2015). Projected changes in snowfall extremes and interannual variability of snowfall in the western United States. *Water Resources Research*, *51*(2), 960–972. <https://doi.org/10.1002/2014WR016267>

- Marks, D., Domingo, J., Susong, D., Link, T., & Garen, D. (1999). A spatially distributed energy balance snowmelt model for application in mountain basins. *Hydrological Processes*, 13(12–13), 1935–1959. [https://doi.org/10.1002/\(SICI\)1099-1085\(199909\)13:12/13<1935::AID-HYP868>3.0.CO;2-C](https://doi.org/10.1002/(SICI)1099-1085(199909)13:12/13<1935::AID-HYP868>3.0.CO;2-C)
- Marks, D., Winstral, A., Reba, M., Pomeroy, J., & Kumar, M. (2013). An evaluation of methods for determining during-storm precipitation phase and the rain/snow transition elevation at the surface in a mountain basin. *Advances in Water Resources*, 55, 98–110. <https://doi.org/10.1016/j.advwatres.2012.11.012>
- Marsh, C. B., Pomeroy, J. W., & Wheeler, H. S. (2020). The Canadian Hydrological Model (CHM) v1.0: A multi-scale, multi-extent, variable-complexity hydrological model - design and overview. *Geoscientific Model Development*, 13(1), 225–247. <https://doi.org/10.5194/gmd-13-225-2020>
- Marsh, P. (1991). Water flux in melting snow covers. In *Advances in Porous Media* (Vol. 1, pp. 61–124). Elsevier Science Publishing.
- Marshall, A. M., Abatzoglou, J. T., Link, T. E., & Tennant, C. J. (2019). Projected Changes in Interannual Variability of Peak Snowpack Amount and Timing in the Western United States. *Geophysical Research Letters*, 46(15), 8882–8892. <https://doi.org/10.1029/2019GL083770>
- Marshall, A. M., Link, T. E., Robinson, A. P., & Abatzoglou, J. T. (2020). Higher Snowfall Intensity is Associated with Reduced Impacts of Warming Upon Winter Snow Ablation. *Geophysical Research Letters*, 47(4). <https://doi.org/10.1029/2019GL086409>
- Marshall, S. (2012). *The cryosphere*. Princeton University Press.
- Mazurkiewicz, A. B., Callery, D. G., & McDonnell, J. J. (2008). Assessing the controls of the snow energy balance and water available for runoff in a rain-on-snow environment. *Journal of Hydrology*, 354(1–4), 1–14. <https://doi.org/10.1016/j.jhydrol.2007.12.027>
- McLaughlin, B. C., Ackerly, D. D., Klos, P. Z., Natali, J., Dawson, T. E., & Thompson, S. E. (2017). Hydrologic refugia, plants, and climate change. *Global Change Biology*, 23(8), 2941–2961. <https://doi.org/10.1111/gcb.13629>

- Mergen, B. (1997). Snow in America. *Weatherwise*, 50(6), 18–26.
<https://doi.org/10.1080/00431672.1997.9926090>
- Mitchell, T. D. (2003). Pattern Scaling: An Examination of the Accuracy of the Technique for Describing Future Climates. *Climatic Change*, 60, 217–242.
- Mote, P. W., Li, S., Lettenmaier, D. P., Xiao, M., & Engel, R. (2018). Dramatic declines in snowpack in the western US. *Npj Climate and Atmospheric Science*, 1(1).
<https://doi.org/10.1038/s41612-018-0012-1>
- Musselman, K. N., Clark, M. P., Liu, C., Ikeda, K., & Rasmussen, R. (2017). Slower snowmelt in a warmer world. *Nature Climate Change*, 7(3), 214–219.
<https://doi.org/10.1038/nclimate3225>
- Musselman, K. N., Lehner, F., Ikeda, K., Clark, M. P., Prein, A. F., Liu, C., Barlage, M., & Rasmussen, R. (2018). Projected increases and shifts in rain-on-snow flood risk over western North America. *Nature Climate Change*, 8(9), 808–812.
<https://doi.org/10.1038/s41558-018-0236-4>
- Musselman, K. N., Molotch, N. P., & Brooks, P. D. (2008). Effects of vegetation on snow accumulation and ablation in a mid-latitude sub-alpine forest. *Hydrological Processes*, 22(15), 2767–2776. <https://doi.org/10.1002/hyp.7050>
- National Operational Hydrologic Remote Sensing Center. (2004). *Snow Data Assimilation System (SNODAS) Data Products at NSIDC, Version 1*. NSIDC: National Snow and Ice Data Center. <https://doi.org/10.7265/N5TB14TC>
- Oleson, K., Dai, Y., Bonan, G., Bosilovich, M., Dickinson, R., Dirmeyer, P., Hoffman, F., Houser, P., Levis, S., Niu, G.-Y., Thornton, P., Vertenstein, M., Yang, Z.-L., & Zeng, X. (2004). *Technical Description of the Community Land Model (CLM)* (p. 2497 KB) [Application/pdf]. UCAR/NCAR. <https://doi.org/10.5065/D6N877R0>
- Praskievicz, S. (2018). Downscaling climate-model output in mountainous terrain using local topographic lapse rates for hydrologic modeling of climate-change impacts. *Physical Geography*, 39(2), 99–117. <https://doi.org/10.1080/02723646.2017.1378555>
- PRISM Climate Group. (2015). Oregon State University. <http://prism.oregonstate.edu>
- Qin, Y., Abatzoglou, J. T., Siebert, S., Huning, L. S., AghaKouchak, A., Mankin, J. S., Hong, C., Tong, D., Davis, S. J., & Mueller, N. D. (2020). Agricultural risks from changing

- snowmelt. *Nature Climate Change*, 10(5), 459–465. <https://doi.org/10.1038/s41558-020-0746-8>
- Raleigh, M. S., & Clark, M. P. (2014). Are temperature-index models appropriate for assessing climate change impacts on snowmelt? *Proceedings of the Western Snow Conference*. Western Snow Conference, Durango, CO.
- Raleigh, M. S., Landry, C. C., Hayashi, M., Quinton, W. L., & Lundquist, J. D. (2013). Approximating snow surface temperature from standard temperature and humidity data: New possibilities for snow model and remote sensing evaluation. *Water Resources Research*, 49(12), 8053–8069. <https://doi.org/10.1002/2013WR013958>
- Rudisill, W., Flores, A., & McNamara, J. (2021). The Impact of Initial Snow Conditions on the Numerical Weather Simulation of a Northern Rockies Atmospheric River. *Journal of Hydrometeorology*, 22(1), 155–167. <https://doi.org/10.1175/JHM-D-20-0018.1>
- Seeherman, J., & Liu, Y. (2015). Effects of extraordinary snowfall on traffic safety. *Accident Analysis & Prevention*, 81, 194–203. <https://doi.org/10.1016/j.aap.2015.04.029>
- Sexstone, G. A., Clow, D. W., Fassnacht, S. R., Liston, G. E., Hiemstra, C. A., Knowles, J. F., & Penn, C. A. (2018). Snow Sublimation in Mountain Environments and Its Sensitivity to Forest Disturbance and Climate Warming. *Water Resources Research*, 54(2), 1191–1211. <https://doi.org/10.1002/2017WR021172>
- Slater, A. G., Schlosser, C. A., Desborough, C. E., Pitman, A. J., Henderson-Sellers, A., Robock, A., Vinnikov, K. Y., Mitchell, K., Boone, A., Braden, H., Chen, F., Cox, P. M., Rosnay, P. D., Dickinson, R. E., Gusev, Y. M., Habets, F., Kim, J., Koren, V., Kowalczyk, E. A., ... Xue, Y. (2001). The Representation of Snow in Land Surface Schemes: Results from PILPS 2(d). *Journal of Hydrometeorology*, 2, 19.
- Sohrabi, M. M., Tonina, D., Benjankar, R., Kumar, M., Kormos, P., Marks, D., & Luce, C. (2019). On the role of spatial resolution on snow estimates using a process-based snow model across a range of climatology and elevation. *Hydrological Processes*, 33(8), 1260–1275. <https://doi.org/10.1002/hyp.13397>
- Stiegler, C., Lund, M., Christensen, T. R., Mastepanov, M., & Lindroth, A. (2016). Two years with extreme and little snowfall: Effects on energy partitioning and surface

- energy exchange in a high-Arctic tundra ecosystem. *The Cryosphere*, 10(4), 1395–1413. <https://doi.org/10.5194/tc-10-1395-2016>
- Sturm, M., Goldstein, M. A., & Parr, C. (2017). Water and life from snow: A trillion dollar science question. *Water Resources Research*, 53(5), 3534–3544. <https://doi.org/10.1002/2017WR020840>
- Tarboton, D. G., & Luce, C. H. (1996). *Utah Energy Balance Snow Accumulation and Melt Model (UEB): Computer model technical description and user guide*. Utah Water Research Laboratory and USDA Forest Service Rocky Mountain Research Station.
- Taylor, K. E., Stouffer, R. J., & Meehl, G. A. (2012). An Overview of CMIP5 and the Experiment Design. *Bulletin of the American Meteorological Society*, 93(4), 485–498. <https://doi.org/10.1175/BAMS-D-11-00094.1>
- Thornton, P. E., Thornton, M. M., Mayer, B. W., Wilhelmi, N., Wei, Y., Devarakonda, R., & Cook, R. B. (2014). *Daymet: Daily surface weather data on a 1-km grid for North America, version 2* [Data set]. Oak Ridge National Laboratory (ORNL).
- Waliser, D., Kim, J., Xue, Y., Chao, Y., Eldering, A., Fovell, R., Hall, A., Li, Q., Liou, K. N., McWilliams, J., Kapnick, S., Vasic, R., De Sale, F., & Yu, Y. (2011). Simulating cold season snowpack: Impacts of snow albedo and multi-layer snow physics. *Climatic Change*, 109(S1), 95–117. <https://doi.org/10.1007/s10584-011-0312-5>
- Walter, T. M., Brooks, E. S., McCool, D. K., King, L. G., Molnau, M., & Boll, J. (2005). Process-based snowmelt modeling: Does it require more input data than temperature-index modeling? *Journal of Hydrology*, 300(1–4), 65–75. <https://doi.org/10.1016/j.jhydrol.2004.05.002>
- Wang, T., Hamann, A., Spittlehouse, D. L., & Murdock, T. Q. (2012). ClimateWNA—High-Resolution Spatial Climate Data for Western North America. *Journal of Applied Meteorology and Climatology*, 51(1), 16–29. <https://doi.org/10.1175/JAMC-D-11-043.1>
- Wigmosta, M. S., Vail, L. W., & Lettenmaier, D. P. (1994). A distributed hydrology-vegetation model for complex terrain. *Water Resources Research*, 30(6), 1665–1679. <https://doi.org/10.1029/94WR00436>

- Winstral, A., Marks, D., & Gurney, R. (2014). Assessing the Sensitivities of a Distributed Snow Model to Forcing Data Resolution. *Journal of Hydrometeorology*, *15*(4), 1366–1383. <https://doi.org/10.1175/JHM-D-13-0169.1>
- Wrzesien, M. L., Durand, M. T., Pavelsky, T. M., Kapnick, S. B., Zhang, Y., Guo, J., & Shum, C. K. (2018). A New Estimate of North American Mountain Snow Accumulation From Regional Climate Model Simulations. *Geophysical Research Letters*, *45*(3), 1423–1432. <https://doi.org/10.1002/2017GL076664>
- You, J., Tarboton, D. G., & Luce, C. H. (2014). Modeling the snow surface temperature with a one-layer energy balance snowmelt model. *Hydrology and Earth System Sciences*, *18*(12), 5061–5076. <https://doi.org/10.5194/hess-18-5061-2014>

Chapter 4: Projected Loss of Active Rock Glaciers in the Western U.S. with Warming

Abstract

Warming is diminishing mountain snowpack and glaciers in many regions, with substantial implications for local and downstream ecosystems and societies. Rock glaciers may respond more slowly than snow or glaciers to warming due to their insulating debris layer. A slower response would enable rock glaciers to continue to provide important habitat and cool summer streamflow after snow and glaciers have diminished. However, a robust assessment of rock glacier environmental niche and future distributions across broad geographic scales is lacking, limiting our understanding of how alpine ecosystems and streamflow will respond to climate change. Using process-relevant, high-resolution covariates we develop a species distribution model of the topographic, geologic, and hydroclimatic niche of rock glaciers that provides novel estimates of potential rock glacier distributions for different climate equilibria. We show that mean annual air temperature and headwall area are the dominant controls on rock glacier spatial distributions, with rock glaciers more likely to be found in areas with mean annual temperatures below freezing and large headwalls. Guided by the assumption that modern rock glaciers are long-lived features in equilibrium with pre-industrial conditions, we find that equilibration to present hydroclimatic conditions will result in a 36% reduction in suitable rock glacier habitat and equilibration to late 21st century climate under RCP8.5 will result in near-complete loss (99% reduction) of rock glacier habitat across the western United States. Under present-day conditions, we find limited potential (5.5 km²) for glacier to rock glacier transformation, concentrated in cold, high elevation, moderate precipitation areas. More widespread glacier to rock glacier transformation may be limited by debris supply.

Introduction

The mountain cryosphere provides critical services including water storage, climate regulation, and habitat for cold-adapted species (Huggel et al., 2015). Rock glaciers are one component of the mountain cryosphere that is particularly important in semi-arid montane portions of the world. In the continental western United States (U.S.), the total water

equivalent of rock glaciers is estimated to be of similar magnitude to that of glaciers (Fountain et al., 2017; Jones et al., 2018; Trcka, 2020). While climate change is reducing snowpack and glacier mass balance (Huss et al., 2017; Moore et al., 2009; Mote et al., 2018), rock glaciers are hypothesized to be more resilient to warming due to their insulating debris mantle (Anderson et al., 2018); the response time of rock glaciers to warming is hundreds of years (Müller et al., 2016), much longer than the decadal response time of midlatitude glaciers (Cuffey and Paterson, 2010) and the almost immediate response time of snow. This suggests that rock glaciers may become an increasingly important source of summer water supply and refugium for cold-adapted species (Harrington et al., 2017, 2018; Jones et al., 2018; Millar et al., 2015).

Rock glaciers depend on a balance of ice and debris fluxes which are controlled by climate, topography, and lithology (Bolch & Gorbunov, 2014; Brenning & Azócar, 2010; Brenning & Trombotto, 2006; Chueca, 1992; Johnson et al., 2007; Millar & Westfall, 2008; Morris, 1981). Previous studies on these combined factors, that we term “rock glacier habitat”, have been largely descriptive, conducted at the scale of mountain ranges or small regions, and many neglected to include any hydroclimatic information despite the dependence of rock glaciers on the accumulation and ablation of snow and ice. Larger scale assessments of the influence of a more functionally relevant set of predictors may better identify the fundamental environmental niche of rock glaciers and improve understanding of rock glacier genesis and climate sensitivity.

Case studies and numerical modeling approaches have evaluated rock glacier climate sensitivity for individual or small groups of rock glaciers, finding that rock glaciers in warmer locations will deteriorate with continued warming while some conventional ice glaciers may transition to rock glaciers (Anderson et al., 2018; Delaloye et al., 2010; Jones et al., 2019; Kääb et al., 2007; Marcer et al., 2021). Glaciers that become rock glaciers are likely to persist on the landscape longer and continue to provide important services such as cool summer water supply. These past analyses have provided valuable insights into rock glacier rheologic behavior, response times, and climate sensitivity, but fall short of providing a more generalizable understanding of how rock glaciers occupy landscapes across broader scales or how they may respond to climate change. It remains unclear under what geologic,

topographic, and hydroclimatic conditions rock glaciers are likely to persist, disappear, or develop from glaciers.

We employ a machine learning approach (Maxent; Phillips et al., 2006; Phillips & Dudík, 2008) to address three primary questions: 1) What hydroclimatic, geologic, and topographic constraints describe the environmental niche of rock glaciers?; 2) How will the spatial distribution of rock glaciers change with projected climate change?; and 3) Is there potential for glacier to rock glacier transformation in the western U.S.? We address these questions by constructing a Maxent model of rock glacier distributions using datasets of known rock glacier locations and high-resolution pre-industrial hydroclimatic, geologic, and topographic predictors across the western U.S. We use this model and data reflecting present and projected late-21st century conditions under RCP8.5 to predict where rock glaciers are likely to disappear, persist, or develop from glaciers in the future. This approach elucidates generalizable controls on rock glacier spatial distributions and their climatic sensitivity and allows us to provide the first estimates of future rock glacier distributions across the western U.S.

Data and Methods

Data

We compiled a set of environmental predictors that capture the hydroclimatic, topographic, and geologic controls on rock glaciers (Table C.1). Predictors cover the western U.S. at a common 210 m spatial resolution, similar to the scale of the rock glaciers themselves (Johnson et al., 2020). We limit the western U.S. modeling domain to potential rock glacier habitat using lower montane and higher elevation classes from the mountain classification scheme of Körner et al., (2011) and a mean annual temperature threshold $< 8^{\circ}\text{C}$ (Figure 4.1). This domain contains all active rock glacier features from the inventory of Trcka, (2020; $n = 1486$), the centroids of which were used as presence locations in the Maxent models. Alpine ice glacier (hereafter glacier) outlines from the Global Land Ice Measurements from Space dataset (GLIMS; Fountain, 2006; Hoffman & Fountain, 2016) were also used for comparison with rock glaciers.

Given the rapid recent global warming and the roughly several hundred-year response time of rock glaciers to warming (Müller et al., 2016), it is unlikely that rock glaciers are in

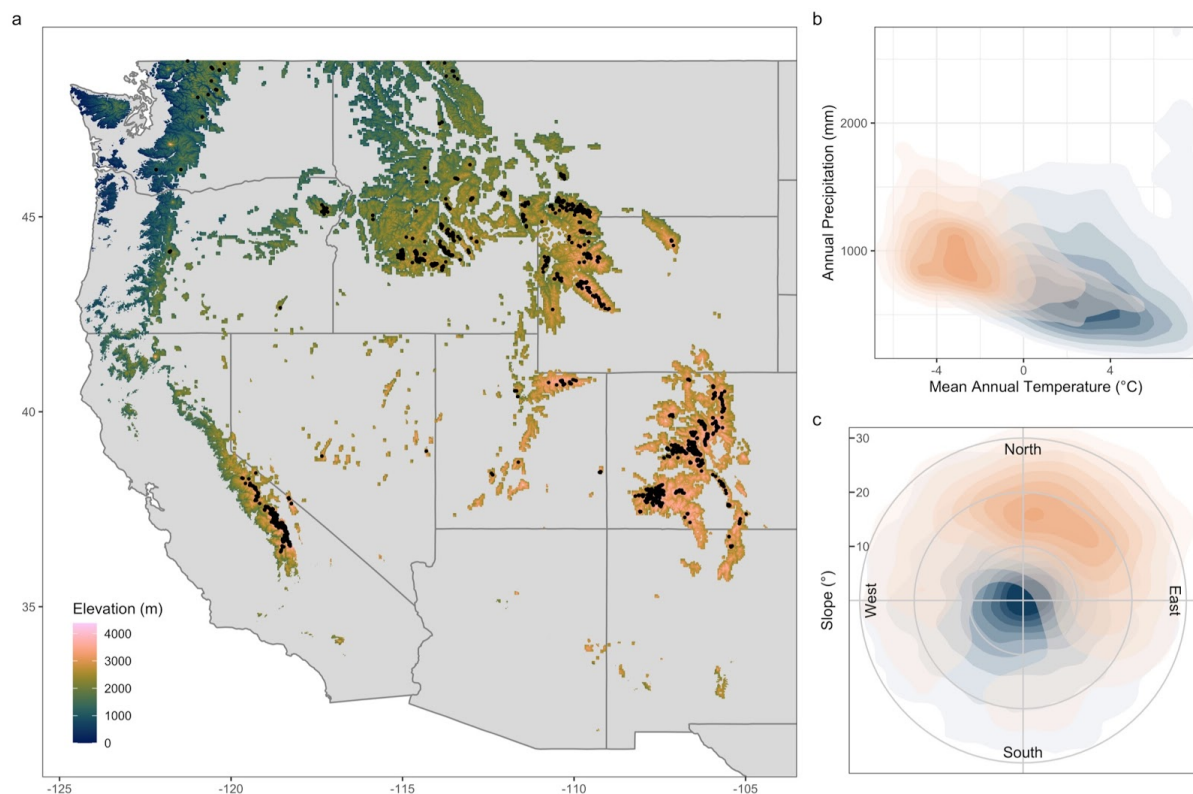


Figure 4.1 a) Modeling domain. Elevation of terrain is indicated by the color bar. Black points denote known rock glacier locations. In bivariate density plots (b and c), salmon color indicates the distribution of rock glacier locations while grey blue indicates the distribution of background domain locations in two-dimensional pre-industrial covariate space.

equilibrium with the current climate (Anderson et al., 2018). We assumed that present-day rock glaciers are a result of pre-industrial climate (1850-1879) and we developed models of the present distribution of rock glaciers using pre-industrial climate forcing. We then predicted rock glacier distributions under recent historical conditions (2000-2013; hereafter present) and future conditions under a high-warming scenario (2071-2100). Since the models are calibrated on pre-industrial conditions and current rock glacier locations, predicted rock glacier distributions for the different time periods reflect the distribution that would result once rock glaciers equilibrate to the given hydroclimatic conditions. For the present period, climatological measures of mean, minimum, and maximum annual temperatures (t_{mean} , t_{min} , t_{max}), annual number of temperature oscillations around 0°C (freeze-thaw), annual precipitation (precip), annual rainfall (rain), and annual downward solar radiation (solar) were calculated from output from the Weather Research and Forecasting model (WRF; Liu et al., 2017) statistically downscaled to ~ 210 m horizontal resolution using local

lapse rates, precipitation bias correction, and solar terrain correction (Lute et al., 2021). Pre-industrial climate covariates were created by perturbing the present period to reflect pre-industrial conditions (1850-1879) using monthly climatological differences in climate between the pre-industrial and present periods from the Fifth Coupled Model Intercomparison Project (CMIP5; Taylor et al., 2012; Lute et al., 2021). Future climate covariates were created using pseudo-global warming runs from WRF, reflecting 2071-2100 conditions under RCP8.5 (Liu et al., 2017). Both pre-industrial and future covariates were downscaled using the same methods as the present period (Lute et al., 2021). Further discussion of the predictor variables is available in Appendix C.

We also considered snow metrics calculated from an energy balance snow model (Lute et al., 2021) forced with the previously described climate datasets. These metrics include annual snowfall water equivalent (sfe), snow duration (duration), annual maximum snow water equivalent (maxswe), and the number of snow free days between the snow on and snow off dates (nosnowdays). The use of snow data enhances the physical relevance of the predictor variables relative to using variables derived from temperature and precipitation alone as is often done in environmental niche modeling, and may enhance model transferability (Austin, 2002).

Topographic factors are widely known to influence rock glaciers as they affect both debris and ice supply as well as the energy budget (Frauenfelder et al., 2003). To capture these topographic effects, terrain aspect, terrain slope, and a headwall metric (headwall3 or headwall5) were derived from the 1 arc-second National Elevation Dataset (Gesch et al., 2018), aggregated to 210 m resolution. The headwall metric was calculated as the fraction of pixels within a given radius of the target pixel that are higher elevation than the target pixel and exceed a slope threshold (e.g., Bolch & Gorbunov, 2014; Kenner & Magnusson, 2017).

Geologic factors influence the debris available for rock glaciers, thereby exerting a first order control on rock glacier distributions (Haeberli et al., 2006; Johnson et al., 2007). We used a rasterized version of a generalized lithology classification consisting of 12 rock types (Anning & Ator, 2017) to represent these effects. Rock type descriptions are provided in Table C.2.

Methods

Maxent modeling (Phillips et al., 2006; Phillips & Dudík, 2008) is a commonly used machine learning approach for environmental niche modeling that is data-driven and well-suited to large datasets. Maxent models use known species presence locations and spatial fields of predictors (i.e., background data) to construct features from the predictor data which are combined to allow modeling of complex, nonlinear relationships. Maxent's logistic output provides continuous values between 0 and 1 which can be interpreted as a measure of habitat suitability. Maxent has provided excellent performance in predicting species distributions, including under new conditions in space and time (Duque-Lazo et al., 2016; Elith et al., 2006). There has been a recent uptick in the application of Maxent in the physical sciences and glaciology in particular where it has generated new insights into surging glaciers and glacier responses to climate change (Comino et al., 2021; Manquehual-Cheuque & Somos-Valenzuela, 2021; Sevestre & Benn, 2015; Wang et al., 2021). Maxent is an ideal modeling approach for the questions posed here because it a) uses presence only data such as the rock glacier inventory, b) can handle large datasets of environmental covariates enabling high-resolution, large-extent modeling, and c) is designed to address questions about changing distributions and habitat suitability like those posed here. We implemented Maxent using the *dismo* (Hijmans et al., 2020) and *ENMeval* (Kass et al., 2021) packages in R (R Core Team, 2020). For modeling efficiency, 10,000 background points were randomly selected for model calibration, in addition to the 1486 known rock glacier locations.

Prior to running Maxent, we removed strongly collinear variables (see Appendix C, Figure C.1 for details), leaving 9 covariates. Next, to determine optimal model complexity and avoid overfitting, we built a suite of models using various levels of model complexity and evaluated model performance using the AICc statistic (Akaike, 1974; see Appendix C for details). The selected model was used to map rock glacier habitat suitability across the domain based on Maxent's logistic output.

We performed several cross validations of the model to assess model transferability geographically and to new climates. First, we split the data into 400 km blocks using the *blockCV* R package (Valavi et al., 2019) with a block size approximately ten times larger than the median effective range of spatial autocorrelation of the predictor variables (Figure C.3). Second, we split the data into cold and warm groups to evaluate potential model

transferability to a warmer climate. Specifically, we developed a model using data with pre-industrial tmean below the median value for rock glacier locations (roughly -2.8°C) and evaluated this model on the warmer half of rock glacier presence locations. The area under the receiver operating characteristic curve statistic (AUC) was used to assess model performance.

Predictor variable importance was assessed using the model jackknife approach available in Maxent. The approach calculates the loss in regularized training gain when each variable is left out of a model as well as the regularized training gain of a model built on that variable alone. We present a normalized version of the regularized training gain for ease of interpretation. The relationship of each covariate to the model predictions of presence was further evaluated by inspecting the marginal response curves that characterize the relationship between covariate values and predicted suitability of rock glacier habitat when other variables are held constant at their average value at known rock glacier locations. Additional response curves from models based on each variable in isolation are provided in Figure C.6.

The optimal model calibrated on the pre-industrial covariates and current active rock glacier locations was used to predict rock glacier habitat suitability over time by applying it to the pre-industrial, present, and future predictors. Throughout, references to results for a particular time period should be interpreted as results assuming active rock glacier equilibration to hydroclimatic conditions in that time period, not to realized changes by that time period. For example, predictions of rock glacier suitability under future hydroclimate represent the potential distribution of active rock glaciers that would result once rock glaciers reached equilibrium with the future climate, which in reality may be hundreds of years later due to the slow response of rock glaciers to warming (Müller et al., 2016).

To control predictions outside of the range of the calibration data, we used clamping, which keeps the response curve probabilities constant outside the range of calibration conditions. To define binary presence/absence thresholds in the model predictions, we used the pre-industrial suitability threshold that omitted 10% of known rock glaciers. For both the pre-industrial to present transition and the present to future transition, locations were classified into four groups depending on the change in their predicted suitability. Locations that did not exceed the threshold in either the earlier or later period were classified as ‘never

suitable'. Locations that exceeded the threshold in both periods were labeled 'persist'. Locations which were suitable in the earlier period but not in the later period were labeled 'disappear', and locations which were not suitable in the earlier period but were suitable in the later period were labeled 'enhance'. Suitable and unsuitable classifications were also used to aggregate suitability predictions by level III ecoregion (US Environmental Protection Agency, 2013; Table C.4).

Results

Pre-industrial model

Based on the multimodel evaluation approach, we identified the model with a beta parameter of 7 and linear, quadratic, threshold, and hinge feature classes as the model with the optimal balance of performance and parsimony (Figure C.2). This model achieved an AUC of 0.98 and the prediction threshold which excluded 10% of rock glaciers was 0.212. Rock glaciers excluded at this prediction threshold were scattered across the domain, with larger concentrations in Colorado and New Mexico (Figure C.4). Known rock glaciers predicted to have low suitability tended to have smaller headwall areas, more snow free days, more diverse aspects and rock types, less snowfall, more solar radiation, and warmer temperatures (Figures C.5). The mean suitability at active rock glacier locations was higher than at inactive rock glacier locations (0.72 and 0.50, respectively).

Models calibrated on portions of the domain and validated on other portions of the domain maintained high AUC values in both calibration and validation, suggesting that the model is robust to changing environmental conditions (Table C.3). In particular, a model calibrated on colder rock glacier locations exhibited no degradation in performance when applied to warmer rock glacier locations, suggesting that the model will transfer well to future climates.

Predictor Variable Importance

The model jackknife approach highlighted tmean as being the single most important variable in the rock glacier model (Figure 4.2a). Models built on headwall5, slope, and sfe alone were the next most powerful. Solar and rocktype were the two least useful predictors when used in isolation.

The relationships between each pre-industrial variable and predicted rock glacier suitability largely matched expectations based on the literature (Figure 4.2b; Figure C.6 shows response curves for each variable in isolation). Hydroclimatically, the model found that rock glaciers were most likely in areas with $t_{\text{mean}} < -1^{\circ}\text{C}$ (see also Figure 4.1), < 500 mm rainfall, less than 250 Wm^{-2} solar radiation, $\sim 500\text{-}1,500$ mm of SFE, and where the snowpack was temporally discontinuous. Rock glaciers were more likely to be found on northern aspects, on $10\text{-}30^{\circ}$ slopes, and in locations with larger headwall areas. The model showed a slight preference for metamorphic and igneous rocktypes and indicated sedimentary rocktypes were less likely to host rock glaciers.

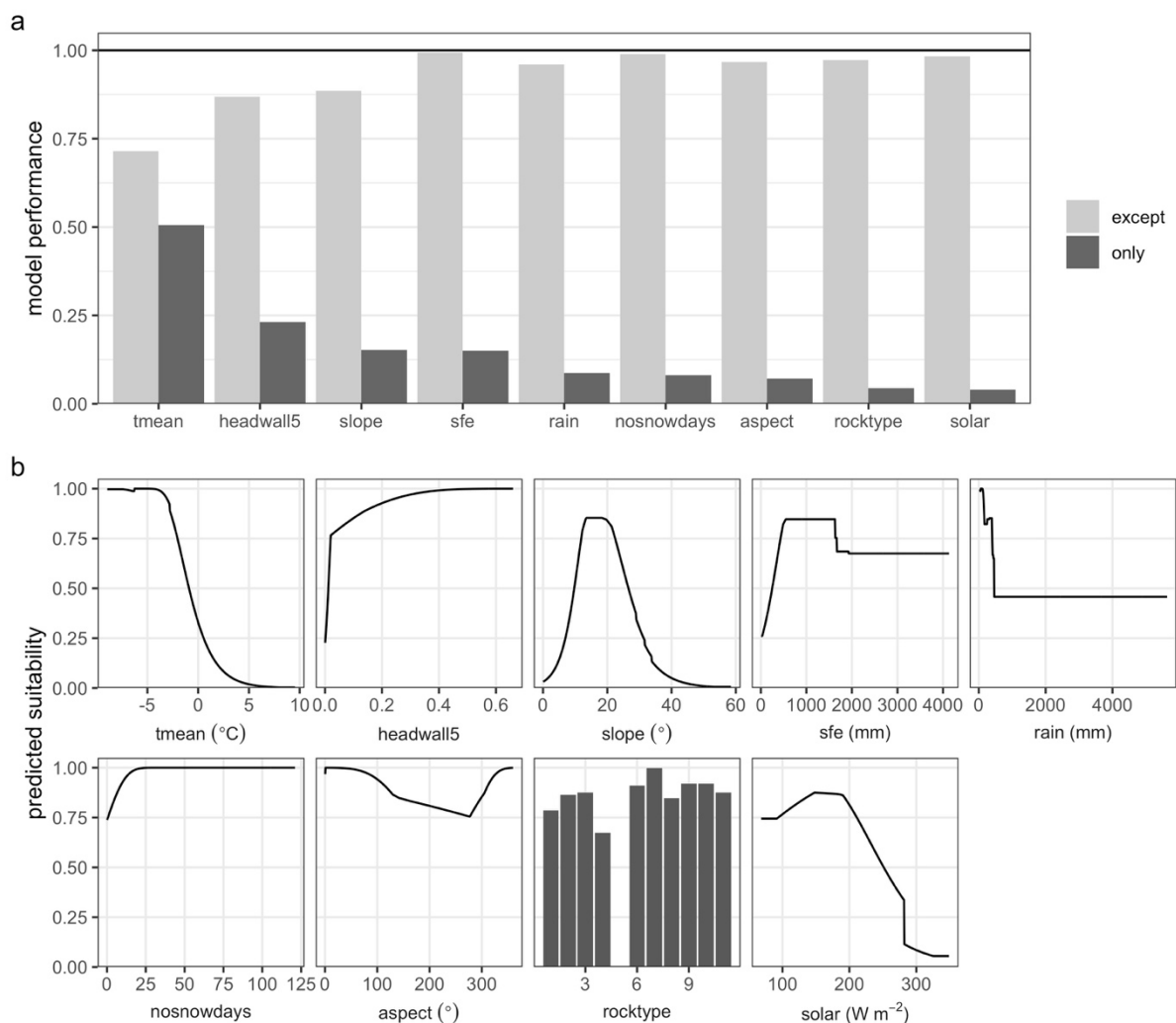


Figure 4.2 a) Importance of each variable to capturing rock glacier habitat suitability according to Maxent jackknife approach. Model performance (y-axis) is the normalized regularized training gain. Black horizontal line indicates the performance of the model with all variables. Light grey bars indicate the performance of all models built with all variables except the variable of interest. Dark grey bars indicate the performance of models built on each variable alone and determine the order of the bars. b) Marginal response functions illustrating the relationship between the covariate values (x-axis) and the rock glacier habitat suitability (y-axis) when other variables are held constant at their average sample value.

Predicted Rock Glacier Distributions

The Maxent model described above was forced with pre-industrial covariates to predict rock glacier habitat suitability under pre-industrial climate equilibria, which is assumed to drive the present distribution of rock glaciers. This approach predicted approximately 27,400 km² of rock glacier habitat across the 437,000 km² modeling domain, with concentrations in the high elevation regions of the Rockies, the southeastern Sierra Nevada, and the eastern portion of the North Cascades (Table C.4; Figure 4.3a, 4.3d). The

areas of high predicted rock glacier suitability aligned well with known current rock glacier locations (Figure 4.1).

The rock glacier suitability predictions commensurate with present-day climate equilibria were largely similar to those for pre-industrial climate equilibria (Figure 4.3b). However, most locations that were suitable in the pre-industrial period saw a slight reduction in suitability when projected to the present day, resulting in a net reduction in suitable area of

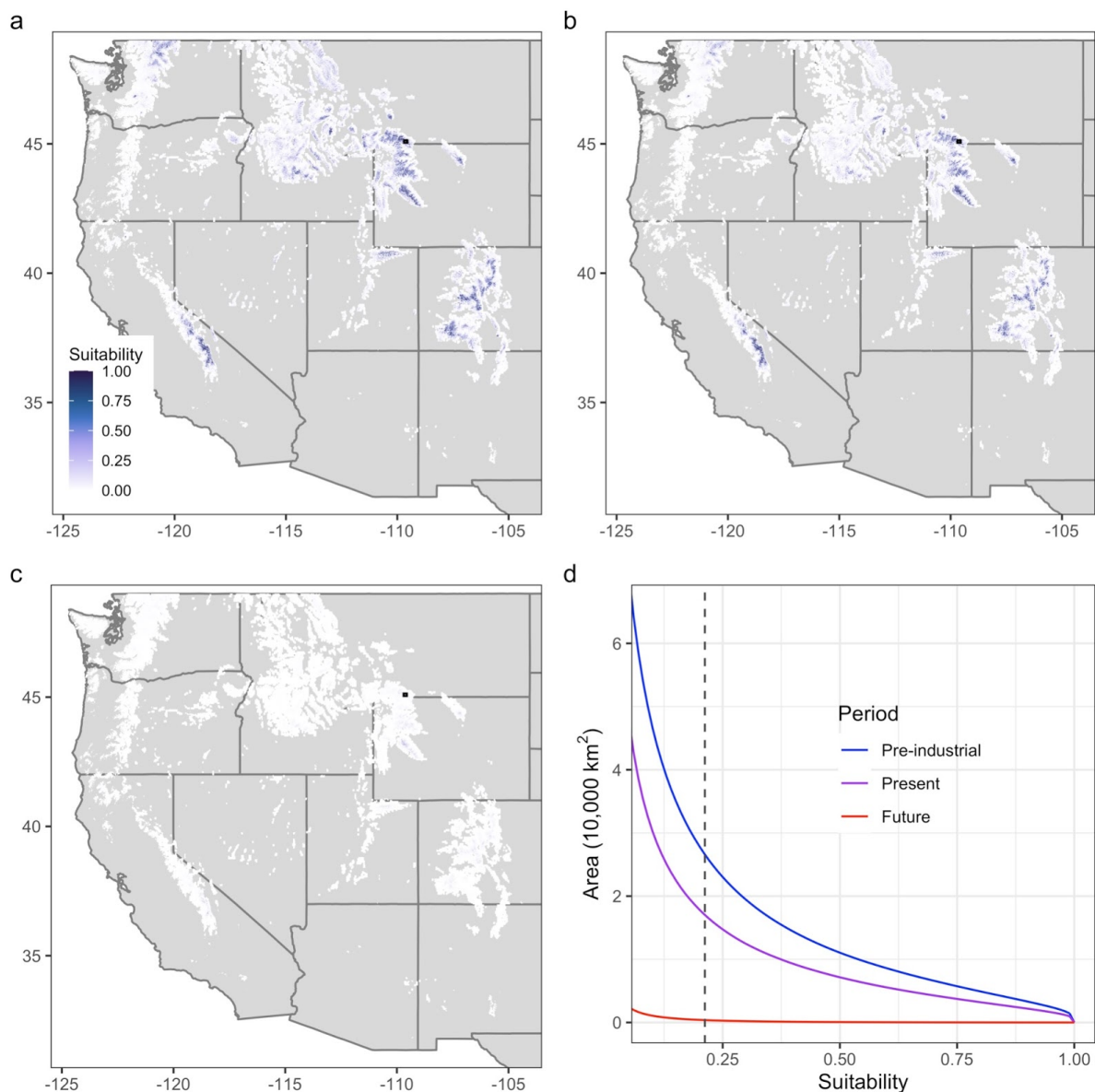


Figure 4.3 Predicted suitability for rock glaciers under pre-industrial (a), present (b), and future (c) conditions across the western U.S. The Beartooth Mountains, Montana domain used in subsequent analyses is marked by a black rectangle on the western U.S. maps. d) shows the area on the y-axis that exceeds the suitability level on the x-axis (starting at 0.1) for the three time periods. The dashed line in d) marks the suitability threshold used in subsequent analyses (0.212).

36% or 9,800 km², including 10% of known rock glacier locations (Table C.4). A few areas were predicted to have enhanced suitability (<0.1% of the domain), including high elevation portions of the Southern Sierra, Middle Rockies, and Southern Rockies. These locations were cooler, had more solar radiation, and were more focused on southern aspects relative to locations where habitat persisted or disappeared (Figure C.7). Locations where habitat persisted tended to be more focused on north aspects and have cooler temperatures than locations where habitat disappeared (Figure C.7).

Drastic reductions in rock glacier habitat were simulated using predictors representing future high-end warming conditions (Figure 4.3c). Relative to the present period, more than 98% (~17,300 km²) of suitable habitat was projected to disappear, including 90% of known rock glacier locations (Table C.4). The 0.1% of the domain projected to retain suitable habitat under the future climate was scattered in the Sierra Nevada, the Idaho Batholith, the Middle Rockies, the Wasatch and Uinta Mountains, and the Southern Rockies (Table C.4). These locations were cooler, more focused on north aspects, had larger headwall areas, and were at higher elevations than locations where suitability was projected to disappear (Figure C.8). Only 1 grid cell was predicted to have enhanced suitability in the future climate.

Glacier to Rock Glacier Transformation

To address our third research question, regarding glacier to rock glacier transformation, we evaluated the rock glacier suitability over time at locations presently occupied by glaciers. Present-day glaciers cover 729 km² of the modeling domain. During the pre-industrial period, 39.5% of this area was considered suitable for rock glaciers and the average rock glacier suitability at glaciated locations was 0.29. Suitable area declined to 29.0% in the present period and 4.1% in the future period, while average suitability in glaciated locations declined to 0.22 in the present period and 0.03 in the future period. Glaciated locations that retained suitable rock glacier habitat in the present period had cooler temperatures, less rain and snowfall, and were at higher elevations than locations that became unsuitable (Figure C.9). Rock glacier suitability increased between the pre-industrial and present periods at some glaciated locations in the Middle Rockies. These locations had cooler temperatures, more solar radiation, and were located at higher elevations, on lower slopes, and were less focused on north aspects (Figure C.9).

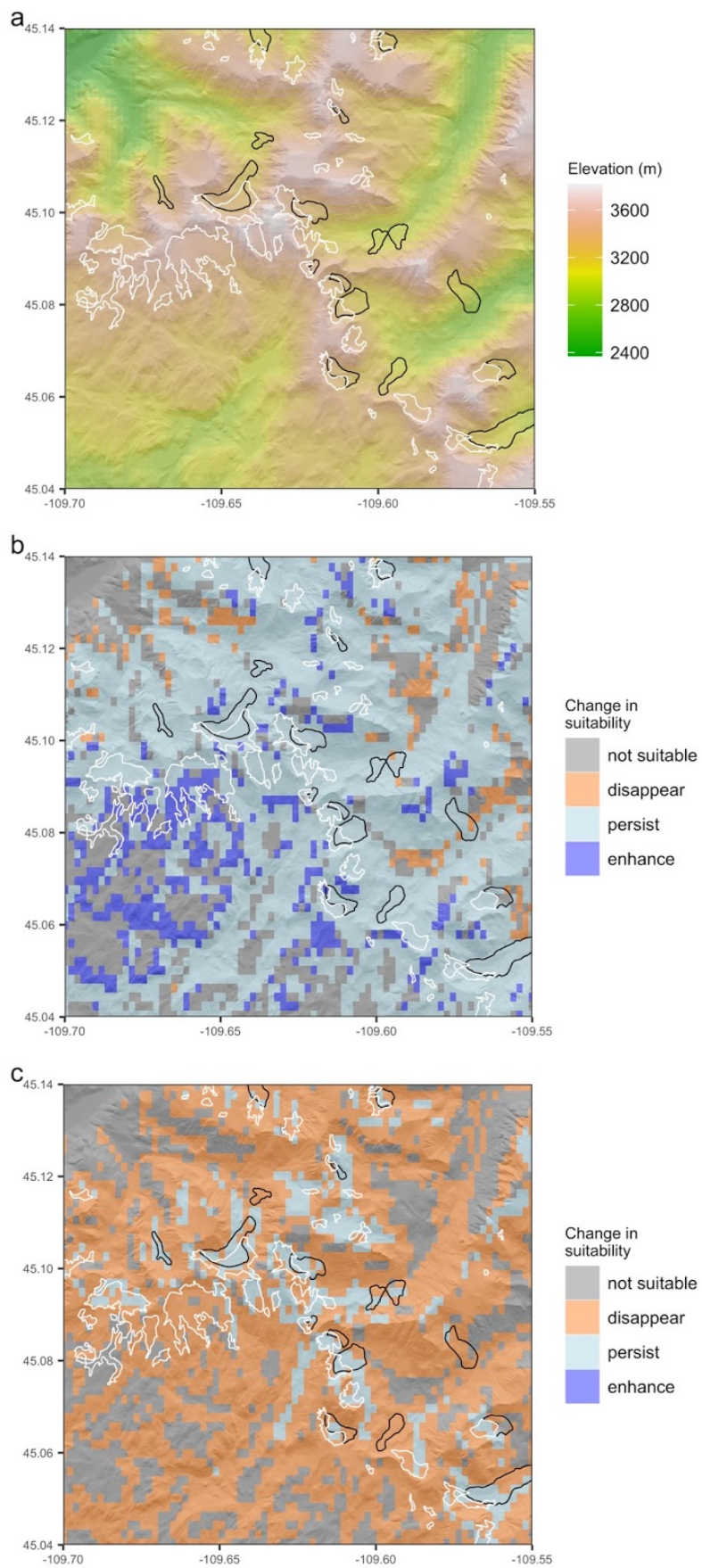


Figure 4.4 Changes in rock glacier habitat suitability over time in the Beartooth Mountains, Montana. Elevation of the terrain (a). Changes in rock glacier suitability between a) pre-industrial and present periods and b) present and future periods. Black and white outlines denote the locations of present-day rock glaciers and glaciers, respectively.

Between the present and future periods, there was a large reduction in rock glacier suitability at glaciated locations (Figure C.10). Relative to locations where suitability disappeared, locations where suitability persisted had cooler temperatures, less rain, more solar radiation, larger headwall areas, and were more concentrated on north aspects and at high elevations.

We illustrate some of these developments on a landscape scale using an area of the Beartooth Mountains, Montana (-109.7°W to -109.55°W, 45.05°N to 45.14°N; Figure 4.4a). Over this domain, the pre-industrial model predicted high rock glacier suitability in all of the known rock glacier locations, as well as some of the glacier locations (Figure C.11a). A small increase in suitable habitat was found under present climate equilibria (Figure 4.4b, C.11). Average suitability remained relatively constant at locations collocated with known rock glaciers, but increased from 0.67 to 0.78 at locations collocated with glaciers. Historically, glaciers in this region occupied locations at higher elevations, with smaller headwall areas and a wider range of slopes, with more rain and snowfall, and cooler temperatures relative to rock glacier locations, but under present climate temperatures at glacier locations became more similar to historical temperatures at rock glacier locations (Figure C.12). Locations with enhanced suitability, some of which corresponded with glacier locations, were cooler, at higher elevations, and on more south facing slopes (Figure 4.4b, C.13), similar to the patterns seen across the western U.S. domain (Figure C.7).

By the future period, the majority of rock glacier habitat in the Beartooth Mountains was projected to disappear, with only the highest elevations and mostly north facing slopes retaining habitat (Figure 4.4c, C.14). Both glacier and rock glacier locations saw substantial warming between the present and future periods, with corresponding increases in rainfall and decreases in snowfall (Figure C.12). Average suitability at rock glacier locations declined from 0.91 to 0.33, while at glacier locations it declined from 0.78 to 0.20.

Discussion and Conclusions

The Maxent model calibrated on pre-industrial covariates and current known rock glacier locations performed very well in both calibration and cross validation, maintaining AUC values > 0.9 in all cases (Table C.3). The model predicted $\sim 27,400$ km² of suitable habitat in the pre-industrial period, which is significantly greater than the estimated area of present rock glaciers (1000 km², Johnson et al., 2020), suggesting that the model predictions should be considered as potential, not actual, rock glacier habitat. The excellent cross validation performance and the diversity of conditions across the western U.S. suggest that the model may transfer well to locations outside of the modeling domain, including warmer novel climates.

Relationships between topographic and geologic covariates and rock glacier habitat suitability simulated by the model (Figure 4.2b) matched expectations based on the literature (Bolch & Gorbunov, 2014; Brazier et al., 1998; Charbonneau & Smith, 2018; Frauenfelder et al., 2003; Haeberli et al., 2006; Johnson et al., 2007; Kenner & Magnusson, 2017; Matsuoka & Ikeda, 2001; Wahrhaftig & Cox, 1959). Climatically, rock glaciers were more likely in areas with pre-industrial $t_{mean} < -1^{\circ}\text{C}$, which corresponds well with other estimates of rock glacier temperature niches based on present climate (Bolch & Gorbunov, 2014; Kenner & Magnusson, 2017). In terms of precipitation, rock glaciers were more likely in areas that received less than 400 mm/year of rain and between 500 and 1500 mm/year of sfe, which is comparable to previous estimates (Bolch & Gorbunov, 2014). Areas with low solar radiation had higher predicted suitability (Figure 4.2b, Johnson et al., 2007). Locations with temporally discontinuous snow cover were most suitable for rock glaciers as such conditions allow for cold air infiltration into the surface debris matrix (Haeberli et al., 2006), whereas snow-rich locations were less suitable for rock glaciers, similar to the findings of Kenner & Magnusson, (2017). Compared with previous efforts to understand controls on rock glacier spatial distributions, this work considered more functionally relevant covariates, a larger spatial extent, a larger sample of known rock glaciers, and a larger range of environmental conditions. These characteristics, in addition to several successful cross validations, lend confidence to the generalizability of the relationships we found between environmental covariates and rock glacier distributions.

This work provided the first estimates of future rock glacier spatial distributions. Relative to pre-industrial rock glacier habitat, habitat in equilibria with present-day climate showed moderate declines in suitability in most mountain ranges and some increases in suitability in high elevation areas and on equatorward aspects (Figure 4.3b, C.7). An additional 10% of known rock glaciers were considered unsuitable in the present climate, suggesting that they are currently in disequilibrium. In contrast, 99% of habitat that was suitable for rock glaciers under the pre-industrial climate became unsuitable in equilibria with future climate (Figure 4.3c, Table C.4). Remaining habitat was concentrated at the highest elevations and on poleward aspects (Figure C.8). These contrasting scenarios illustrate the potential for actions which limit climate warming to avoid the near complete loss of one element of the mountain cryosphere.

While snow and glaciers are expected to become increasingly focused on north facing slopes with minimal solar radiation (Barsugli et al., 2020; Florentine et al., 2018), rock glacier habitat was predicted to improve on some south facing slopes with high solar radiation under the present climate (Figures 4.4b, C.7, C.9, C.13). These sites were also some of the coldest and highest elevation sites. This finding aligns with previous work on current rock glacier distributions that shows that rock glaciers can exist on equatorward aspects with high solar radiation if they are sufficiently cold (Brenning & Azócar, 2009; Brenning & Trombotto, 2006). This can be explained by the fact that solar radiation warms the debris surface and the air above the rock glacier, but due to air density differences the warm air is unlikely to infiltrate the debris matrix and thus warming is limited to conduction through the debris matrix, which is minimal (Haeberli et al., 2006). However, these high radiation sites only maintained habitat through the present period; under the future scenario, rock glacier habitat became increasingly focused on poleward aspects and at high elevations (Figure 4.4c, C.8, C.10, C.14), similar to expectations for snow and glaciers.

We found limited potential for glacier to rock glacier transformation in the western U.S. Presently glaciated areas that were suitable for rock glaciers in the present climate were particularly cold, high elevation sites that received < 1500 mm of sfe (Figure C.9) and were scattered across western U.S. mountains. Under the future scenario, presently glaciated areas with suitable rock glacier habitat were largely restricted to the southern Sierra Nevada and Middle Rockies. Case studies of glacier to rock glacier transformations in the central Andes

showed that this transformation can occur over the course of decades (Monnier & Kinnard, 2015, 2016). Along with other studies, they highlighted the importance of topoclimatic conditions and specifically a reduction in the ratio of ice supply to debris supply (Anderson et al., 2018; Knight et al., 2019). Glacier ice volume in the western U.S. has declined and is projected to continue declining through the 21st century (Frans et al., 2018; Radić et al., 2014). However, the largest glaciers (concentrated in Oregon and Washington) tend to be in locations that receive the most precipitation and snowfall but have the smallest headwall areas, and vice versa. Therefore, we hypothesize that many western U.S. glaciers in wetter locations will not transition to rock glaciers because the reduction in ice supply necessary to achieve a suitable ice to debris ratio would require a large reduction in the snowfall to rainfall ratio and be associated with a large increase in rainfall which is unsuitable for rock glaciers. This aligns with work based on observations of currently transitioning landforms, which suggested that debris supply may determine which glaciers transition to rock glaciers and which do not (Jones et al., 2019).

Sources of uncertainty in our estimates of rock glacier distributions and their environmental controls include uncertainties in the rock glacier inventory (Brardinoni et al., 2019), the spatial scale of the covariates (especially in the case of terrain metrics; Deng et al., 2007), missing or poorly captured processes such as snow redistribution, uncertainties in the downscaled climate data, the model formulation (e.g., beta parameter, feature classes, and covariate selection; Convertino et al., 2014), the suitability threshold (Liu et al., 2016), and differential response times of rock glaciers to climate forcing (Knight et al., 2019). Predicting future rock glacier distributions introduces additional uncertainties regarding the stationarity of modeled relationships between covariates and rock glaciers as well as uncertainties in the future climate data stemming from climate models and scenarios. Model development steps including assessment of collinearity and optimal model complexity have alleviated some of these concerns, but these results remain one possible estimate of rock glacier habitat. Specifically, the assumption that current rock glaciers are a reflection of pre-industrial hydroclimatic conditions may overestimate or underestimate rock glacier decline for rock glaciers that have equilibrated to more or less recent conditions, respectively. Future work should quantify these sources of uncertainty and their effects on predicted rock glacier habitat. While the chosen covariates did an excellent job of predicting current rock glacier

habitat in calibration and cross validation, future work could incorporate more process-relevant predictors such as a refined metric of headwall area (Janke & Frauenfelder, 2008), some measure of fracturing propensity (Chueca, 1992), and a metric of snow redistribution via wind and avalanching (Kenner & Magnusson, 2017). Evaluation of changes in glaciers and rock glaciers using remote sensing and field investigations would provide a useful secondary line of evidence.

The impacts of the loss of active rock glaciers in the western U.S. will likely be felt most at local scales and in semi-arid regions. Beyond their intrinsic value as features of the mountain landscape, rock glaciers support greater plant, arthropod, and bacterial diversity than nearby landscapes (Fegel et al., 2016; Franklin, 2012; Millar et al., 2015) and provide potential climate refugia for pika and cold-adapted fish (Harrington et al., 2017; Millar & Westfall, 2019). Equilibration to future climate, and the transition from active to inactive or relict, may take hundreds to thousands of years (Müller et al., 2016) during which time rock glaciers may continue to provide these services as well as increased contributions to streamflow in semi-arid watersheds (Brighenti et al., 2019; Harrington et al., 2018; Wagner et al., 2016). However, under the high warming scenario considered here, rock glaciers, like snow and glaciers, are likely to eventually disappear from the landscape. In contrast, stabilizing climate at today's temperatures will largely preserve active rock glaciers in this region.

References

- Akaike, H. (1974). A new look at the statistical model identification. *IEEE Transactions on Automatic Control*, *19*(6), 716–723. <https://doi.org/10.1109/TAC.1974.1100705>
- Anderson, R. S., Anderson, L. S., Armstrong, W. H., Rossi, M. W., & Crump, S. E. (2018). Glaciation of alpine valleys: The glacier – debris-covered glacier – rock glacier continuum. *Geomorphology*, *311*, 127–142. <https://doi.org/10.1016/j.geomorph.2018.03.015>
- Anning, D. W., & Ator, S. W. (2017). *Generalized lithology of the conterminous United States* [Data set]. U.S. Geological Survey. <https://doi.org/10.5066/F7R78D4N>

- Austin, M. P. (2002). Spatial prediction of species distribution: An interface between ecological theory and statistical modelling. *Ecological Modelling*, *157*(2–3), 101–118. [https://doi.org/10.1016/S0304-3800\(02\)00205-3](https://doi.org/10.1016/S0304-3800(02)00205-3)
- Barsugli, J. J., Ray, A. J., Livneh, B., Dewes, C. F., Heldmyer, A., Rangwala, I., Guinotte, J. M., & Torbit, S. (2020). Projections of Mountain Snowpack Loss for Wolverine Denning Elevations in the Rocky Mountains. *Earth's Future*, *8*(10). <https://doi.org/10.1029/2020EF001537>
- Bolch, T., & Gorbunov, A. P. (2014). Characteristics and Origin of Rock Glaciers in Northern Tien Shan (Kazakhstan/Kyrgyzstan). *Permafrost and Periglacial Processes*, *25*(4), 320–332. <https://doi.org/10.1002/ppp.1825>
- Brardinoni, F., Scotti, R., Sailer, R., & Mair, V. (2019). Evaluating sources of uncertainty and variability in rock glacier inventories. *Earth Surface Processes and Landforms*, *44*(12), 2450–2466. <https://doi.org/10.1002/esp.4674>
- Brazier, V., Kirkbride, M. P., & Owens, I. F. (1998). The relationship between climate and rock glacier distribution in the Ben Ohau Range, New Zealand. *Geografiska Annaler: Series A, Physical Geography*, *80*(3-4), 193–207. <https://doi.org/10.1111/j.0435-3676.1998.00037.x>
- Brenning, A., & Azócar, G. F. (2009). Statistical analysis of topographic and climatic controls and multispectral signatures of rock glaciers in the dry Andes, Chile (27°–33°S). *Permafrost and Periglacial Processes*, *21*(1), 54–66. <https://doi.org/10.1002/ppp.670>
- Brenning, A., & Azócar, G. F. (2010). Statistical analysis of topographic and climatic controls and multispectral signatures of rock glaciers in the dry Andes, Chile (27°–33°S). *Permafrost and Periglacial Processes*, *21*(1), 54–66. <https://doi.org/10.1002/ppp.670>
- Brenning, A., & Trombotto, D. (2006). Logistic regression modeling of rock glacier and glacier distribution: Topographic and climatic controls in the semi-arid Andes. *Geomorphology*, *81*(1–2), 141–154.
- Brighenti, S., Tolotti, M., Bruno, M. C., Wharton, G., Pusch, M. T., & Bertoldi, W. (2019). Ecosystem shifts in Alpine streams under glacier retreat and rock glacier thaw: A

- review. *Science of The Total Environment*, 675, 542–559.
<https://doi.org/10.1016/j.scitotenv.2019.04.221>
- Charbonneau, A. A., & Smith, D. J. (2018). An inventory of rock glaciers in the central British Columbia Coast Mountains, Canada, from high resolution Google Earth imagery. *Arctic, Antarctic, and Alpine Research*, 50(1), e1489026.
<https://doi.org/10.1080/15230430.2018.1489026>
- Chueca, J. (1992). A statistical analysis of the spatial distribution of rock glaciers, Spanish Central Pyrenees. *Permafrost and Periglacial Processes*, 3(3), 261–265.
<https://doi.org/10.1002/ppp.3430030316>
- Comino, E., Fiorucci, A., Rosso, M., Terenziani, A., & Treves, A. (2021). Vegetation and Glacier Trends in the Area of the Maritime Alps Natural Park (Italy): MaxEnt Application to Predict Habitat Development. *Climate*, 9(4), 54.
<https://doi.org/10.3390/cli9040054>
- Convertino, M., Muñoz-Carpena, R., Chu-Agor, M. L., Kiker, G. A., & Linkov, I. (2014). Untangling drivers of species distributions: Global sensitivity and uncertainty analyses of MaxEnt. *Environmental Modelling & Software*, 51, 296–309.
<https://doi.org/10.1016/j.envsoft.2013.10.001>
- Delaloye, R., Lambiel, C., & Gärtner-Roer, I. (2010). Overview of rock glacier kinematics research in the Swiss Alps: Seasonal rhythm, interannual variations and trends over several decades. *Geographica Helvetica*, 65(2), 135–145.
<https://doi.org/info:doi/10.5167/uzh-38562>
- Deng, Y., Wilson, J. P., & Bauer, B. O. (2007). DEM resolution dependencies of terrain attributes across a landscape. *International Journal of Geographical Information Science*, 21(2), 187–213. <https://doi.org/10.1080/13658810600894364>
- Duque-Lazo, J., van Gils, H., Groen, T. A., & Navarro-Cerrillo, R. M. (2016). Transferability of species distribution models: The case of *Phytophthora cinnamomi* in Southwest Spain and Southwest Australia. *Ecological Modelling*, 320, 62–70.
<https://doi.org/10.1016/j.ecolmodel.2015.09.019>
- Elith, J., H. Graham, C., P. Anderson, R., Dudík, M., Ferrier, S., Guisan, A., J. Hijmans, R., Huettmann, F., R. Leathwick, J., Lehmann, A., Li, J., G. Lohmann, L., A. Loiselle, B., Manion, G., Moritz, C., Nakamura, M., Nakazawa, Y., McC. M. Overton, J.,

- Townsend Peterson, A., ... E. Zimmermann, N. (2006). Novel methods improve prediction of species' distributions from occurrence data. *Ecography*, 29(2), 129–151. <https://doi.org/10.1111/j.2006.0906-7590.04596.x>
- Fegel, T. S., Baron, J. S., Fountain, A. G., Johnson, G. F., & Hall, E. K. (2016). The differing biogeochemical and microbial signatures of glaciers and rock glaciers. *Journal of Geophysical Research: Biogeosciences*, 121(3), 919–932. <https://doi.org/10.1002/2015JG003236>
- Florentine, C., Harper, J., Fagre, D., Moore, J., & Peitzsch, E. (2018). Local topography increasingly influences the mass balance of a retreating cirque glacier. *The Cryosphere*, 12(6), 2109–2122. <https://doi.org/10.5194/tc-12-2109-2018>
- Fountain, A. G. (2006). *GLIMS Glacier Database* [Data set]. National Snow and Ice Data Center. <http://dx.doi.org/10.7265/N5V98602>
- Fountain, A. G., Glenn, B., & Basagic IV, H. J. (2017). The Geography of Glaciers and Perennial Snowfields in the American West. *Arctic, Antarctic, and Alpine Research*, 49(3), 391–410. <https://doi.org/10.1657/AAAR0017-003>
- Franklin, R. S. (2012). *Climatic and Ecological Implications of Shrub-Chronologies at Rock Glacier Sites of the Eastern Sierra Nevada Range, California, U.S.A.* [Dissertation, University of Arizona]. <https://repository.arizona.edu/handle/10150/242393>
- Frans, C., Istanbuluoglu, E., Lettenmaier, D. P., Fountain, A. G., & Riedel, J. (2018). Glacier Recession and the Response of Summer Streamflow in the Pacific Northwest United States, 1960-2099. *Water Resources Research*. <https://doi.org/10.1029/2017WR021764>
- Frauenfelder, R., Haeberli, W., & Hoelzle, M. (2003). Rockglacier occurrence and related terrain parameters in a study area of the Eastern Swiss Alps. *Proceedings of the Eighth International Permafrost Conference on Permafrost*, 253–258.
- Gesch, D. B., Evans, G. A., Oimoen, M. J., & Arundel, S. (2018). *The National Elevation Dataset* (pp. 83–110). American Society for Photogrammetry and Remote Sensing; USGS Publications Warehouse. <http://pubs.er.usgs.gov/publication/70201572>
- Haeberli, W., Hallet, B., Arenson, L., Elconin, R., Humlum, O., Käab, A., Kaufmann, V., Ladanyi, B., Matsuoka, N., Springman, S., & Mühlh, D. V. (2006). Permafrost creep

- and rock glacier dynamics. *Permafrost and Periglacial Processes*, 17(3), 189–214. <https://doi.org/10.1002/ppp.561>
- Harrington, J. S., Hayashi, M., & Kurylyk, B. L. (2017). Influence of a rock glacier spring on the stream energy budget and cold-water refuge in an alpine stream. *Hydrological Processes*, 31(26), 4719–4733. <https://doi.org/10.1002/hyp.11391>
- Harrington, J. S., Mozil, A., Hayashi, M., & Bentley, L. R. (2018). Groundwater flow and storage processes in an inactive rock glacier. *Hydrological Processes*, 32(20), 3070–3088. <https://doi.org/10.1002/hyp.13248>
- Hijmans, R. J., Phillips, S., Leathwick, J., & Elith, J. (2020). *Dismo: Species Distribution Modeling. R package version 1.3-3*. (1.3-3) [Computer software]. <https://CRAN.R-project.org/package=dismo>
- Hoffman, M., & Fountain, A. G. (2016). *GLIMS Glacier Database* [Data set]. National Snow and Ice Data Center. <http://dx.doi.org/10.7265/N5V98602>
- Huggel, C., Carey, M., Clague, J. J., & Kaab, A. (Eds.). (2015). *The High-Mountain Cryosphere: Environmental Changes and Human Risks*. Cambridge University Press. <https://doi.org/10.1017/CBO9781107588653>
- Huss, M., Bookhagen, B., Huggel, C., Jacobsen, D., Bradley, R. S., Clague, J. J., Vuille, M., Buytaert, W., Cayan, D. R., Greenwood, G., Mark, B. G., Milner, A. M., Weingartner, R., & Winder, M. (2017). Toward mountains without permanent snow and ice. *Earth's Future*, 5(5), 2016EF000514. <https://doi.org/10.1002/2016EF000514>
- Janke, J., & Frauenfelder, R. (2008). The relationship between rock glacier and contributing area parameters in the Front Range of Colorado. *Journal of Quaternary Science*, 23(2), 153–163. <https://doi.org/10.1002/jqs.1133>
- Johnson, B. G., Thackray, G. D., & Van Kirk, R. (2007). The effect of topography, latitude, and lithology on rock glacier distribution in the Lemhi Range, central Idaho, USA. *Geomorphology*, 91(1), 38–50. <https://doi.org/10.1016/j.geomorph.2007.01.023>
- Johnson, G., Chang, H., & Fountain, A. (2020). Rock glaciers of the contiguous United States: GIS inventory and spatial distribution patterns [Preprint]. *Earth Systems Science Datasets*. <https://doi.org/10.5194/essd-2020-158>

- Jones, D. B., Harrison, S., & Anderson, K. (2019). Mountain glacier-to-rock glacier transition. *Global and Planetary Change*, *181*, 102999. <https://doi.org/10.1016/j.gloplacha.2019.102999>
- Jones, D. B., Harrison, S., Anderson, K., & Betts, R. A. (2018). Mountain rock glaciers contain globally significant water stores. *Scientific Reports*, *8*(1), 2834. <https://doi.org/10.1038/s41598-018-21244-w>
- Kääb, A., Chiarle, M., Raup, B., & Schneider, C. (2007). Climate change impacts on mountain glaciers and permafrost. *Global and Planetary Change*, *56*(1–2), vii–ix. <https://doi.org/10.1016/j.gloplacha.2006.07.008>
- Kass, J. M., Muscarella, R., Galante, P. J., Bohl, C. L., Pinilla-Buitrago, G. E., Boria, R. A., Soley-Guardia, M., & Anderson, R. P. (2021). ENMeval 2.0: Redesigned for customizable and reproducible modeling of species' niches and distributions. *Methods in Ecology and Evolution*, 2041–210X.13628. <https://doi.org/10.1111/2041-210X.13628>
- Kenner, R., & Magnusson, J. (2017). Estimating the Effect of Different Influencing Factors on Rock Glacier Development in Two Regions in the Swiss Alps: Effects of different influencing factors on rock glacier development. *Permafrost and Periglacial Processes*, *28*(1), 195–208. <https://doi.org/10.1002/ppp.1910>
- Knight, J., Harrison, S., & Jones, D. B. (2019). Rock glaciers and the geomorphological evolution of deglaciating mountains. *Geomorphology*, *324*, 14–24. <https://doi.org/10.1016/j.geomorph.2018.09.020>
- Körner, C., Paulsen, J., & Spehn, E. M. (2011). A definition of mountains and their bioclimatic belts for global comparisons of biodiversity data. *Alpine Botany*, *121*(2). <https://doi.org/10.1007/s00035-011-0094-4>
- Liu, C., Ikeda, K., Rasmussen, R., Barlage, M., Newman, A. J., Prein, A. F., Chen, F., Chen, L., Clark, M., Dai, A., Dudhia, J., Eidhammer, T., Gochis, D., Gutmann, E., Kurkute, S., Li, Y., Thompson, G., & Yates, D. (2017). Continental-scale convection-permitting modeling of the current and future climate of North America. *Climate Dynamics*, *49*(1–2), 71–95. <https://doi.org/10.1007/s00382-016-3327-9>

- Liu, C., Newell, G., & White, M. (2016). On the selection of thresholds for predicting species occurrence with presence-only data. *Ecology and Evolution*, 6(1), 337–348.
<https://doi.org/10.1002/ece3.1878>
- Lute, A.C., Abatzoglou, J.T. & Link, T. (2021). SnowClim: high-resolution snow model and data for the western United States. *Manuscript in preparation*.
- Manquehual-Cheuque, F., & Somos-Valenzuela, M. (2021). Climate change refugia for glaciers in Patagonia. *Anthropocene*, 33, 100277.
<https://doi.org/10.1016/j.ancene.2020.100277>
- Marcet, M., Cicoira, A., Cusicanqui, D., Bodin, X., Echelard, T., Obregon, R., & Schoeneich, P. (2021). Rock glaciers throughout the French Alps accelerated and destabilised since 1990 as air temperatures increased. *Communications Earth & Environment*, 2(1), 81. <https://doi.org/10.1038/s43247-021-00150-6>
- Matsuoka, N., & Ikeda, A. (2001). Geological control on the distribution and characteristics of talus-derived rock glaciers. *Annual Report, Institute of Geoscience, University of Tsukuba*, no 27, pp 11-16.
- Millar, C. I., & Westfall, R. D. (2019). Geographic, hydrological, and climatic significance of rock glaciers in the Great Basin, USA. *Arctic, Antarctic, and Alpine Research*, 51(1), 232–249. <https://doi.org/10.1080/15230430.2019.1618666>
- Millar, C., & Westfall, R. (2008). Rock glaciers and related periglacial landforms in the Sierra Nevada, CA, USA; inventory, distribution and climatic relationships. *Quaternary International*, 188(1), 90–104.
<https://doi.org/10.1016/j.quaint.2007.06.004>
- Millar, C., Westfall, R. D., Evenden, A., Holmquist, J. G., Schmidt-Gengenbach, J., Franklin, R. S., Nachlinger, J., & Delany, D. (2015). Potential climatic refugia in semi-arid, temperate mountains: Plant and arthropod assemblages associated with rock glaciers, talus slopes, and their forefield wetlands, Sierra Nevada, California, USA. *Quaternary International*, 387, 106–121. <https://doi.org/10.1016/j.quaint.2013.11.003>
- Monnier, S., & Kinnard, C. (2015). Reconsidering the glacier to rock glacier transformation problem: New insights from the central Andes of Chile. *Geomorphology*, 238, 47–55.
<https://doi.org/10.1016/j.geomorph.2015.02.025>

- Monnier, S., & Kinnard, C. (2016). Pluri-decadal (1955-2014) evolution of glacier-rock glacier transitional landforms in the central Andes of Chile (30-33 S). *Earth Surface Dynamics Discussions*, 1–35. <https://doi.org/10.5194/esurf-2016-16>
- Moore, R. D., Fleming, S. W., Menounos, B., Wheate, R., Fountain, A., Stahl, K., Holm, K., & Jakob, M. (2009). Glacier change in western North America: Influences on hydrology, geomorphic hazards and water quality. *Hydrological Processes*, 23(1), 42–61. <https://doi.org/10.1002/hyp.7162>
- Morris, S. (1981). Topoclimatic Factors and the Development of Rock Glacier Facies, Sangre de Cristo Mountains, Southern Colorado. *Arctic and Alpine Research*, 13(3), 329–338.
- Mote, P. W., Li, S., Lettenmaier, D. P., Xiao, M., & Engel, R. (2018). Dramatic declines in snowpack in the western US. *Npj Climate and Atmospheric Science*, 1(1). <https://doi.org/10.1038/s41612-018-0012-1>
- Müller, J., Vieli, A., & Gärtner-Roer, I. (2016). Rockglaciers on the run- Understanding rockglacier landform evolution and recent changes from numerical flow modeling. *The Cryosphere Discussions*, 1–40. <https://doi.org/10.5194/tc-2016-35>
- Phillips, S. J., Anderson, R. P., & Schapire, R. E. (2006). Maximum entropy modeling of species geographic distributions. *Ecological Modelling*, 190(3), 231–259. <https://doi.org/10.1016/j.ecolmodel.2005.03.026>
- Phillips, S. J., & Dudík, M. (2008). Modeling of species distributions with Maxent: New extensions and a comprehensive evaluation. *Ecography*, 31(2), 161–175. <https://doi.org/10.1111/j.0906-7590.2008.5203.x>
- R Core Team. (2020). *R: A language and environment for statistical computing*. R Foundation for Statistical Computing. <https://www.R-project.org/>
- Radić, V., Bliss, A., Beedlow, A. C., Hock, R., Miles, E., & Cogley, J. G. (2014). Regional and global projections of twenty-first century glacier mass changes in response to climate scenarios from global climate models. *Climate Dynamics*, 42(1–2), 37–58. <https://doi.org/10.1007/s00382-013-1719-7>
- Sevestre, H., & Benn, D. I. (2015). Climatic and geometric controls on the global distribution of surge-type glaciers: Implications for a unifying model of surging. *Journal of Glaciology*, 61(228), 646–662. <https://doi.org/10.3189/2015JoG14J136>

- Taylor, K. E., Stouffer, R. J., & Meehl, G. A. (2012). An Overview of CMIP5 and the Experiment Design. *Bulletin of the American Meteorological Society*, 93(4), 485–498. <https://doi.org/10.1175/BAMS-D-11-00094.1>
- Trcka, A. (2020). *Inventory of Rock Glaciers in the American West and Their Topography and Climate* [Thesis, Portland State University]. <https://doi.org/10.15760/etd.7509>
- US Environmental Protection Agency. (2013). *Level III Ecoregions of the Conterminous United States* [Data set]. US EPA Office of Research and Development (ORD) - National Health and Environmental Effects Research Laboratory (NHEERL). ftp://ftp.epa.gov/wed/ecoregions/us/usl3_no_st.zip
- Valavi, R., Elith, J., Lahoz-Monfort, J. J., & Guillera-Arroita, G. (2019). BlockCV: An R package for generating spatially or environmentally separated folds for k-fold cross-validation of species distribution models. *Methods in Ecology and Evolution*, 10(2), 225–232. <https://doi.org/10.1111/2041-210X.13107>
- Wagner, T., Pauritsch, M., & Winkler, G. (2016). Impact of relict rock glaciers on spring and stream flow of alpine watersheds: Examples of the Niedere Tauern Range, Eastern Alps (Austria). *Austrian Journal of Earth Sciences*, 109(1). <https://doi.org/10.17738/ajes.2016.0006>
- Wahrhaftig, C., & Cox, A. (1959). Rock Glaciers in the Alaska Range. *GSA Bulletin*, 70(4), 383–436. [https://doi.org/10.1130/0016-7606\(1959\)70\[383:RGITAR\]2.0.CO;2](https://doi.org/10.1130/0016-7606(1959)70[383:RGITAR]2.0.CO;2)
- Wang, T., Zhang, Z., Liu, L., Li, Z., Wang, P., Xu, L., Zhao, G., Tian, H., Kang, Z., Chen, H., & Zhang, X. (2021). Simulation of the Potential Distribution of the Glacier Based on Maximum Entropy Model in the Tianshan Mountains, China. *Water*, 13(11), 1541. <https://doi.org/10.3390/w13111541>

Chapter 5: Conclusion

In a nutshell, this work uses innovative approaches to data and computational constraints to enhance the physical realism of environmental models in the context of topographic complexity and climate change. Outcomes of this work include scientific findings, tools, and datasets that will benefit science and society more broadly. Below, I highlight the broader impacts of this research and suggest areas for future work.

In the first study, I showed how sparse temperature observations can be best used to calculate temperature lapse rates, which allow the estimation of air temperature across gridded, high-resolution domains. This work enhanced the utility of these observations by accounting for topoclimatic variability and quantifying sources of error and uncertainty. The best practices we developed for lapse rate estimation have the potential for broad scale impact by improving the accuracy of environmental models, statistical downscaling routines, and assessments of elevation dependent warming.

Additional work is needed to better constrain lapse rates for daily minimum air temperatures which are subject to more frequent inversions than daily maximum air temperatures and to better understand the variability of lapse rates across both spatial and temporal scales. An assessment of elevation dependent warming using observational data and best practices for lapse rate estimation would complement existing studies based on model outputs.

In the second study, I developed a novel hybrid snow model that emphasizes fidelity to physics and computational efficiency. A basis in physics is key to capturing differences in snowpack across complex terrain and to simulating its response to ongoing climate change, however physics-based models are typically too expensive to run at high resolution (<1 km) across large (subcontinental or larger) domains. The hybrid approach I developed retains the most important element of physics-based models while incorporating empirical parameterizations to enhance efficiency. I also created high-resolution climate forcing data that incorporates the effects of topographic complexity through elevation adjustments and correction of solar radiation for aspect, self-shading, and shading by adjacent terrain. These traits are key to understanding the current and future mountain snowpack since snowpack is likely to have differential sensitivities across terrain (e.g., aspect). The SnowClim model will

enable others to run high-resolution, physics-based simulations of snow in other contexts. The SnowClim dataset, consisting of climatologies of important climate and snow metrics for three time periods, will enable unprecedented assessment of changing snowpack in the Western U.S. and its implications for wildlife, agriculture, water resources, and other applications.

Future work regarding the SnowClim model could include incorporation of additional or more sophisticated processes, further evaluation of model uncertainty, and more thorough evaluation of model outputs. Specifically, it should be investigated whether more sophisticated representations of snow surface temperature and ground heat flux substantially improve simulations. In its current form, the model neglects some important processes such as sublimation by blowing snow, snow redistribution by wind and gravity, the effects of vegetation, and the effects of impurities such as dust and black carbon on snow albedo. In terms of model uncertainty, more work is needed to understand whether calibration at SNOTEL sites, which are typically in forest clearings, may bias the calibration by selecting parameters that compensate for the lack of vegetation effects in the model. Connecting this work to the previous chapter, it would be interesting to compare the current model outputs with those based on temperature data downscaled with a constant lapse rate in order to further document the importance of air temperature lapse rates in environmental modeling. More thorough evaluation of model outputs is needed to better understand differential snowpack sensitivities as a function of terrain properties such as aspect and elevation. Furthermore, this work would benefit from spatial comparison with an independent dataset of high-resolution snowpack observations. More broadly, this work highlighted the need for more observations of snowpack sublimation and cold content in order to validate energy and mass fluxes in snow models. These elements are key to accurately simulating the partitioning of snow lost to the air versus surface and groundwater and to simulating snowmelt timing. With additional observations of cold content, future work should further investigate empirical parameterizations for cold content in single layer models given the potential to improve physical realism while limiting computational cost.

In the third study, we sought to understand the current and future distribution of rock glaciers in the Western U.S. A physics-based modeling approach was not feasible in this case due to the limited observations of rock glacier internal compositions and debris

characterizations. To maximize the utility of the available data, we used a machine learning approach from the species distribution modeling literature. Recognizing the importance of fine resolution topoclimate to rock glaciers, we sourced high-resolution topographic, geologic, and hydroclimatic information. The use of high spatial resolution, physically relevant predictors enhanced the physical basis of the modeling approach and helped to account for the effects of topographic complexity. This work highlights the utility of machine learning approaches when necessary data for more physics-based approaches are unavailable. This approach enabled novel large-scale predictions of future rock glacier distributions, which are important for understanding semi-arid alpine ecosystems in a changing climate. This approach also generated insights regarding shifting rock glacier habitat suitability on the landscape and environmental prerequisites for glacier to rock glacier transformation that have not been achieved with previous approaches. Modeled suitabilities may also inform reassessment of rock glacier status at known rock glaciers with low modeled suitability and creation of new rock glacier inventories in previously unsurveyed areas.

Future work with this model should include more thorough assessments of glacier to rock glacier transformation potential. Specifically, more work is needed to understand what distinguishes glacier habitat from rock glacier habitat and what makes some glacier habitat suitable for transitioning to rock glaciers under a warming climate but other glacier habitat not suitable for this transition. In this vein, more thought should be given to the evolution of terrain parameters during glaciation and deglaciation and how this sets the stage for rock glacier development. Given that observed glacier to rock glacier transformations have occurred over the course of decades, glaciated locations with high modeled potential for transformation to rock glaciers should be investigated and subject to ongoing monitoring using time series of remotely sensed imagery. These efforts could help constrain the global potential for glacier to rock glacier transformation, informing adaptation measures in mountain environments. This work would benefit from quantification of uncertainty stemming from choice of equilibrium time period, model parameters, environmental variables, future climate scenarios, spatial resolution, and modeling approach. Broadly speaking, much remains unknown about rock glaciers. Detailed geophysical investigations are needed to better understand rock glacier genesis and evolution in past climates, internal composition, activity level, and degree of climate equilibrium on broad scales.

In sum, this work has improved our understanding of mountain environments in a variety of ways, including enabling more accurate assessments of elevation dependent warming, improving understanding of changes in snow in past and future climates, and providing a first estimate of future rock glacier distributions. This work developed and applied novel modeling approaches in order to push the limits of data and computational constraints, opening up new territory for future work. Through an emphasis on topographic complexity, this work documented ways to improve temperature lapse rates, found differential climate sensitivities of snow as a function of aspect, and increased the physical realism of a machine learning approach. The tools and datasets developed in this research will enable continued progress toward a more comprehensive understanding of current and future mountain environments.

Appendix A - Best Practices for Estimating Near-Surface Temperature Lapse Rates

Synthetic datasets covariates

Elevation

Elevation (*elev*) values were drawn from a random uniform distribution between 500 and 3500m. The effect of *elev* on temperature was estimated via simple linear regression based on a sea level temperature (y-intercept) of 25°C and the prescribed lapse rate of -6.5°C/km.

$$T_{elev} = 25^{\circ}C + -6.5^{\circ}C/km \times elev/1000$$

Equation A.1

Solar Radiation

Solar radiation (*srad*) values were initially drawn from a random normal distribution with mean 175 W/m² and standard deviation 70 W/m². Then *srad* values were made orthogonal to *elev* values using QR-decomposition, scaled, and perturbed by a function of *elev* to match the desired collinearity level ($r = 0.0, 0.3, \text{ or } 0.6$). Finally, *srad* values were rescaled, resulting in a quasi-random normal distribution of values of mean 175 W/m², standard deviation 70 W/m², and the prescribed collinearity.

T_{srad} was calculated as a linear function of solar radiation:

$$T_{srad} = \frac{srad}{100 \text{ W/m}^2/^{\circ}C} - 1.75 \text{ W/m}^2/^{\circ}C$$

Equation A.2

Distance from coast

Similar to *srad*, distance from coast (*coast*) values were drawn from a random normal distribution with mean 150 km and standard deviation 50 km in such a way that the correlation with *elev* was 0. T_{coast} was calculated as a simple nonlinear function of distance from coast:

$$T_{coast} = \frac{coast^2}{20000 \text{ km}^2/^{\circ}C} - 1.125 \text{ km}^2/^{\circ}C$$

Equation A.3

Random error

The error term was drawn randomly from a normal distribution with mean of 0 and varying standard deviation (0.1°C, 1°C, or 2°C) and in such a way that the correlation with *elev* was 0.

Observational station data covariates

A suite of topoclimatic covariates was calculated for each observational station as described below. Correlations between the covariates and temperature are shown in Figure A.1.

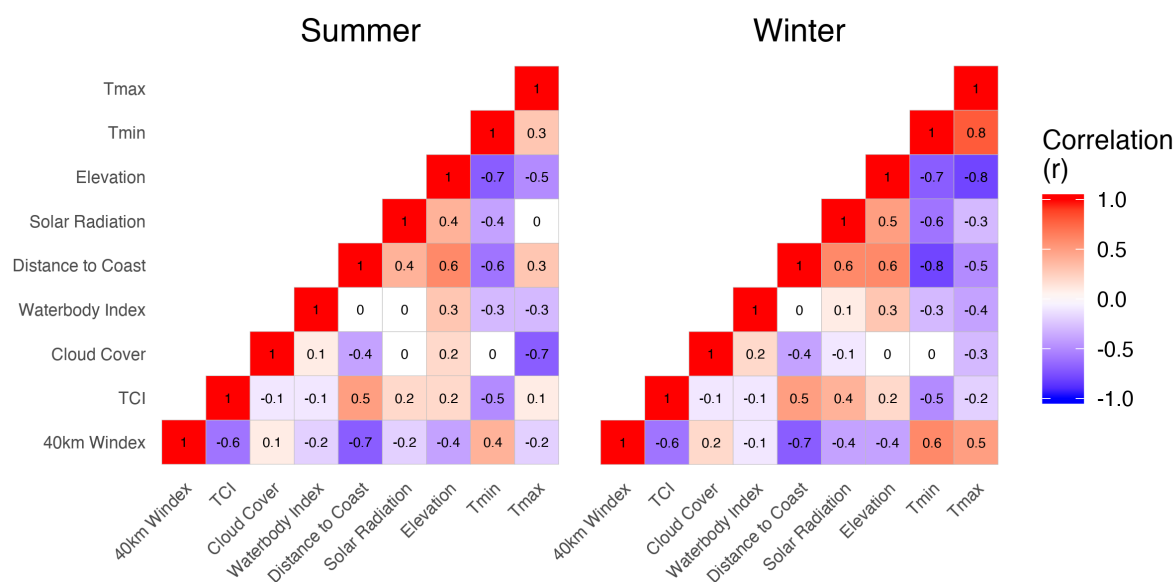


Figure A.1 Correlation matrix for a subset of the covariates associated with the Oregon Cascades stations for Summer and Winter. Numbers and colors indicate the correlation coefficient.

Elevation

Station elevations extracted from the station metadata were used as the covariate in estimating lapse rates.

Topographic Convergence Index (TCI)

Topographic convergence is a proxy for drainage effects (e.g., cold air drainage) that can occur in montane regions (Lundquist et al., 2008; Sadoti et al., 2018). We calculated a topographic convergence index (TCI) value for each station using a 30m digital elevation

model (DEM) from the Shuttle Radar and Topography Mission (SRTM) and the `rsaga.wetness.index` function with default options from the ‘RSAGA’ package (Brenning et al., 2018) in R (R Core Team, 2013).

Solar radiation

Solar radiation exerts a first order control on temperature through the surface energy budget (e.g., Dobrowski et al., 2009). Solar radiation collocated with each station was estimated using a two-step process. An initial estimate of monthly average downwelling shortwave radiation at the surface was acquired from the Weather Research and Forecasting (WRF) model (Liu et al., 2017) at 4 km spatial resolution by averaging data during 2001-2013. WRF solar radiation accounts for cloud cover effects but not terrain effects. We terrain corrected WRF radiation using the ‘insol’ package (Corripio, 2015) in R. The ‘insol’ algorithms account for slope, aspect, self-shading, and shading by adjacent terrain. We calculated monthly solar radiation values by running the algorithm at an hourly timestep for the 15th day of each month using static parameter values for visibility (30 km), relative humidity (50%), and temperature (288K). These parameter values are realistic for the Oregon Cascades domain and the relative values of solar radiation across the stations are insensitive to parameter values. Following Maguire et al., (2019), we calculate a terrain correction factor by dividing calculations using a 30m DEM by calculations using a flat DEM with elevation equal to the mean elevation of the 30m DEM. The terrain correction factor is greater than 1 where the terrain enhances solar radiation receipt (e.g., south-facing slopes) and less than 1 where terrain decreases solar radiation receipt (e.g., in a shaded valley). We multiplied the WRF solar radiation by the terrain correction factor to derive monthly solar radiation accounting for cloud cover and terrain influences.

Cloud cover

Cloud cover can decrease near-surface temperatures during the daytime by reducing incoming solar radiation, but can also influence near-surface temperatures at night through downward longwave radiation (Barry, 1992; Pepin et al., 1999). Additionally, cloud cover is indicative of higher relative humidity, which dampens near-surface lapse rates by increasing latent heating due to condensation (Li et al., 2013; Pepin et al., 1999). Seasonal and annual

means of gridded midday percent cloud cover data derived from 1 km resolution MODIS images (Wilson & Jetz, 2016) were extracted for the grid cell collocated with each station.

Orographic upslope wind index (Windex)

Windward and leeward slopes can experience contrasting climatic and land cover conditions which may affect temperature lapse rates (Lundquist & Cayan, 2007; Minder et al., 2010). Differences in lapse rates between windward and leeward slopes may arise due to: i) gradients in surface available moisture that alter the Bowen ratio and near-surface temperatures, ii) contrasts between moist and dry adiabatic lapse rates, and iii) differences in cloud cover. While previous studies have noted differences in lapse rates and topoclimate between windward and leeward slopes, we are unaware of studies that have delineated this factor as a covariate in topoclimatic modeling. To represent this effect, we developed an orographic upslope wind index (hereafter windex) which can be thought of as a metric of linear stable upslope flow due to prevailing wind direction and topography. The windex represents the magnitude of upslope (positive values) or downslope (negative values) flow at a given location, which indicates whether the location is in a windward or leeward position relative to broad scale circulation patterns.

Monthly 700mb wind velocity from the ERA-Interim reanalysis dataset (Dee et al., 2011) for 2006-2015 were used to calculate the seasonal and annual windex for each station for six different radii: 0.5 km, 1 km, 5 km, 10 km, 20 km, and 40 km. Winds at 700mb were used because they have been identified as relevant to orographic processes in the western U.S. (Luce et al., 2013; Lundquist & Cayan, 2007). The wind fields and 30m DEM were aggregated to the scale of each radii. For each season, the windex was computed as the dot product of the wind vector and the elevation gradient, averaged across years:

$$windex_{s,r} = \frac{1}{ny} \sum_{yr=2006}^{2015} \vec{V}_{yr,s,r} \cdot \nabla elev_{s,r}$$

Equation A.4

where ny is the number of years (10), yr is the year from 2006 to 2015, s is the station, r is the radius, \vec{V} is the interpolated horizontal wind field, and $elev$ is the aggregated DEM.

Distance from coast

The distance from the nearest coastline can affect broad scale atmospheric conditions such as humidity and associated properties of the lower troposphere which can affect lapse rates (Navarro-Serrano et al., 2018). The distance from coast was quantified as the Euclidean distance (km) between each station and the nearest coastline using the `st_distance` function in the R `sf` package (Pebesma, 2018).

Waterbody index

Large waterbodies can have a moderating effect on diurnal and seasonal temperatures. Using a spatial coverage of waterbodies from NHDPlus version 2 (McKay et al., 2012), we developed a waterbody index for each station based on work by Klaić & Kvakić, (2014). Waterbodies were restricted to ‘LakePond’ and ‘Reservoir’ feature types and features with surface area greater than 10 km². For each station, an inverse distance weighted waterbody metric (`wbd_index`) was calculated such that:

$$wbd_index_s = \sum_{w=1}^n \frac{wbd_area_w}{wbd_dist_{w,s}^{1.5}}$$

Equation A.5

where s is each station, w is each waterbody, wbd_area is the surface area in square kilometers of each waterbody, wbd_dist is the distance in kilometers between each waterbody centroid and each station. The waterbodies included in the above calculation are restricted on a station by station basis to those whose centroids are within a 100 km radius of the station, thus n (the total number of waterbodies considered) varies by station. The `wbd_index` declines exponentially with distance from the waterbody and increases linearly with waterbody area.

Free-air temperatures

Free-air temperatures capture regional scale gradients in air mass conditions and can help account for non-elevation effects on temperature (Dobrowski et al., 2009). Monthly free-air temperature and geopotential height were extracted from the ERA-Interim atmospheric reanalysis dataset (Dee et al., 2011) for 2006-2015 on pressure surfaces. Free-air temperatures at 2500m (approximate height of the Cascade crest) were estimated via

linear regression between the two closest elevation pressure levels. Grids were bilinearly interpolated from 0.75° to 0.05° to minimize abrupt changes in temperature values. The monthly fine resolution grids were then aggregated to seasonal grids for each year and values at station locations were extracted.

Free-air lapse rates

Free-air lapse rates are indicative of broad scale atmospheric conditions which can affect near-surface temperature lapse rates (Minder et al., 2010). Free-air lapse rates were estimated using linear regression of free-air temperatures on geopotential heights from ERA-interim for 2006-2015. The vertical extent of values used in the lapse rate calculation was limited to the first pressure surface above model ground level to the pressure surface below 3700m. This elevation range was chosen to focus free-air lapse rates on the vertical region most relevant to near-surface lapse rates and is a few hundred meters above the highest elevation point in the Oregon Cascades, Mt. Hood (3429m). Free-air lapse rates were interpolated from 0.75° to 0.05° and free-air lapse rates collocated with stations were extracted.

References

- Barry, R. G. (1992). Mountain Climatology and Past and Potential Future Climatic Changes in Mountain Regions: A Review. *Mountain Research and Development*, 12(1), 71–86. <https://doi.org/10.2307/3673749>
- Brenning, A., Bangs, D., & Becker, M. (2018). RSAGA: SAGA Geoprocessing and Terrain Analysis R package (Version 1.3.0) [R]. Retrieved from <https://CRAN.R-project.org/package=RSAGA>
- Corripio, M. J. G. (2015). *Package “insol.”* Retrieved from <https://cran.r-project.org/web/packages/insol/insol.pdf>
- Dee, D. P., Uppala, S. M., Simmons, A. J., Berrisford, P., Poli, P., Kobayashi, S., ... Vitart, F. (2011). The ERA-Interim reanalysis: Configuration and performance of the data assimilation system. *Quarterly Journal of the Royal Meteorological Society*, 137(656), 553–597. <https://doi.org/10.1002/qj.828>

- Dobrowski, S. Z., Abatzoglou, J. T., Greenberg, J., & Schladow, S. G. (2009). How much influence does landscape-scale physiography have on air temperature in a mountain environment? *Agricultural and Forest Meteorology*, *149*, 1751–1758. <https://doi.org/10.1016/j.agrformet.2009.06.006>
- Klaić, Z. B., & Kvakić, M. (2014). Modeling the Impacts of a Man-Made Lake on the Meteorological Conditions of the Surrounding Areas. *Journal of Applied Meteorology and Climatology*, *53*(5), 1121–1142. <https://doi.org/10.1175/JAMC-D-13-0163.1>
- Li, X., Wang, L., Chen, D., Yang, K., Xue, B., & Sun, L. (2013). Near-surface air temperature lapse rates in the mainland China during 1962–2011. *Journal of Geophysical Research: Atmospheres*, *118*(14), 7505–7515. <https://doi.org/10.1002/jgrd.50553>
- Liu, C., Ikeda, K., Rasmussen, R., Barlage, M., Newman, A. J., Prein, A. F., ... Yates, D. (2017). Continental-scale convection-permitting modeling of the current and future climate of North America. *Climate Dynamics*, *49*(1–2), 71–95. <https://doi.org/10.1007/s00382-016-3327-9>
- Luce, C. H., Abatzoglou, J. T., & Holden, Z. A. (2013). The Missing Mountain Water: Slower Westerlies Decrease Orographic Enhancement in the Pacific Northwest USA. *Science*, *342*(6164), 1360–1364. <https://doi.org/10.1126/science.1242335>
- Lundquist, J. D., & Cayan, D. R. (2007). Surface temperature patterns in complex terrain: Daily variations and long-term change in the central Sierra Nevada, California. *Journal of Geophysical Research: Atmospheres*, *112*(D11). <https://doi.org/10.1029/2006JD007561>
- Lundquist, Jessica. D., Pepin, N., & Rochford, C. (2008). Automated algorithm for mapping regions of cold-air pooling in complex terrain. *Journal of Geophysical Research: Atmospheres*, *113*(D22). <https://doi.org/10.1029/2008JD009879>
- Maguire, A. J., Eitel, J. U. H., Vierling, L. A., Johnson, D. M., Griffin, K. L., Boelman, N. T., ... Meddens, A. J. H. (2019). Terrestrial lidar scanning reveals fine-scale linkages between microstructure and photosynthetic functioning of small-stature spruce trees at the forest-tundra ecotone. *Agricultural and Forest Meteorology*, *269–270*, 157–168. <https://doi.org/10.1016/j.agrformet.2019.02.019>

- McKay, L., Bondelid, T., Dewald, T., Johnston, J., Moore, R., & Rea, A. (2012). *NHDPlus Version 2: User Guide*. Retrieved from https://s3.amazonaws.com/nhdplus/NHDPlusV21/Documentation/NHDPlusV2_User_Guide.pdf
- Minder, J. R., Mote, P. W., & Lundquist, J. D. (2010). Surface temperature lapse rates over complex terrain: Lessons from the Cascade Mountains. *Journal of Geophysical Research: Atmospheres*, *115*(D14), D14122. <https://doi.org/10.1029/2009JD013493>
- Navarro-Serrano, F., López-Moreno J. I., Azorin-Molina C., Alonso-González E., Tomás-Burguera M., Sanmiguel-Valladolid A., ... Vicente-Serrano S. M. (2018). Estimation of near-surface air temperature lapse rates over continental Spain and its mountain areas. *International Journal of Climatology*, *38*(8), 3233–3249. <https://doi.org/10.1002/joc.5497>
- Pebesma, E. (2018). Simple Features for R: Standardized Support for Spatial Vector Data. *The R Journal*, *10*(1), 439–446. <https://doi.org/10.32614/RJ-2018-009>
- Pepin, N., Benham, D., & Taylor, K. (1999). Modeling Lapse Rates in the Maritime Uplands of Northern England: Implications for Climate Change. *Arctic, Antarctic, and Alpine Research*, *31*(2), 151–164. <https://doi.org/10.2307/1552603>
- R Core Team. (2013). *R: A language and environment for statistical computing*. Retrieved from <http://www.R-project.org/>
- Sadoti, G., McAfee, S. A., Roland, C. A., Fleur Nicklen, E., & Sousanes, P. J. (2018). Modelling high-latitude summer temperature patterns using physiographic variables. *International Journal of Climatology*, *38*(10), 4033–4042. <https://doi.org/10.1002/joc.5538>
- Wilson, A. M., & Jetz, W. (2016). Remotely Sensed High-Resolution Global Cloud Dynamics for Predicting Ecosystem and Biodiversity Distributions. *PLOS Biology*, *14*(3), e1002415. <https://doi.org/10.1371/journal.pbio.1002415>

Appendix B - SnowClim: High-Resolution Snow Model and Data for the Western United States

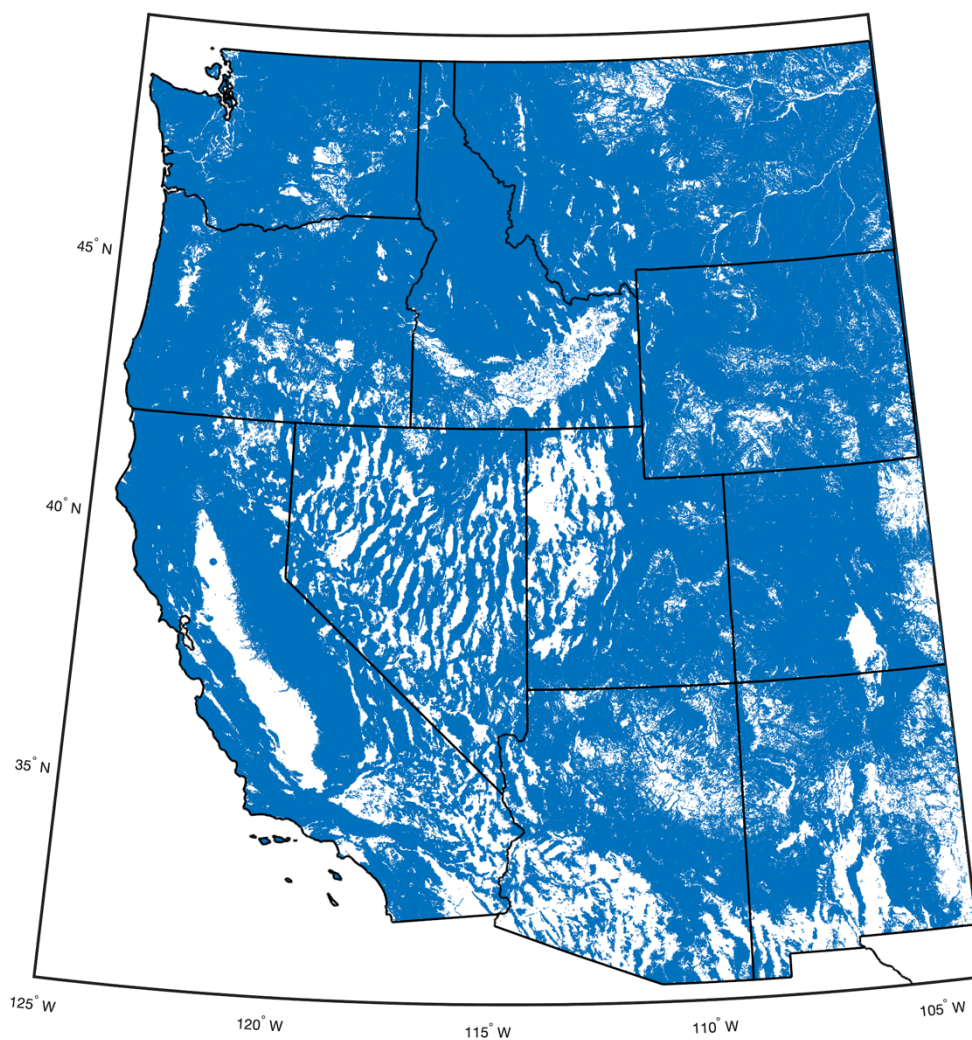


Figure B.1 Map of modeling domain with locations modeled at 210m spatial resolution in blue.

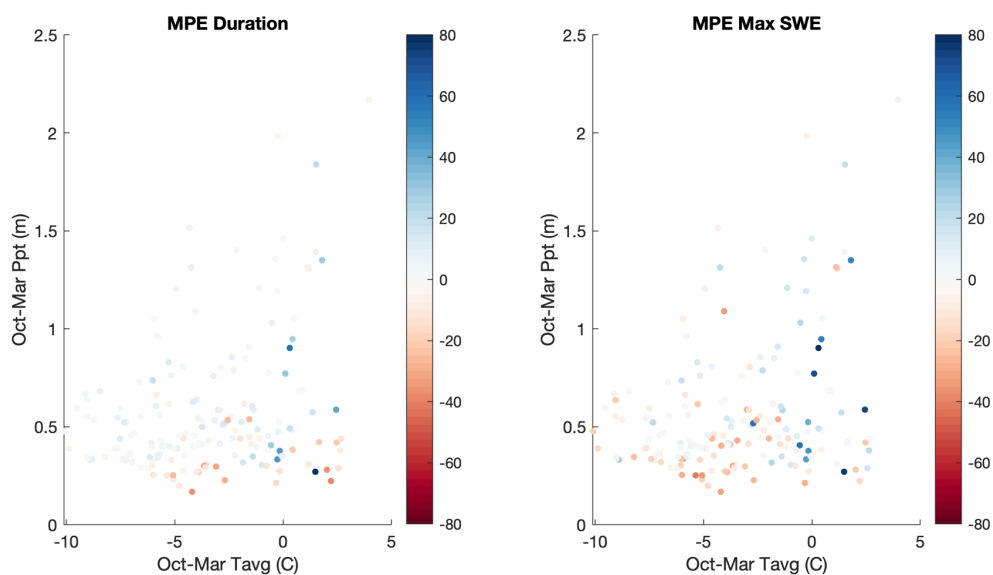


Figure B.2 Performance of best hourly model at SNOTEL sites in temperature-precipitation space. Each point represents a SNOTEL site.

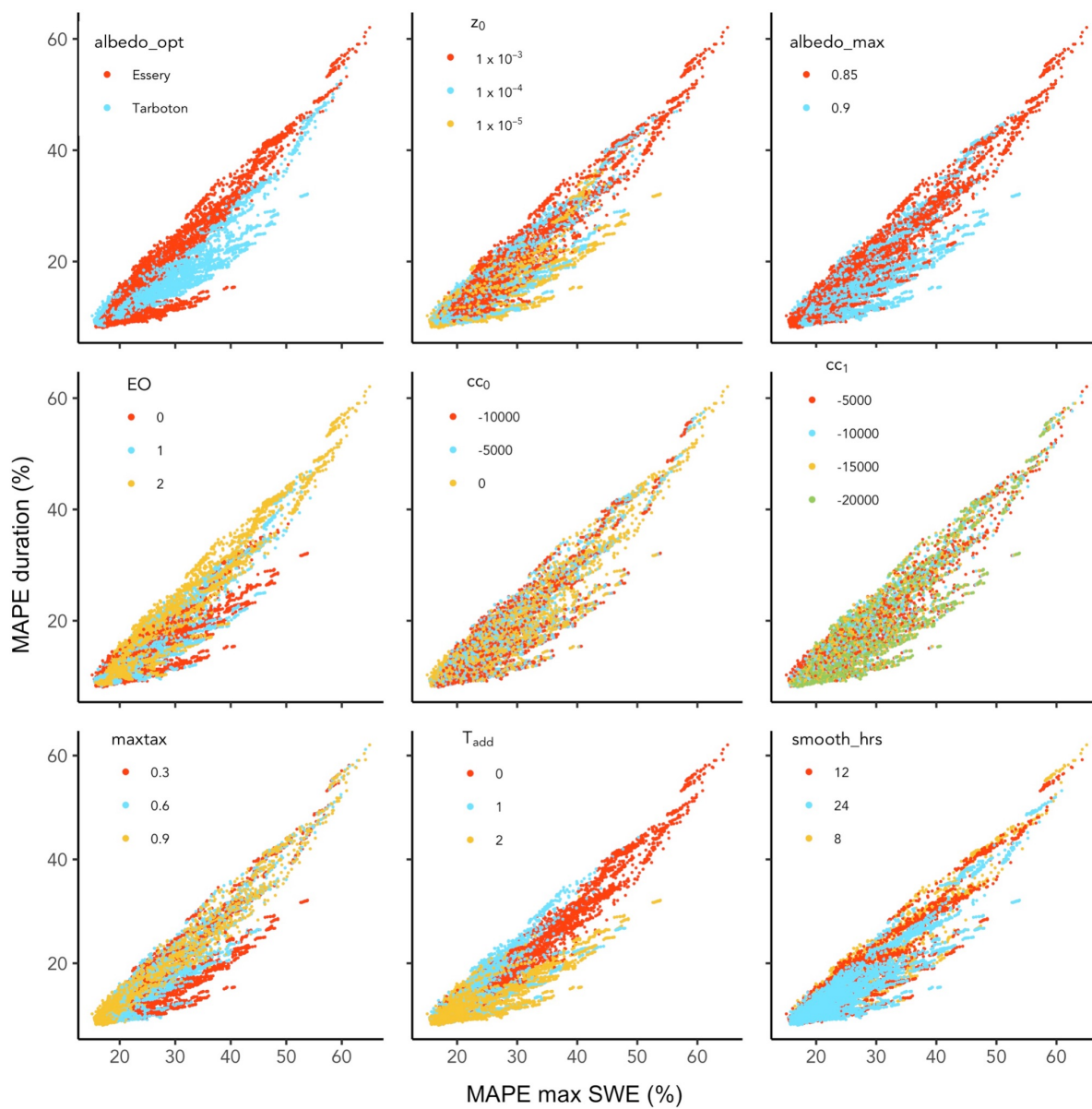


Figure B.3 Parameter sensitivity of hourly model performance

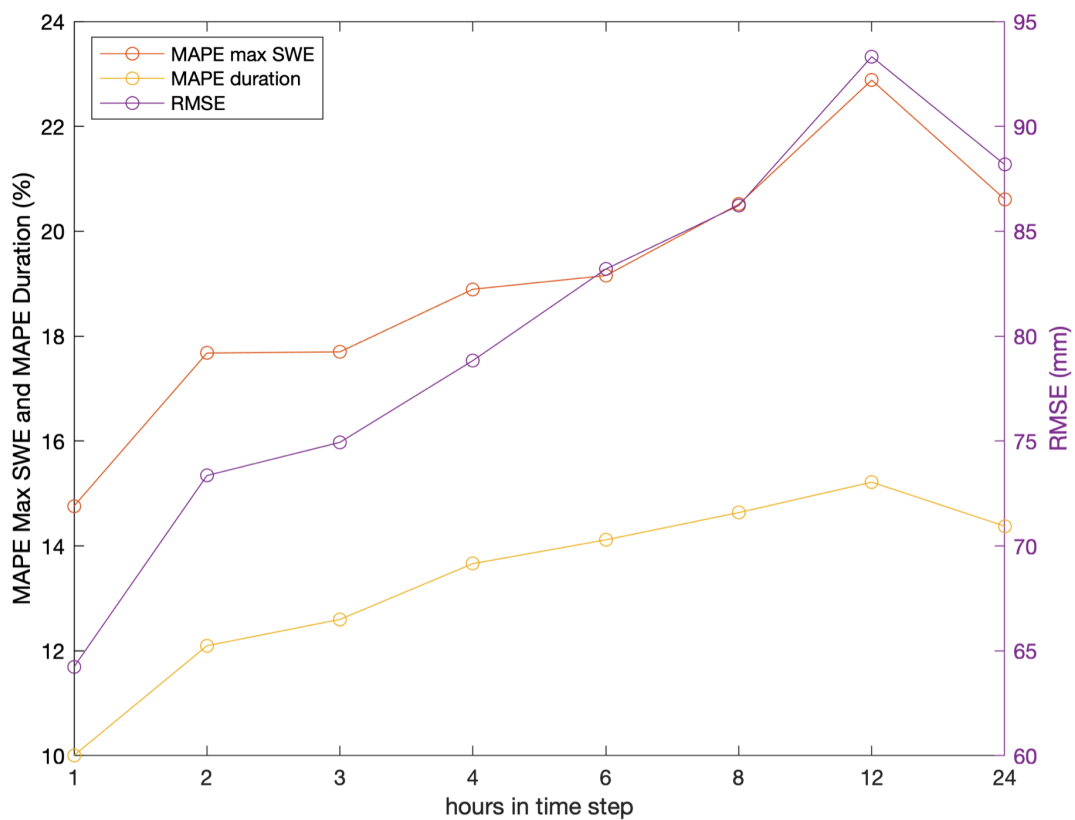


Figure B.4 Performance of snow model without shallow snow correction for different time steps using the parameter set selected in calibration of the hourly model with shallow snow correction. Points represent median values across 170 SNOTEL sites.

Appendix C - Projected Loss of Active Rock Glaciers in the Western U.S. with Warming

Data

Description of Covariates

Climate is one key determinant of rock glacier distributions. Temperature is relevant to processes of snow accumulation and ablation, active layer thickness, and freeze-thaw debris production (Haeberli et al., 2006). Precipitation contributes to snow accumulation and ice flux to supply the rock glacier, however rain and meltwater also have the potential to infiltrate the surface debris layer, contributing to latent heating of the ice and to erosion of finer sediments from the rock glacier surface (Kenner & Magnusson, 2017). Solar radiation shapes the strong spatial variability of available energy in complex terrain and rock glaciers are often found in shaded areas such as northern aspects or cirques (Johnson et al., 2007). We consider the following metrics: mean, minimum, and maximum annual temperatures, annual number of temperature oscillations around 0°C, annual precipitation, annual rainfall, and mean annual downward solar radiation (Table C.1).

Snow accumulation is necessary to provide the ice flux for rock glacier development and persistence. However, snow is not universally beneficial to rock glaciers. Too much snow can increase the ice to debris ratio, leading to the formation of a debris covered glacier or ice glacier instead of a rock glacier (Anderson et al., 2018). The insulating effects of snow are also a double-edged sword; snow cover limits the advection of air within the debris matrix which prevents warming when air temperatures are above freezing, but also can limit advective cooling when the air is cold (Wagner et al., 2019). The snow metrics we used included annual snowfall water equivalent (sfe), snow duration (duration), annual maximum snow water equivalent (maxswe), and the number of snow free days between the snow on and snow off dates (nosnowdays). Snow on (off) was defined as the first (last) day of the first (last) period of 5 consecutive days of snow cover each year. Duration was calculated as the difference between the snow on and off dates.

Aspect is indicative of solar radiation loading which provides energy for snow and ice melt as well as for freeze-thaw debris production, and can be associated with preferential

Table C.1 Environmental covariates used in the Maxent model. ¹Lute et al., (2021); ²Gesch et al., (2018); ³Anning & Ator, (2017).

Environmental Covariate	Short Name	Data Source	Relevant Processes
Minimum, maximum, and mean annual temperature, annual number of temperature oscillations around °0C	tmin, tmax, tmean, freeze-thaw	SnowClim ¹	Snow accumulation, snow melt, freeze-thaw debris production
Annual precipitation	precip	SnowClim ¹	Snow accumulation, water infiltration in rock matrix
Annual rainfall	rain	SnowClim ¹	Precipitation heat flux, propensity to wash debris off of rock glacier surface
Mean annual downward shortwave radiation	solar	SnowClim ¹	Available energy for melt, snow cover duration
Annual SFE, snow duration, annual maximum SWE, number of snow free days between snow on and snow off dates	sfe, duration, maxswe, nosnowdays	SnowClim ¹	Accumulation zone productivity, surface insulation
Aspect	aspect	Derived from NED ²	Solar radiation loading, snow ablation
Slope	slope	Derived from NED ²	Rock glacier driving stress, velocity
Headwall Metric (using 3x3 window and 5x5 window)	headwall3, headwall5	Derived from NED ²	Debris supply source, avalanche supplementation of snowpack
Rock Type	rocktype	USGS ³	Fracture propensity, debris supply, clast size

snow loading if aligned with prevailing winds. Slope is a key variable for calculating the driving stress and velocity of rock glaciers and provides a constraint on suitable rock glacier

Table C.2 Descriptions of numeric lithology classes which were used as a categorical variable in the Maxent model. Data is from Anning & Ator, (2017).

Class number	Class abbreviation	Class description
1	CARB	sediments and sedimentary rocks. Carbonate rocks such as limestone and dolostone. Generally, any rock including any minor carbonate lithology is included in this group. Some special cases exist where carbonates are also identified based on LITH62MINO field.
2	CLAST_C	sediments and sedimentary rocks. Clastic sediments/rocks primarily made of sands, gravels, cobbles, or larger clasts.
3	CLAST_F	sediments and sedimentary rocks. Clastic sediments/rocks primarily made of fine-grained materials such as shale, siltstone, claystone, mudstone, etc.
4	CLAST_U	sediments and sedimentary rocks. Clastic sediments/rocks of unknown or highly variable clast sizes.
5	EVAP	sediments and sedimentary rocks. Evaporites or playas.
6	META	Metamorphic rocks.
7	PLUT_OTH	Igneous, generally mafic, other less quartz-rich plutonic rocks, such as monzonite or gabbro.
8	PLUT_QTZ	Igneous, generally felsic, quartz-rich plutonic rocks such as granitoids, granite, granodacite.
9	VOLC_OTH	Igneous, generally mafic, volcanic rocks, such as basalt that are mineralogically equivalent to the less quartz-rich plutonic rocks.
10	VOLC_QTZ	Igneous, generally felsic, volcanic rocks such as rhyolite and dacite that are mineralogically equivalent to the quartz-rich plutonic rocks.
11	WATER	Water or ice
12	NONE	

locations since rock glaciers are typically located on 5°-30° slopes which promote downslope movement but are not so steep that the rock glacier detaches from sources of debris and ice (Kenner & Magnusson, 2017; Sloan & Dyke, 1998).

Several studies have demonstrated the importance of rock headwalls as sources of debris and avalanched snow for rock glaciers (Morris, 1981; Müller et al., 2016). We assessed two different headwall metrics, described in the main text. One used a 5x5 window and the other used a 3x3 window of grid cells centered on the target pixel and both used a slope threshold of 30°. Similar headwall metrics showed up as key predictors of rock glacier presence in preliminary work.

Geologic considerations are also relevant to rock glacier distributions. In particular, the fracturing propensity and characteristic clast size of the rock help determine the rate of debris supply and the size of the debris, which is relevant to rock glacier energy budgets (Ikeda & Matsuoka, 2006; Kenner & Magnusson, 2017). Explanations of the classes in the generalized lithology layer we used (Anning & Ator, 2017) are provided in Table C.2.

Covariate Preparation

Collinearity of predictor variables can hamper the interpretation of the importance and effect of different predictors and can degrade model transferability when the collinearity structure changes between calibration and projection datasets (Dormann et al., 2013; Feng et al., 2019). Collinearity was assessed by computing Pearson correlations coefficients (r) between each pair of predictors (Figure C.1). Combinations with $|r| > 0.7$ were considered to be problematic (Dormann et al., 2013). In cases with $|r| > 0.7$, we chose which collinear variable to include/remove by considering the results of the Maxent jackknife procedure (Figure 4.3a). The approach calculates the loss in regularized training gain when each variable is left out of a model and calculates the regularized training gain of a model built on that variable alone. For these models we used default parameter options. This resulted in the removal of headwall3, tmin, tmax, maxswe, duration, and precip, leaving 10 covariates.

We assessed changes in the collinearity structure between the pre-industrial, present, and future time periods by comparing correlation matrices for the three time periods. For the variables we retained from the previous step, the only variable that had substantial changes in collinearity was freeze-thaw; the sign of the correlation between freeze-thaw and several

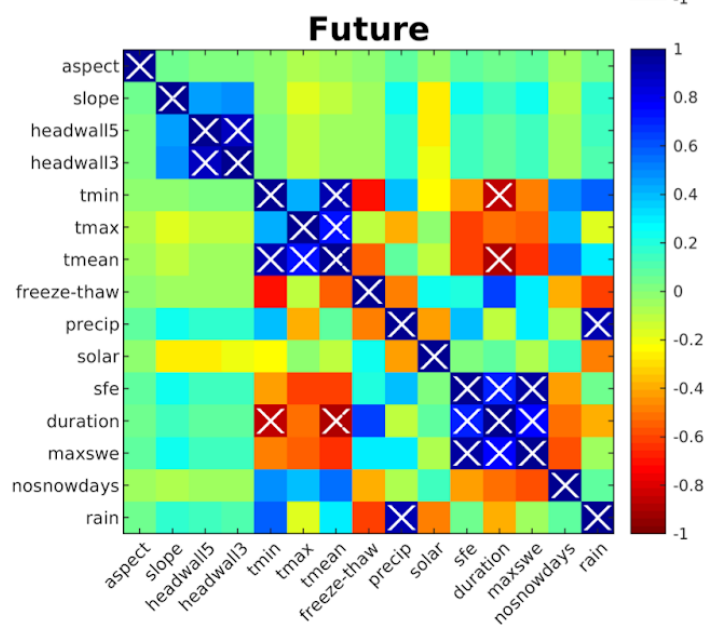
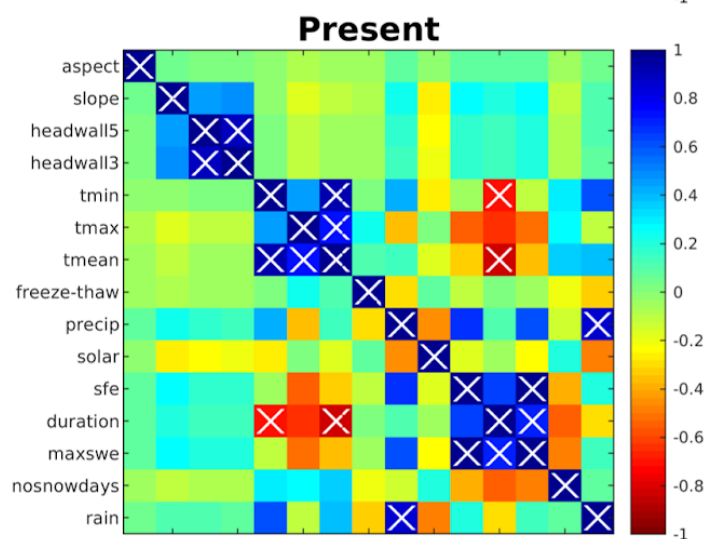
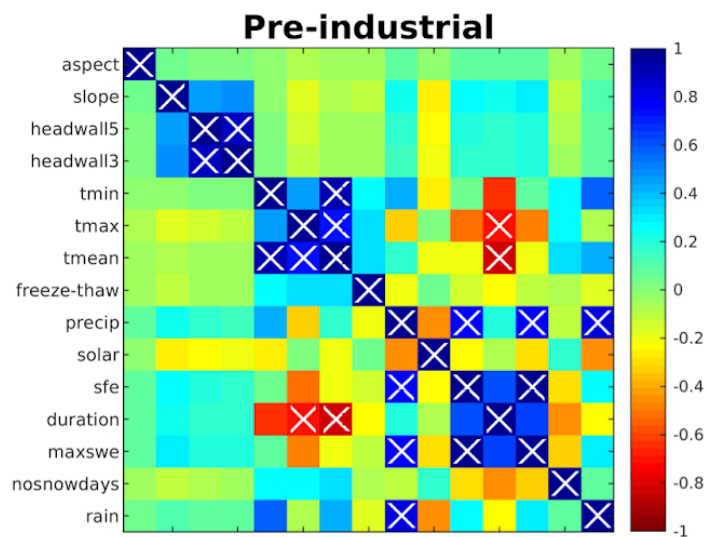


Figure C.1 Correlation matrices for pre-industrial, present, and future time periods. White x's denote correlations with absolute values greater than 0.7.

other variables changed between the pre-industrial and future time periods. To avoid complications in prediction, we excluded freeze-thaw from the model, leaving 9 covariates.

Model Complexity

To identify the appropriate level of model complexity, we constructed a series of models with varying values of the regularization parameter (beta) and feature classes (including linear (L), quadratic (Q), threshold (T), and hinge (H)). We excluded product features in the interest of interpretability of the results. We used the ENMeval package (Kass et al., 2021) in R to evaluate the performance of these models using the AICc statistic (Akaike, 1974), which penalizes model complexity and has been shown to outperform AUC based methods of selecting optimal Maxent model complexity (Warren & Seifert, 2011). We built a model for each combination of beta parameter (1 (the default), 3, 5, 7, 9) and feature class (L, LQ, LH, LT, LQH, LQT, LQTH). The model with the lowest AICc was considered the best model. Our analysis showed that the model with a regularization beta of 5 and linear, quadratic, and threshold features provided the optimal performance (Figure C.2). However, a more parsimonious model with LQTH features and beta of 7 performed similarly well and gave similar results. We chose to use this model in the interest of interpretability of the results. The selected model was used to map rock glacier probability of presence across the domain based on Maxent's cloglog output.

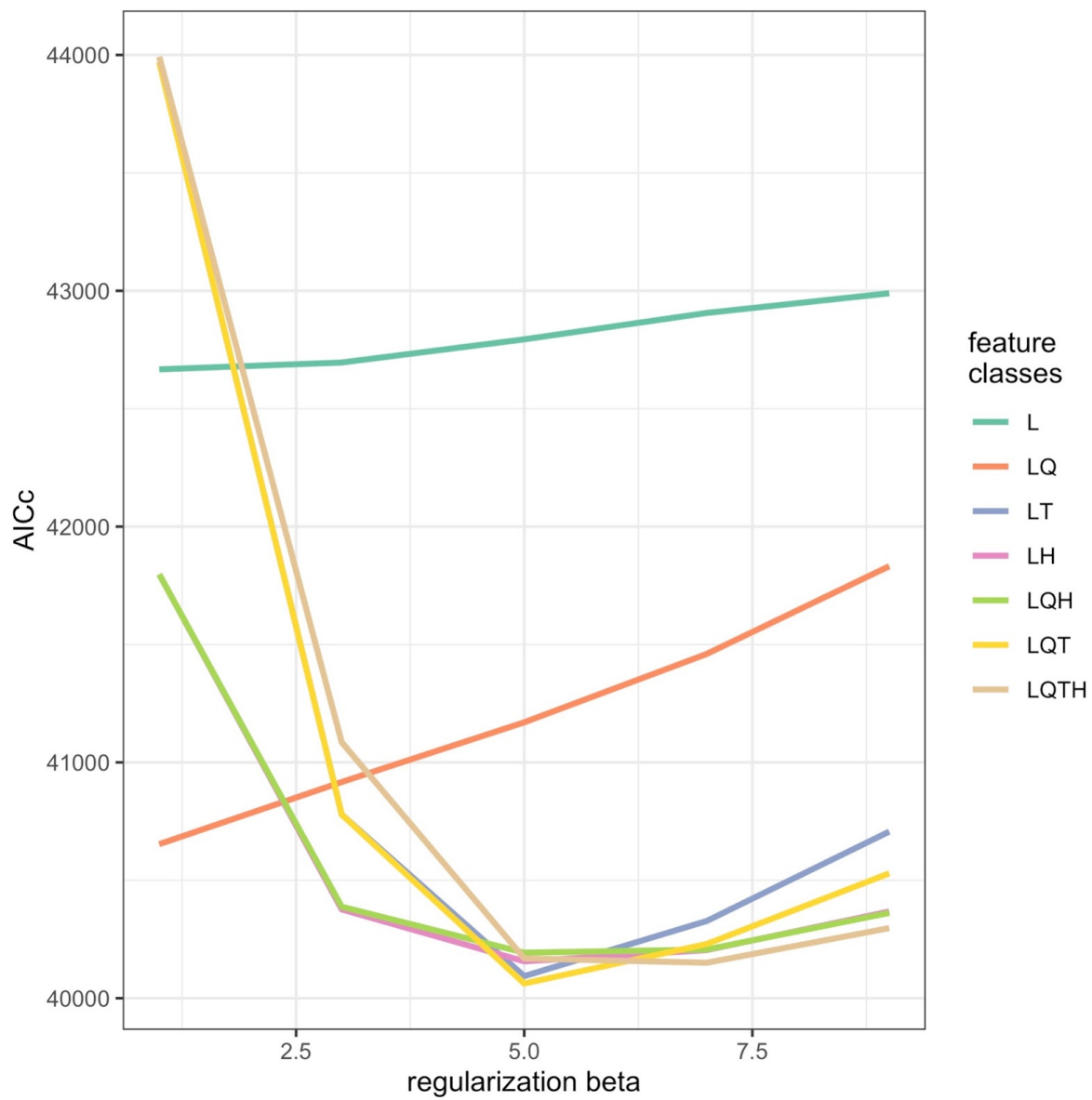


Figure C.2 AICc values for different levels of regularization beta parameter and different feature class combinations.

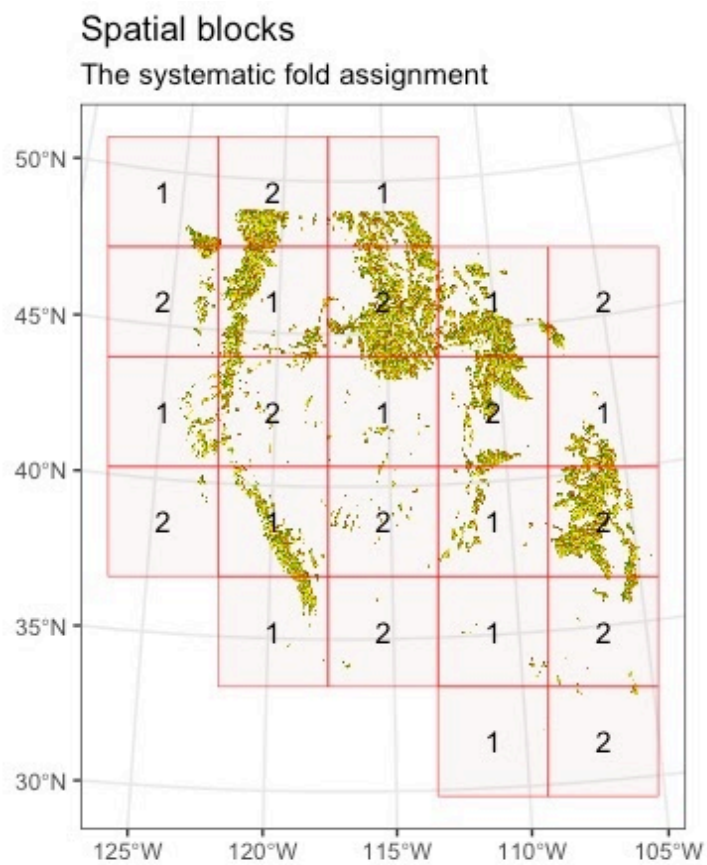


Figure C.3 Map of spatial blocks used in the spatial cross validation analysis overlaid on western U.S. modeling domain. Blocks were grouped into folds as indicated by the number in each block.

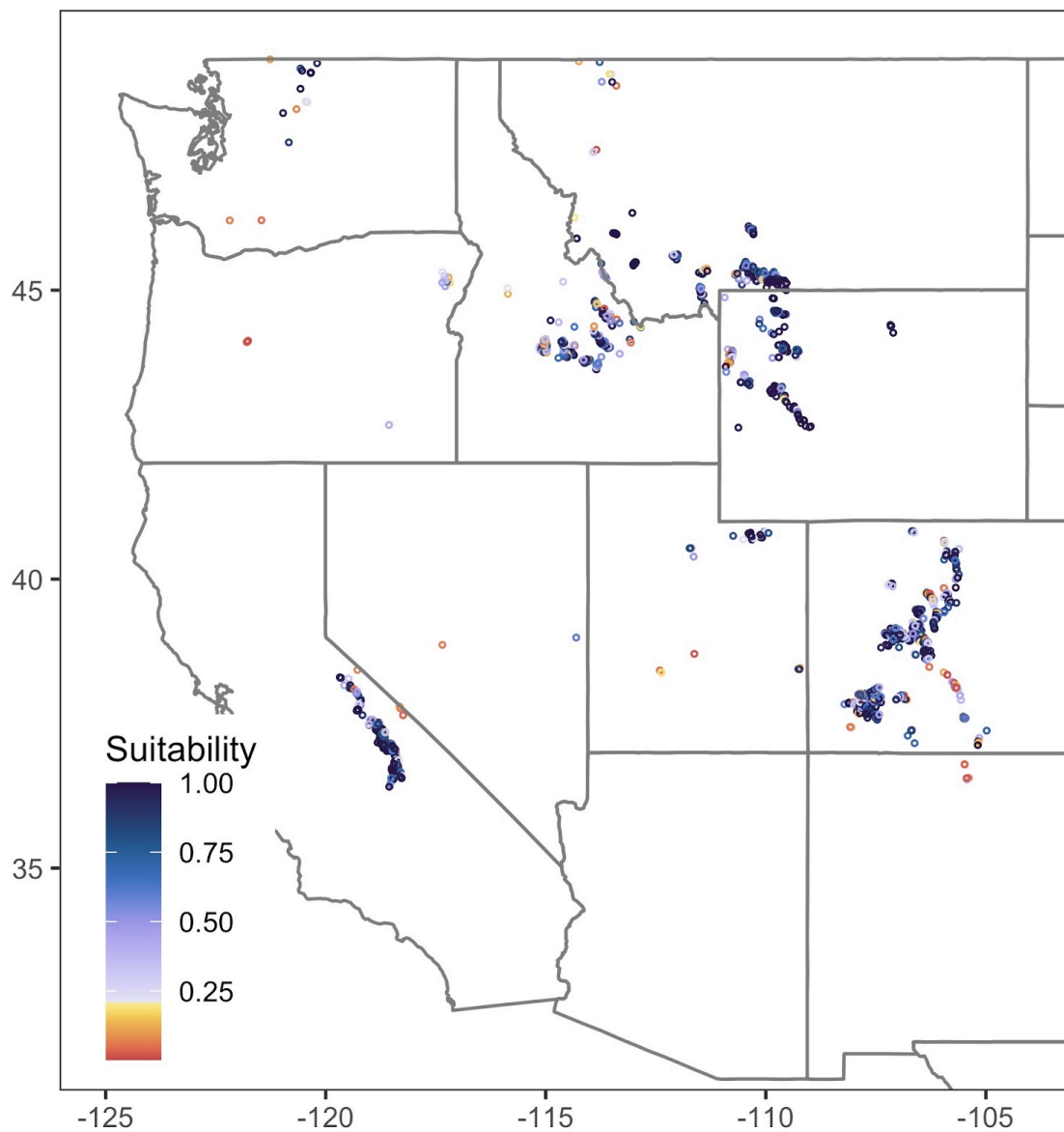


Figure C.4. Predicted pre-industrial suitability at known rock glacier locations. Color scale is divided at the threshold that excludes 10% of known rock glaciers (0.212).

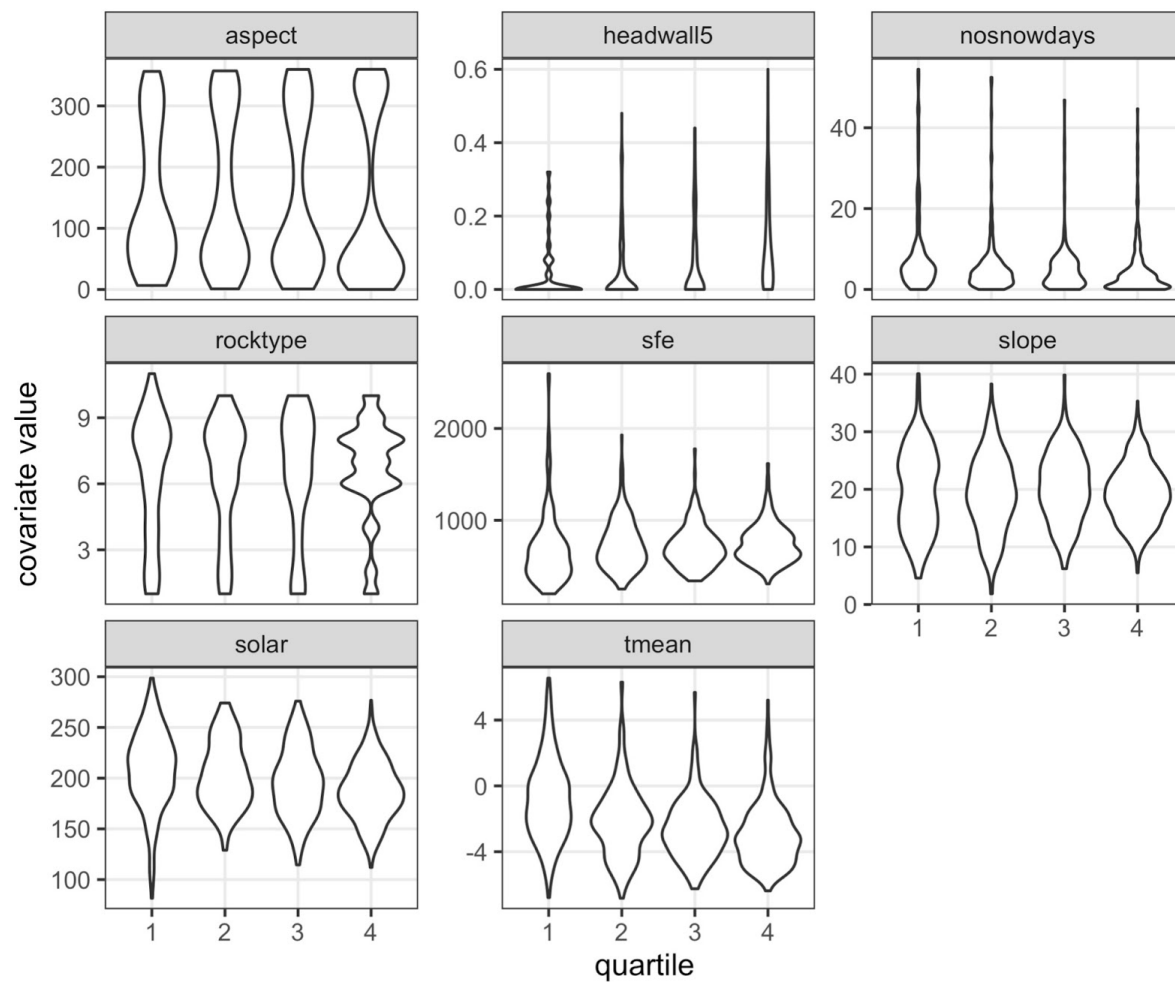


Figure C.5. Pre-industrial covariate distributions at known rock glacier locations. Quartiles on the x-axis are quartiles of predicted suitability with 1 being the least suitable and 4 being the most suitable.

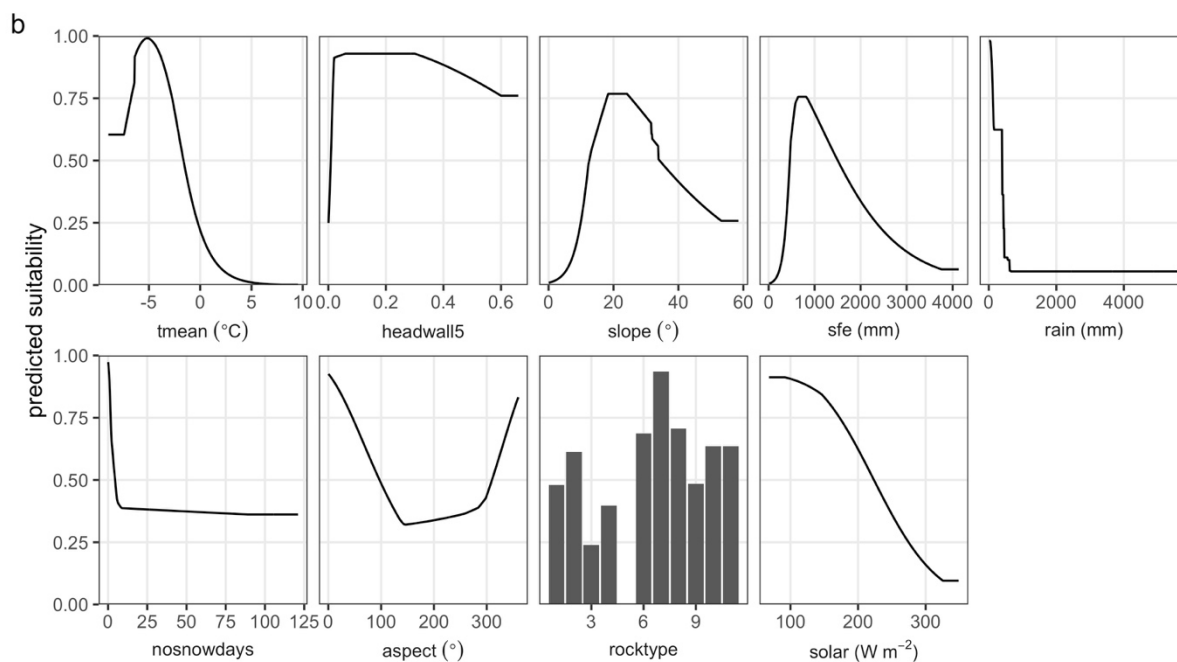


Figure C.6. Response functions illustrating the relationship between the covariate values (x-axis) and the rock glacier habitat suitability (y-axis) based on models built on each variable in isolation.

Table C.3 AUC values from cross-validation experiments. Calibration AUC is the AUC from the model calibrated on the indicated spatial fold. Validation AUC is the AUC of the model calibrated on the other fold and validated on the indicated spatial fold. Delta AUC is the difference between the calibration and validation AUC values.

	Calibration AUC	Validation AUC	Delta AUC
Spatial block fold 1	0.99	0.93	0.06
Spatial block fold 2	0.98	0.90	0.08
Cold to warm	0.90	0.90	0.00

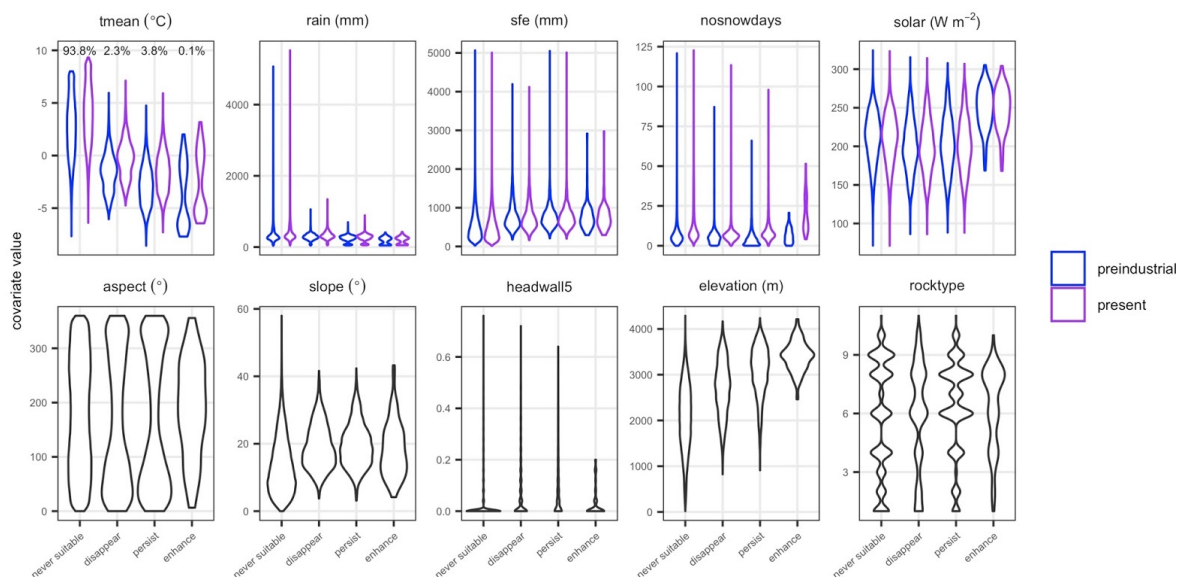


Figure C.7. Distribution of covariates between preindustrial (blue) and present (purple) time periods, grouped by suitability change category. For covariates that are not time-varying (bottom row), a single violin is shown for each suitability category. In the first subplot, percent values indicate the percent of the full modeling domain that falls into each category.

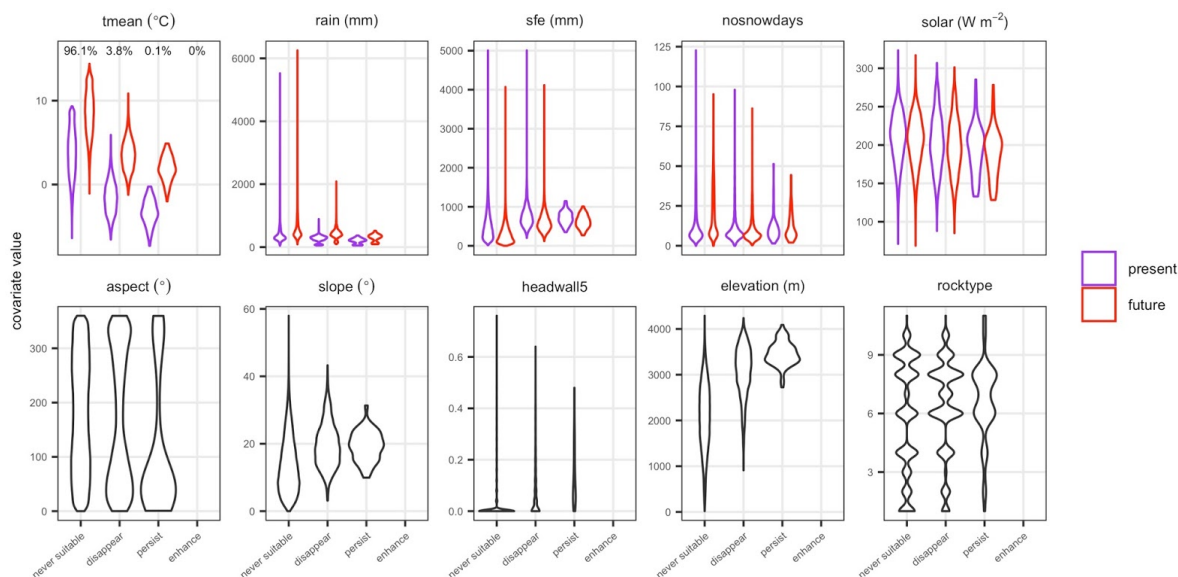


Figure C.8. Distribution of covariates between present (purple) and future (red) time periods, grouped by suitability change category. For covariates that are not time-varying (bottom row), a single violin is shown for each suitability category. In the first subplot, percent values indicate the percent of the full modeling domain that falls into each category.

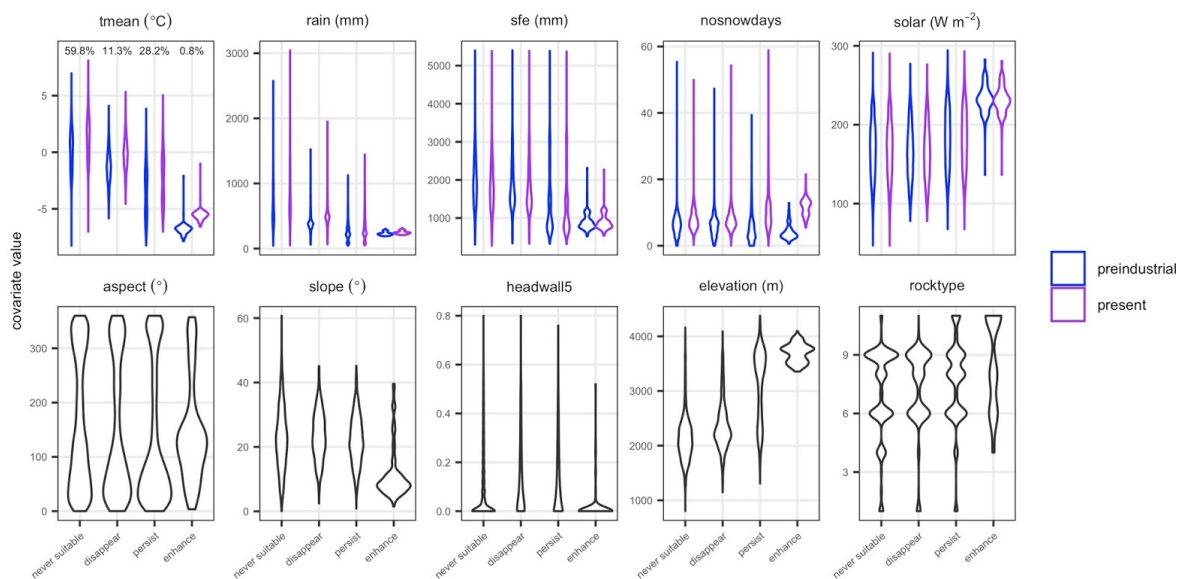


Figure C.9. Distribution of covariates between preindustrial (blue) and present (purple) time periods, for presently glaciated locations, grouped by suitability change category. For covariates that are not time-varying (bottom row), a single violin is shown for each suitability category. In the first subplot, percent values indicate the percent of modeled glaciated area that falls into each category.

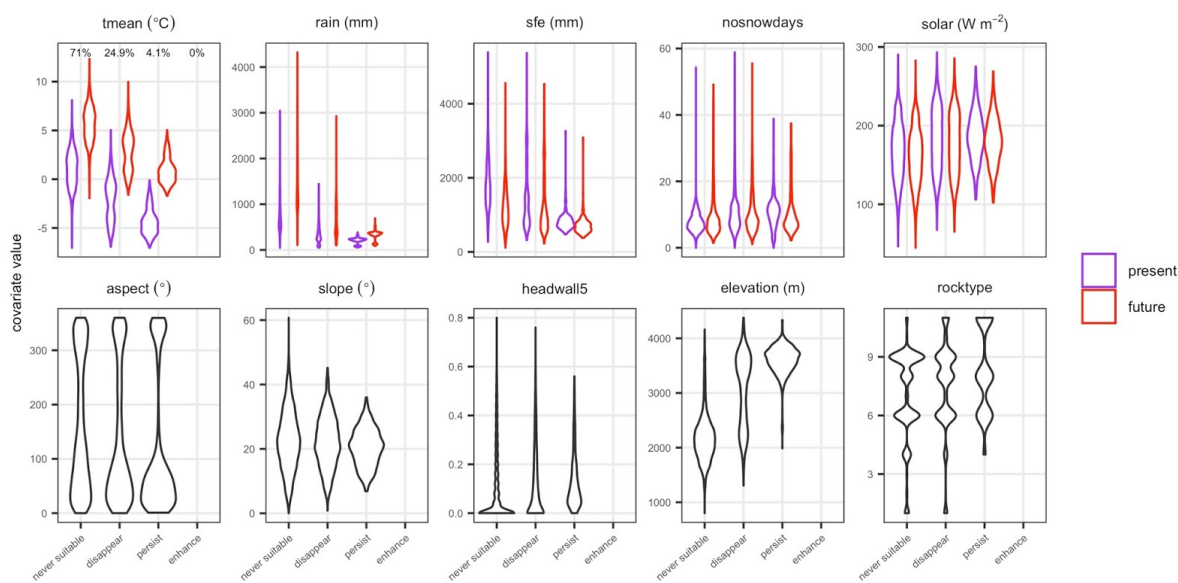


Figure C.10. Distribution of covariates between present (purple) and future (red) time periods, for presently glaciated locations, grouped by suitability change category. For covariates that are not time-varying (bottom row), a single violin is shown for each suitability category. In the first subplot, percent values indicate the percent of modeled glaciated area that falls into each category.

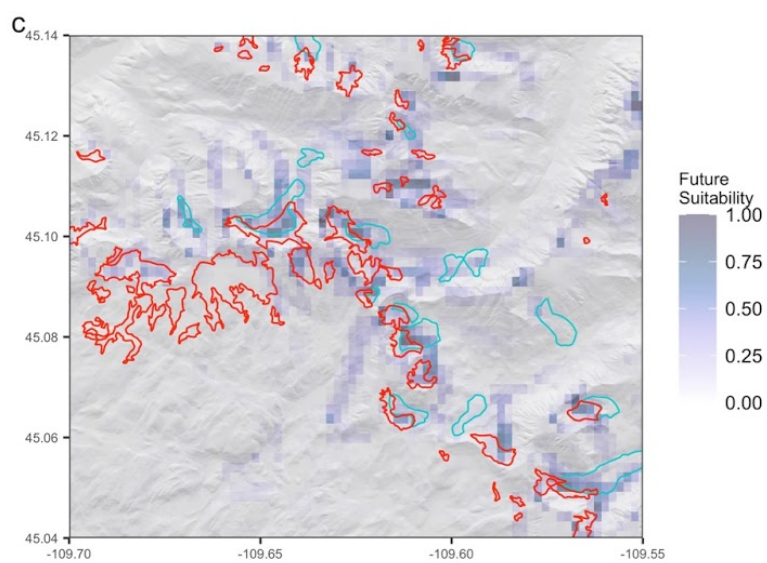
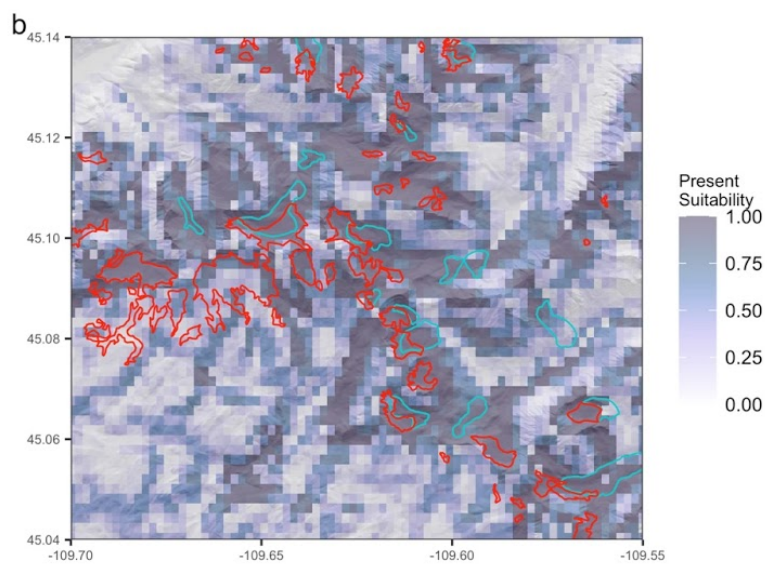
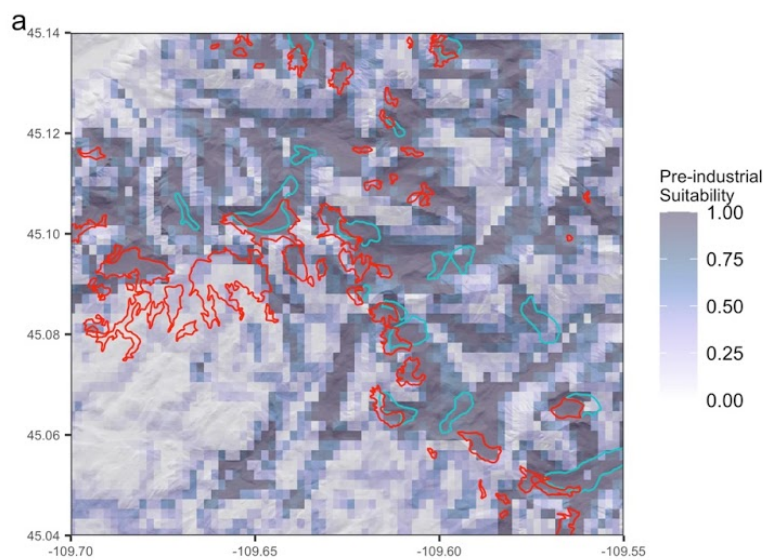


Figure C.11. Predicted suitability for rock glaciers under pre-industrial (a), present (b), and future (c) conditions across the Beartooth Mountains, Montana domain. Red and turquoise outlines mark the locations of present day glaciers and rock glaciers, respectively.

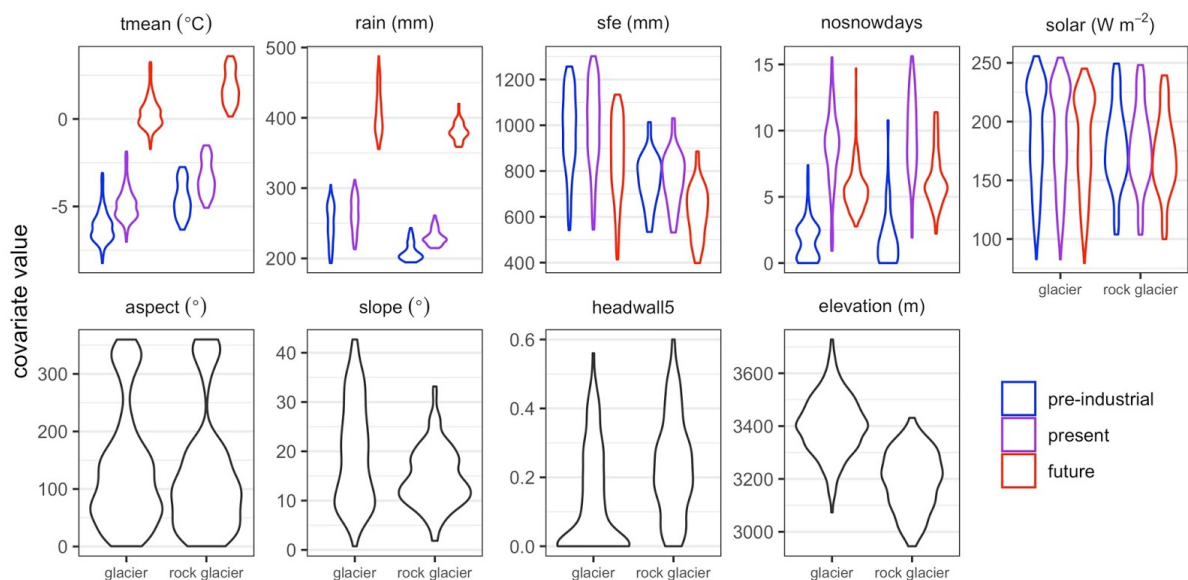


Figure C.12. Changes in environmental covariates over time at locations corresponding to present day glaciers and present-day rock glaciers in the Beartooth Mountains domain. Topographic variables, which do not change over time, are represented by one violin for glaciers and one for rock glaciers. The rocktype covariate is excluded from the plot because all glacier and rock glacier locations in the domain had the same rocktype (class 6).

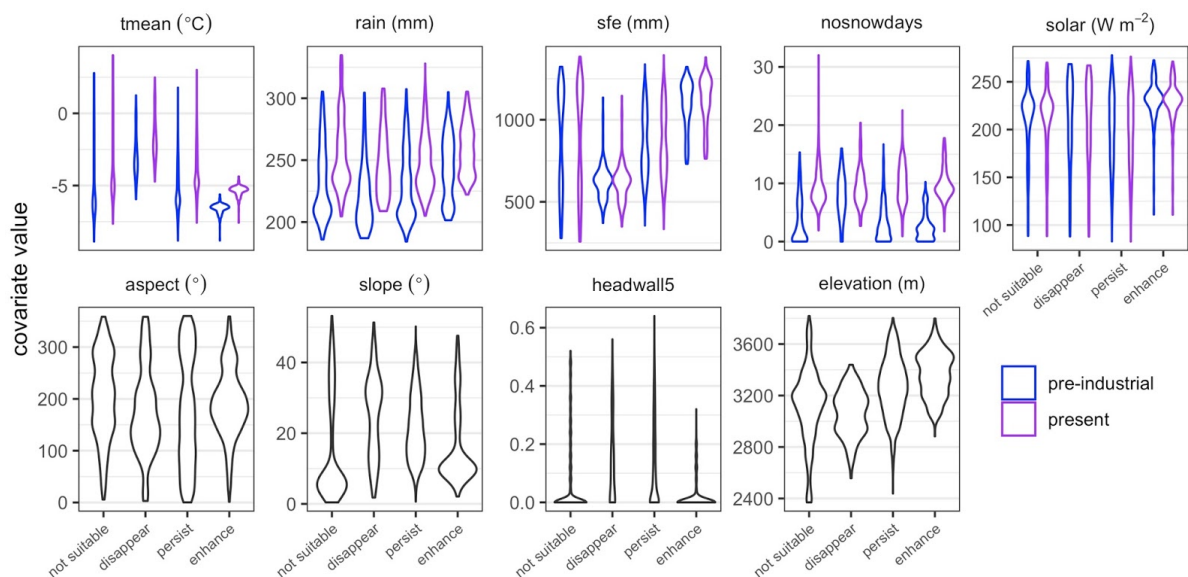


Figure C.13. For locations in the Beartooth Mountains, Montana, distributions of covariate values under pre-industrial and present conditions grouped by habitat suitability class. The rocktype covariate is not shown because the region has a single rocktype (class 6).

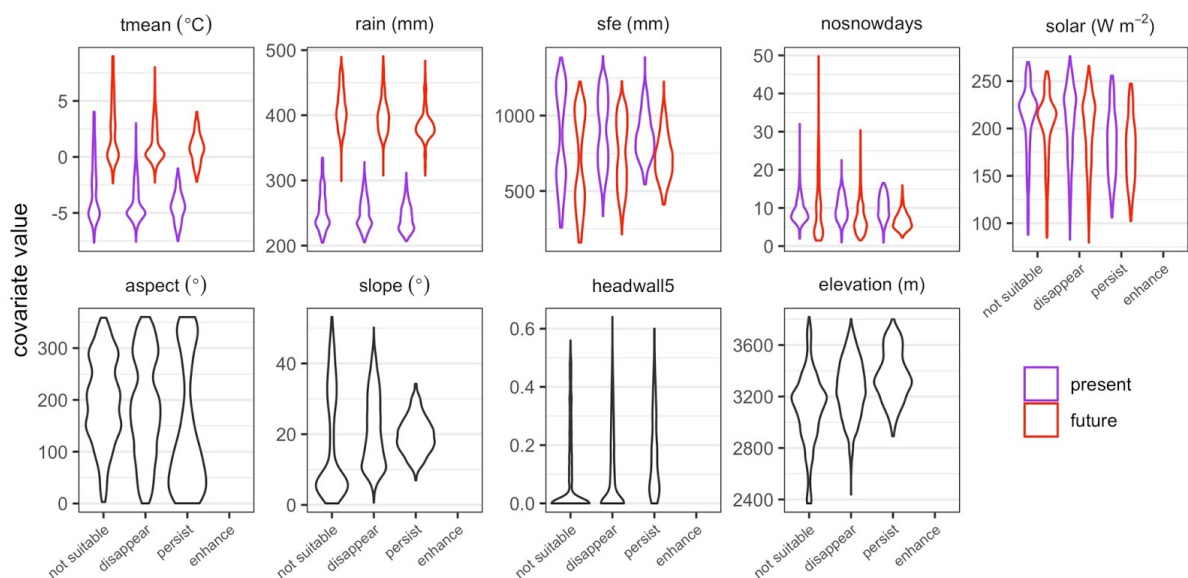


Figure C.14. For locations in the Beartooth Mountains, Montana, distributions of covariate values under present and future conditions grouped by habitat suitability class. The rocktype covariate is not shown because the region has a single rocktype (class 6).

Table C.4. Summary of pre-industrial, historical, and future rock glacier habitat, grouped by level III ecoregion. Suitable and unsuitable areas are defined by the 0.212 threshold as discussed in the text. Values are in km², except for the percent changes which are in %. Total column shows the area of the whole ecoregion, whereas the Modeled column shows the area within the ecoregion that was included in the distribution model.

Ecoregion Number	Ecoregion Name	Total	Modeled	Suitable								Unsuitable							
				Pre-industrial	Historical	Future	Absolute Change Pre-Hist	Absolute Change Hist-Fut	Percent Change Pre-Hist	Percent Change Hist-Fut	Pre-industrial	Historical	Future	Absolute Change Pre-Hist	Absolute Change Hist-Fut	Percent Change Pre-Hist	Percent Change Hist-Fut		
1	Coast Range	54,242.96	10,570.21	0.14	0.00	0.00	-0.14	0.00	-100.0	0.0	10,570.07	10,570.21	10,570.21	0.14	0.00	0.0	0.0		
2	Puget Lowland	16,971.80	544.06	0.00	0.00	0.00	0.00	0.00	0.0	0.0	544.06	544.06	544.06	0.00	0.00	0.0	0.0		
3	Willamette Valley	14,883.85	26.98	0.00	0.00	0.00	0.00	0.00	0.0	0.0	26.98	26.98	26.98	0.00	0.00	0.0	0.0		
4	Cascades	58,855.32	33,928.16	135.78	62.22	0.14	-73.56	-62.09	-54.2	-99.8	33,792.38	33,865.94	33,928.03	73.56	62.09	0.2	0.2		
5	Sierra Nevada	53,102.33	26,148.69	2,858.96	2,554.80	58.47	-304.16	-2,496.33	-10.6	-97.7	23,289.73	23,593.89	26,090.22	304.16	2,496.33	1.3	10.6		
6	Central California Foothills and Coastal Mountains	76,679.41	4.41	0.00	0.00	0.00	0.00	0.00	0.0	0.0	4.41	4.41	4.41	0.00	0.00	0.0	0.0		
7	Central California Valley	46,488.54	0.00	-	-	-	-	-	-	-	-	-	-	-	-	-	-		
8	Southern California Mountains	15,837.68	546.23	0.07	0.00	0.00	-0.07	0.00	-100.0	0.0	546.16	546.23	546.23	0.07	0.00	0.0	0.0		
9	Eastern Cascades Slopes and Foothills	53,257.96	7,666.95	1.10	0.03	0.00	-1.07	-0.03	-96.9	-100.0	7,665.84	7,666.91	7,666.95	1.07	0.03	0.0	0.0		
10	Columbia Plateau	83,131.47	160.73	0.00	0.00	0.00	0.00	0.00	0.0	0.0	160.73	160.73	160.73	0.00	0.00	0.0	0.0		
11	Blue Mountains	70,909.50	16,660.02	173.75	78.25	0.00	-95.51	-78.25	-55.0	-100.0	16,486.27	16,581.78	16,660.02	95.51	78.25	0.6	0.5		
12	Snake River Plain	53,627.48	167.45	0.00	0.00	0.00	0.00	0.00	0.0	0.0	167.45	167.45	167.45	0.00	0.00	0.0	0.0		
13	Central Basin and Range	308,791.05	9,421.31	139.40	93.65	0.10	-45.75	-93.54	-32.8	-99.9	9,281.91	9,327.66	9,421.21	45.75	93.54	0.5	1.0		
14	Mojave Basin and Range	127,689.93	97.23	0.00	0.00	0.00	0.00	0.00	0.0	0.0	97.23	97.23	97.23	0.00	0.00	0.0	0.0		
15	Northern Rockies	81,961.04	28,177.00	15.81	2.96	0.00	-12.85	-2.96	-81.3	-100.0	28,161.18	28,174.03	28,177.00	12.85	2.96	0.0	0.0		
16	Idaho Batholith	60,282.82	47,170.25	2,181.63	833.03	5.13	-1,348.60	-827.90	-61.8	-99.4	44,988.62	46,337.22	47,165.11	1,348.60	827.90	3.0	1.8		
17	Middle Rockies	164,463.07	95,383.97	10,838.61	7,432.00	186.36	-3,406.60	-7,245.64	-31.4	-97.5	84,545.36	87,951.97	95,197.61	3,406.60	7,245.64	4.0	8.2		
18	Wyoming Basin	132,680.36	3,983.88	4.69	2.96	0.00	-1.72	-2.96	-36.8	-100.0	3,979.20	3,980.92	3,983.88	1.72	2.96	0.0	0.1		
19	Wasatch and Uinta Mountains	45,695.00	19,023.26	835.27	509.23	12.75	-326.04	-496.48	-39.0	-97.5	18,187.99	18,514.03	19,010.51	326.04	496.48	1.8	2.7		
20	Colorado Plateaus	136,573.14	1,015.15	0.07	0.00	0.00	-0.07	0.00	-100.0	0.0	1,015.08	1,015.15	1,015.15	0.07	0.00	0.0	0.0		
21	Southern Rockies	145,703.04	77,038.25	7,303.73	4,988.53	61.33	-2,315.21	-4,927.20	-31.7	-98.8	69,734.52	72,049.72	76,976.92	2,315.21	4,927.20	3.3	6.8		
22	Arizona/New Mexico Plateau	146,859.18	236.08	0.00	0.00	0.00	0.00	0.00	0.0	0.0	236.08	236.08	236.08	0.00	0.00	0.0	0.0		
23	Arizona/New Mexico Mountains	110,911.56	3,063.96	0.00	0.00	0.00	0.00	0.00	0.0	0.0	3,063.96	3,063.96	3,063.96	0.00	0.00	0.0	0.0		
24	Chihuahuan Deserts	105,451.12	0.00	-	-	-	-	-	-	-	-	-	-	-	-	-	-		
25	High Plains	267,507.71	0.00	-	-	-	-	-	-	-	-	-	-	-	-	-	-		
26	Southwestern Tablelands	151,240.59	1.79	0.00	0.00	0.00	0.00	0.00	0.0	0.0	1.79	1.79	1.79	0.00	0.00	0.0	0.0		
41	Canadian Rockies	18,878.41	16,211.74	1,067.83	317.53	0.00	-750.30	-317.53	-70.3	-100.0	15,143.91	15,894.22	16,211.74	750.30	317.53	5.0	2.0		
42	Northwestern Glaciated Plains	108,783.34	141.98	0.00	0.00	0.00	0.00	0.00	0.0	0.0	141.98	141.98	141.98	0.00	0.00	0.0	0.0		
43	Northwestern Great Plains	298,299.67	1,889.15	0.03	0.00	0.00	-0.03	0.00	-100.0	0.0	1,889.11	1,889.15	1,889.15	0.03	0.00	0.0	0.0		
77	North Cascades	30,393.32	25,394.49	1,843.81	742.35	0.52	-1,101.46	-741.83	-59.7	-99.9	23,550.69	24,652.15	25,393.98	1,101.46	741.83	4.7	3.0		
78	Klamath Mountains/California High North Coast Range	48,357.50	8,652.64	2.38	0.03	0.00	-2.34	-0.03	-98.6	-100.0	8,650.26	8,652.61	8,652.64	2.34	0.03	0.0	0.0		
79	Madrean Archipelago	39,650.63	18.02	0.00	0.00	0.00	0.00	0.00	0.0	0.0	18.02	18.02	18.02	0.00	0.00	0.0	0.0		
80	Northern Basin and Range	140,196.50	3,776.02	13.75	4.17	0.00	-9.58	-4.17	-69.7	-100.0	3,762.27	3,771.85	3,776.02	9.58	4.17	0.3	0.1		
81	Sonoran Basin and Range	118,368.75	0.00	-	-	-	-	-	-	-	-	-	-	-	-	-	-		
85	Southern California/Northern Baja Coast	20,955.65	0.00	-	-	-	-	-	-	-	-	-	-	-	-	-	-		
Total	Western US	3,407,681.68	437,120.06	27,416.81	17,621.74	324.80	-9,795.06	-17,296.94	-35.7	-98.2	409,703.24	419,498.33	436,795.27	9,795.06	17,296.94	2.4	4.1		

References

- Akaike, H. (1974). A new look at the statistical model identification. *IEEE Transactions on Automatic Control*, *19*(6), 716–723. <https://doi.org/10.1109/TAC.1974.1100705>
- Anderson, R. S., Anderson, L. S., Armstrong, W. H., Rossi, M. W., & Crump, S. E. (2018). Glaciation of alpine valleys: The glacier – debris-covered glacier – rock glacier continuum. *Geomorphology*, *311*, 127–142. <https://doi.org/10.1016/j.geomorph.2018.03.015>
- Anning, D. W., & Ator, S. W. (2017). *Generalized lithology of the conterminous United States* [Data set]. U.S. Geological Survey. <https://doi.org/10.5066/F7R78D4N>
- Dormann, C. F., Elith, J., Bacher, S., Buchmann, C., Carl, G., Carré, G., Marquéz, J. R. G., Gruber, B., Lafourcade, B., Leitão, P. J., Münkemüller, T., McClean, C., Osborne, P. E., Reineking, B., Schröder, B., Skidmore, A. K., Zurell, D., & Lautenbach, S. (2013). Collinearity: A review of methods to deal with it and a simulation study evaluating their performance. *Ecography*, *36*(1), 27–46. <https://doi.org/10.1111/j.1600-0587.2012.07348.x>
- Feng, X., Park, D. S., Liang, Y., Pandey, R., & Papeş, M. (2019). Collinearity in ecological niche modeling: Confusions and challenges. *Ecology and Evolution*, *9*(18), 10365–10376. <https://doi.org/10.1002/ece3.5555>
- Gesch, D. B., Evans, G. A., Oimoen, M. J., & Arundel, S. (2018). *The National Elevation Dataset* (pp. 83–110). American Society for Photogrammetry and Remote Sensing; USGS Publications Warehouse. <http://pubs.er.usgs.gov/publication/70201572>
- Haeberli, W., Hallet, B., Arenson, L., Elconin, R., Humlum, O., Kääb, A., Kaufmann, V., Ladanyi, B., Matsuoka, N., Springman, S., & Mühl, D. V. (2006). Permafrost creep and rock glacier dynamics. *Permafrost and Periglacial Processes*, *17*(3), 189–214. <https://doi.org/10.1002/ppp.561>
- Ikeda, A., & Matsuoka, N. (2006). Pebbly versus bouldery rock glaciers: Morphology, structure and processes. *Geomorphology*, *73*(3–4), 279–296. <https://doi.org/10.1016/j.geomorph.2005.07.015>
- Johnson, B. G., Thackray, G. D., & Van Kirk, R. (2007). The effect of topography, latitude, and lithology on rock glacier distribution in the Lemhi Range, central Idaho, USA. *Geomorphology*, *91*(1), 38–50. <https://doi.org/10.1016/j.geomorph.2007.01.023>

- Kass, J. M., Muscarella, R., Galante, P. J., Bohl, C. L., Pinilla-Buitrago, G. E., Boria, R. A., Soley-Guardia, M., & Anderson, R. P. (2021). ENMeval 2.0: Redesigned for customizable and reproducible modeling of species' niches and distributions. *Methods in Ecology and Evolution*, 2041-210X.13628. <https://doi.org/10.1111/2041-210X.13628>
- Kenner, R., & Magnusson, J. (2017). Estimating the Effect of Different Influencing Factors on Rock Glacier Development in Two Regions in the Swiss Alps: Effects of different influencing factors on rock glacier development. *Permafrost and Periglacial Processes*, 28(1), 195–208. <https://doi.org/10.1002/ppp.1910>
- Lute, A.C., Abatzoglou, J.T. & Link, T. (2021). SnowClim: high-resolution snow model and data for the western United States. *Manuscript in preparation*.
- Morris, S. (1981). Topoclimatic Factors and the Development of Rock Glacier Facies, Sangre de Cristo Mountains, Southern Colorado. *Arctic and Alpine Research*, 13(3), 329–338.
- Müller, J., Vieli, A., & Gärtner-Roer, I. (2016). Rockglaciers on the run- Understanding rockglacier landform evolution and recent changes from numerical flow modeling. *The Cryosphere Discussions*, 1–40. <https://doi.org/10.5194/tc-2016-35>
- Sloan, V. F., & Dyke, L. D. (1998). Decadal and Millennial Velocities of Rock Glaciers, Selwyn Mountains, Canada. *Geografiska Annaler. Series A, Physical Geography*, 80(3/4), 237–249.
- Wagner, T., Pauritsch, M., Mayaud, C., Kellerer-Pirklbauer, A., Thalheim, F., & Winkler, G. (2019). Controlling factors of microclimate in blocky surface layers of two nearby relict rock glaciers (Niedere Tauern Range, Austria). *Geografiska Annaler: Series A, Physical Geography*, 101(4), 310–333. <https://doi.org/10.1080/04353676.2019.1670950>
- Warren, D. L., & Seifert, S. N. (2011). Ecological niche modeling in Maxent: The importance of model complexity and the performance of model selection criteria. *Ecological Applications*, 21(2), 335–342. <https://doi.org/10.1890/10-1171.1>